

Inaugural dissertation
for
obtaining the doctoral degree
of the
Combined Faculty of Mathematics, Engineering and Natural
Sciences
of the
Ruprecht - Karls - University
Heidelberg

Presented by
M.Sc. Märt Rannap
born in Tallinn, Estonia

Date of oral examination:

Microcircuitry and afferent connectivity of the deep layers
of the medial entorhinal cortex

Referees: Prof. Dr. Andreas Draguhn

Prof. Dr. Hilmar Bading

STATEMENT OF ORIGINALITY

According to §8 (3) c) and d) of the Doctoral Degree Regulations:

I hereby declare that I have written the present thesis myself using only the sources and materials that I have explicitly indicated.

I hereby declare that I have not applied for an examination at any other institution, have not used the present thesis in this or any other form elsewhere as an examination paper and have not submitted the present thesis to any other faculty as a dissertation.

Märt Rannap

Heidelberg, 20th of November 2024

ASSOCIATED PUBLICATIONS

Rannap, M., Ohara, S., Winterstein, J., Roth, F.C., Draguhn, A., and Egorov, A.V. (2024). Functional and structural organization of medial entorhinal cortex layer VI. [Manuscript in revision]

Ohara, S.* , **Rannap, M.***, Tsutsui, K.-I., Draguhn, A., Egorov, A.V., and Witter, M.P. (2023). Hippocampal-medial entorhinal circuit is differently organized along the dorsoventral axis in rodents. *Cell Rep.* 42, 112001. 10.1016/j.celrep.2023.112001.

Rozov, A., **Rannap, M.**, Lorenz, F., Nasretdinov, A., Draguhn, A., and Egorov, A.V. (2020). Processing of hippocampal network activity in the receiver network of the medial entorhinal cortex layer V. *J. Neurosci.* 40, 8413-8425. 10.1523/JNEUROSCI.0586-20.2020.

Additional publication

Koumoundourou, A., **Rannap, M.**, De Bruyckere, E., Nestel, S., Reissner, C., Egorov, A.V., Liu, P., Missler, M., Heimrich, B., Draguhn, A., and Britsch, S. (2024). Regulation of hippocampal mossy fiber-CA3 synapse function by a Bcl11b/C1ql2/Nrxn3(25b+) pathway. *Elife.* 12:RP89854. 10.7554/eLife.89854.

Adherence to copyright regulations

I hereby indicate that data, figures, pictures, graphs and parts of text presented in the present thesis have been previously published in Ohara et al., 2023 or have been submitted for publication in Rannap et al. (in revision). Figures, pictures, graphs, text not written by myself and other major passages of text adapted for use in the present thesis from these manuscripts are correctly cited.

I confirm that as per the licence agreement for Ohara et al., 2023, I own the right to use all data, figures, pictures, graphs and text in my thesis. User license: Creative Commons Attribution International (CC BY 4.0) License, <https://creativecommons.org/licenses/by/4.0/>

Märt Rannap
Heidelberg, 20th of November 2024

TABLE OF CONTENTS

ABBREVIATIONS	11
SUMMARY	13
ZUSAMMENFASSUNG	15
1 INTRODUCTION	17
1.1 The hippocampal-medial entorhinal system	17
1.1.1 The medial entorhinal cortex.....	18
1.1.1.1 Delineation and subdivisions of the rodent entorhinal cortex	18
1.1.1.2 Laminar organization.....	19
1.1.1.3 Principles of extrinsic connectivity	21
1.1.1.4 Principles of intrinsic connectivity	23
1.1.1.5 Functional cell types.....	24
1.1.2 The hippocampal formation	26
1.1.2.1 Delineation and subdivisions of the rodent hippocampal formation.....	26
1.1.2.2 Anatomical architecture.....	27
1.1.2.3 Subcortical and neocortical connectivity along the dorsoventral axis	29
1.1.2.4 Functional roles of hippocampal formation subregions	30
1.2 The neurobiology of declarative memory	32
1.2.1 Types of memory.....	32
1.2.2 Neural circuits underlying short-term and working memory.....	33
1.2.3 Neural circuits underlying long-term episodic memory	34
AIMS OF THE STUDY	37
Functional organization of hippocampal projections to MEC layer V.....	37
Functional organization of MEC layer VI.....	38
CONTRIBUTIONS OF OTHERS	39
2 MATERIALS AND METHODS	41
2.1 Electrophysiology.....	41
2.1.1 Animals used in electrophysiological experiments	41
2.1.2 Surgical procedures and delivery of viral vectors	42
2.1.3 Preparation of mouse brain slices.....	42
2.1.4 Patch clamp recordings	44
2.1.4.1 Overview of the patch clamp technique	44
2.1.4.2 Experimental details	46
2.1.5 Staining and imaging of recorded slices	48
2.1.6 Analysis of electrophysiological data.....	49

2.2 Neuroanatomical tracings	50
2.2.1 Animals used in neuroanatomical tracing experiments	51
2.2.2 Surgical procedures and delivery of tracers or viral vectors	51
2.2.3 Staining and imaging of neuroanatomical tracing samples	52
2.2.4 Analysis of neuroanatomical tracing data.....	53
3 RESULTS.....	55
3.1 Organization of hippocampal projections to MEC layer V.....	55
3.1.1 Distribution of dorsal hippocampal projections in MEC layer V.....	55
3.1.2 Functional connectivity between the dorsal HF and MEC layer V	58
3.1.3 Distribution of ventral hippocampal projections in MEC layer V	63
3.1.4 Functional connectivity between the ventral HF and MEC layer V.....	66
3.2 Organization of hippocampal projections to MEC layer VI	71
3.2.1 Distribution of hippocampal projections in MEC layer VI	71
3.2.2 Functional connectivity between the dorsal HF and MEC layer VI.....	73
3.2.3 Functional connectivity between the ventral HF and MEC layer VI	76
3.3 Layer VI microcircuitry in MEC deep layers.....	79
3.3.1 Local connectivity within layer VI	79
3.3.2 Interlaminar connectivity between layers VI and Vb	81
3.3.3 Interlaminar connectivity between layers VI and Va.....	83
3.3.4 Functional connectivity from LVa to layers VI and Vb.....	84
4 DISCUSSION.....	87
4.1 Dorsoventral organization of hippocampal projections to MEC deep layers	87
4.2 Sublayer specificity of hippocampal projections to layer V	89
4.3 Convergence of dorsal and ventral hippocampal output signals in dorsal layer Va ..	90
4.4 Potential functions of the convergent hippocampal output pathway to dorsal LVa ..	91
4.5 The hippocampal output projection to MEC layer VI	92
4.6 Local and interlaminar connectivity of LVI neurons.....	93
4.7 Potential functions of the hippocampal output pathway to layer VI	95
4.8 Limitations of the study and future directions	96
CONCLUSION.....	99
ACKNOWLEDGEMENTS.....	101
REFERENCES	103
APPENDIX A	115
Supplementary figures	115
APPENDIX B.....	125
Supplementary tables.....	125

ABBREVIATIONS

AAV	adeno-associated virus
ACSF	artificial cerebrospinal fluid
AMPA	alpha-amino-3-hydroxy-5-methyl-4-isoxazolepropionic acid
ANOVA	analysis of variance
AP	anteroposterior
BDA	biotinylated dextran amine
CaMKIIa	calcium/calmodulin-dependent protein kinase II subunit alpha
ChR	channelrhodopsin
CNQX	cyanquixaline
Ctip2	COUP-TF interacting protein 2
DAPI	4,6-diamidino-2-phenylindole
DG	dentate gyrus
DV	dorsoventral
EC	entorhinal cortex
EGTA	ethylene-glycol-bis-tetraacetic acid
EPSC	excitatory postsynaptic current
Etv1	ETS variant 1
EYFP	enhanced yellow fluorescent protein
FS	fast-spiking
GABA	gamma-aminobutyric acid
GFP	green fluorescent protein
hChR2	humanized channelrhodopsin-2

HEPES	4-(2-hydroxyethyl)-1-piperazineethanesulfonic acid
HF	hippocampal formation
LI-LVI	MEC layer I / layer II / layer III / layer IV / layer V / layer VI
LEC	lateral entorhinal cortex
LVa	MEC layer Va
LVb	MEC layer Vb
MEC	medial entorhinal cortex
Mg-ATP	Mg-adenosine-5-triphosphate
ML	mediolateral
Na-GTP	Na-guanosine-5-triphosphate
NMDA	N-methyl-D-aspartate
PB	phosphate buffer
PBS	phosphate-buffered saline
PBS-Tx	PBS supplemented with 0.1% Triton X-100
PFA	paraformaldehyde
PHA-L	phaseolus vulgaris leucoagglutinin
PSP	postsynaptic potential
PV	parvalbumin
RMP	resting membrane potential
RT	room temperature
SEM	standard error of the mean
SPW-R	sharp wave-ripple complex
Sub	subiculum
tdTomato	tandem dimer Tomato

SUMMARY

The ability to navigate the environment and to remember and learn from past experiences is essential for an organism's survival. In the mammalian brain, these functions rely on an interplay between the hippocampal formation and the medial entorhinal cortex (MEC) which use multimodal sensory information to generate internal representations of the external world. Detailed spatial maps of the environment are first created by neurons in superficial layers of MEC. Hippocampal circuits subsequently combine the spatial information into complex representations that correspond to specific memory episodes. The mnemonic representations are finally consolidated in neocortical networks, requiring signals to be transmitted through neuronal populations in MEC deep layers V (LV) and VI (LVI).

Recent structural and functional insights have forced the classical view of MEC deep layers as a simple hippocampal-neocortical relay station to be greatly revised. LV can be divided into sublayers Va and Vb with contrasting roles – while cells in LVa mediate the canonical transfer of hippocampal representations to the neocortex, cells in LVb project locally to superficial MEC layers. Conversely, LVI neurons project back to all hippocampal subfields and help stabilize hippocampal representations. Although these findings suggest a capacity for sophisticated information processing within the MEC deep layer network, detailed understanding of this processing has remained incomplete due to poor knowledge of hippocampal innervation of individual deep layers and crosstalk between layers V and VI.

The present study combines anatomical tracing and *in vitro* electrophysiology to systematically characterize the functional organization of the hippocampal output pathway to MEC deep layers and the integration of LVI neurons into the MEC deep layer network. We confirm direct hippocampal projections to both layers V and VI and demonstrate the preferential targeting of LV neurons. Importantly, we discover a novel ventral hippocampal projection to LVa cells that uniquely distributes along the entire MEC dorsoventral axis. Simultaneously, we verify that dorsal hippocampal outputs mainly target LVb neurons. These sublayer-specific connectivity patterns set important constraints for the flow of hippocampal information to different downstream networks. We further examine interlaminar connectivity of LVI neurons, finding minimal excitatory and relatively common inhibitory connections between cells in layers VI and V. Overall, our results establish organizational principles for the hippocampal-medial entorhinal output pathway and suggest that MEC deep layers process signals largely independently in parallel streams of activity.

ZUSAMMENFASSUNG

Die Fähigkeit, sich in der Umwelt zurechtzufinden und aus Erfahrungen zu lernen, ist für das Überleben eines Organismus entscheidend. Im Gehirn von Säugetieren beruht diese Fähigkeit auf dem Zusammenspiel zwischen der Hippocampusformation (HF) und dem medialen entorhinalen Cortex (MEC), die multimodale sensorische Signale nutzen, um interne Repräsentationen der Außenwelt zu erzeugen. Repräsentationen der räumlichen Umwelt werden von Neuronen in oberflächlichen Schichten des MEC und der HF erstellt. Sie werden anschließend in neocortikalen Netzwerken konsolidiert, wofür Signale aus der HF durch die tiefen Schichten V (LV) und VI (LVI) des MEC übertragen werden müssen.

Neuere Erkenntnisse zeigen, dass die hippocampal-neocortikale Übertragung in tiefen MEC Schichten komplexer ist als bisher gedacht. LV umfasst die Unterschichten Va und Vb, wobei Zellen in LVa die kanonische Leitung an den Neocortex vermitteln und Zellen in LVb lokal in oberflächliche MEC Schichten projizieren. LVI Neuronen, dagegen, projizieren zurück in die HF und tragen zur Stabilisierung der hippocampalen Repräsentationen bei. Obwohl diese Befunde darauf hindeuten, dass die tiefen Schichten des MEC komplexe Informationsverarbeitungen durchführen, ist die Kenntnis der hippocampalen Innervation und der Verschaltung der einzelnen tiefen Schichten höchst unvollständig.

Die vorliegende Studie kombiniert anatomische und elektrophysiologische Methoden, um die funktionelle Organisation der hippocampalen Ausgangsbahn zu den tiefen MEC Schichten und der LVI Neurone im Netzwerk der tiefen MEC Schichten systematisch zu charakterisieren. Wir bestätigen direkte hippocampale Projektionen in die Schichten V und VI und zeigen, dass LV Neuronen bevorzugt innerviert werden. Wir beschreiben eine neue Projektion der ventralen HF zu LVa Zellen, die sich entlang der gesamten dorsoventralen Achse des MEC verteilt. Dorsale HF-Ausgänge steuern dagegen hauptsächlich LVb Neurone an. Diese Schicht-spezifischen Konnektivitätsmuster stellen wichtige Randbedingungen für den Informationsfluss der HF zu verschiedenen nachgeschalteten Netzwerken dar. Wir untersuchen außerdem die interlaminare Konnektivität von LVI Neuronen und finden minimale exzitatorische und relativ häufige inhibitorische Verbindungen zwischen Zellen in den Schichten VI und V. Insgesamt legen unsere Ergebnisse Organisationsprinzipien für die hippocampale-mediale entorhinale Ausgangsbahn fest und deuten darauf hin, dass tiefe MEC Schichten Signale unabhängig in parallelen Aktivitätsströmen verarbeiten.

1 INTRODUCTION

1.1 The hippocampal-medial entorhinal system

The ability to navigate the external environment and to remember and learn from past experiences are essential operations carried out by all complex nervous systems. In the mammalian brain, these functions rely on the hippocampal-entorhinal system – a major neuronal network comprising the hippocampal formation (HF) and the adjacent entorhinal cortex (EC). Due to its readily identifiable structure, directional signal flow and a fundamental role in memory, HF is one of the most thoroughly studied areas of the mammalian central nervous system (Johnston and Amaral, 2004). On the other hand, the striking diversity of spatially tuned neurons in the medial part of EC (MEC) has similarly generated significant research interest in this cortical region and enabled the first detailed investigations of network computations performed by a higher-order brain area (Tukker et al., 2022). Despite a wealth of existing functional, molecular and connectomic data, many fundamental questions about the hippocampal-entorhinal system remain unanswered, including details on the organization of basic connectivity.

The hippocampal-entorhinal system rose to prominence in the landmark medical case of Henry Molaison, known as patient H.M., who suffered from intractable epilepsy originating bilaterally in the medial temporal lobe (Scoville and Milner, 1957). In order to alleviate his seizures, H.M. underwent surgery in which parts of his medial temporal lobe were bilaterally resected, including most of HF and almost the entirety of EC (Annese et al., 2014; Scoville and Milner, 1957). As a result of the surgery, H.M. strikingly lost the ability to form new long-term memories, while his ability to remember earlier events was only slightly affected and his general intelligence remained unchanged (Scoville and Milner, 1957). This established the hippocampal-entorhinal system as a critical circuit for long-term memory formation.

A second major breakthrough occurred in 1971, when John O'Keefe and Jonathan Dostrovsky reported that cells in the hippocampus fire preferentially when the animal is at a specific location in the environment (O'Keefe and Dostrovsky, 1971). As different hippocampal cells fire at different locations, an intrinsic map of the external environment is

generated (O'Keefe, 1976). The concept of intrinsic representation of external space was extended with the discovery of spatially modulated cells in MEC (Fyhn et al., 2004). However, in contrast to hippocampal neurons which typically fire at single locations, cells in MEC fired at multiple locations, covering the environment in a symmetrical hexagonal grid-like pattern (Hafting et al., 2005). Later reports have identified a number of additional spatially selective cell types in MEC (Tukker et al., 2022) and it is estimated that the majority of all medial entorhinal cells may be spatially modulated (Diehl et al., 2017). On the one hand, the spatial processing in MEC and HF makes these structures compelling candidates for a neural navigation system (Buzsáki and Moser, 2013). At the same time, the detailed spatial information available in both networks is widely considered to provide a spatial dimension to individual memory episodes (Buzsáki and Moser, 2013). Conscious memories are thought to be constructed by the hippocampal network which combines spatial information from MEC with object-context relationships encoded by cells in the lateral EC, allowing multifaceted internal representations of external events to be generated (Nilssen et al., 2019).

1.1.1 The medial entorhinal cortex

1.1.1.1 Delineation and subdivisions of the rodent entorhinal cortex

The entorhinal cortex (EC) is part of periallocortex, a distinct type of cortex with a more complex organization than the three-layered allocortical hippocampus but lacking the internal granular layer of the neocortex (Insausti et al., 2017). Its name derives from its location in the medial temporal lobe, being partially enclosed by the rhinal sulcus (Witter et al., 2017). In rodents, EC constitutes a prominent section of the posterior cortical mantle and is bordered medially by the parasubiculum, laterally by the perirhinal cortex, dorsally by the postrhinal cortex and antero-ventrally by the piriform cortex (van Groen, 2001; Figure 1). Ventral and intermediate hippocampal levels are situated immediately antero-medially to EC, whereas the dorsal HF starts above the dorsal border of EC (Fanselow and Dong, 2010; Figure 1).

EC is most commonly divided into a medial (MEC) and a lateral area (LEC), with MEC located postero-medially and LEC antero-laterally (van Groen, 2001; Figure 1B). Both subdivisions form an interface between HF and the neocortex, simultaneously conveying

cortical signals to HF and routing hippocampal outputs to downstream cortical networks (Witter et al., 2017). Despite these similarities, MEC and LEC show differences in cytoarchitecture, extrinsic and intrinsic connectivity and function. Importantly, MEC and LEC receive input from partially divergent cortical and subcortical areas (Kerr et al., 2007). This is thought to underlie key functional differences between the two regions: while neurons in MEC are spatially tuned, LEC neurons appear to represent specific objects in context (Nilssen et al., 2019). The two information streams converge in HF, where complex representations of the external environment are created.

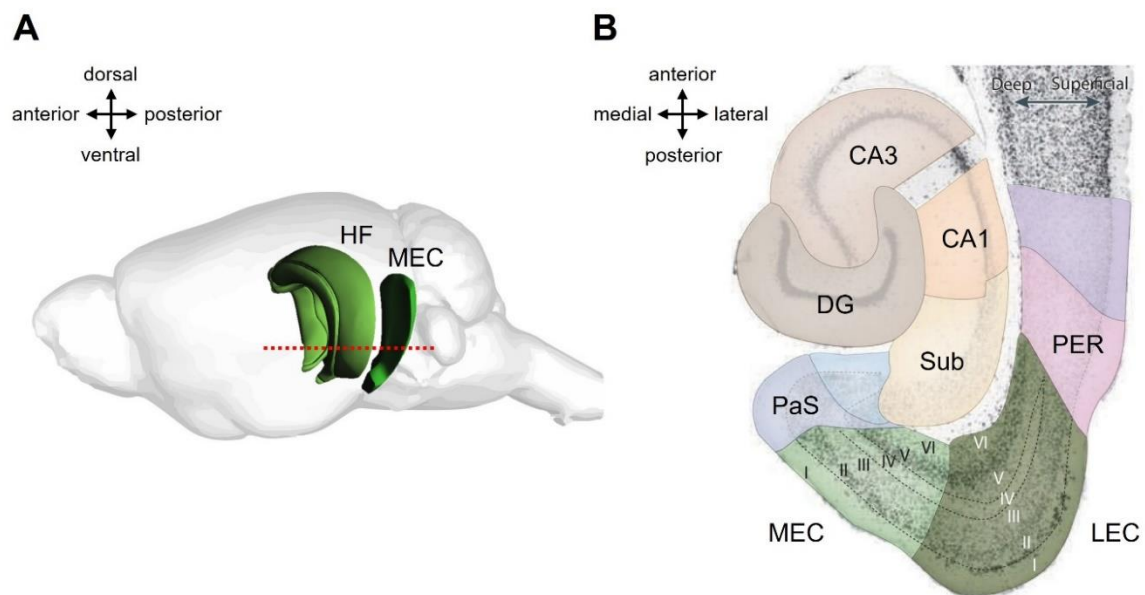


Figure 1. Location of the medial entorhinal cortex and the hippocampal formation in the rodent brain. (A) The medial entorhinal cortex (MEC) and the hippocampal formation (HF) are situated in the caudal part of the rodent brain. The dotted red line indicates the approximate level of the horizontal section shown in B. Adapted from Allen Brain Explorer (<http://connectivity.brain-map.org/3d-viewer>). (B) A horizontal section through the rodent parahippocampal region with the main subdivisions indicated. LEC, lateral entorhinal cortex; DG, dentate gyrus; Sub, subiculum; PaS, parasubiculum; PER, perirhinal cortex. Modified from van Strien et al., 2009.

1.1.1.2 Laminar organization

MEC comprises six regularly structured cortical layers (Nilssen et al., 2019; Figure 1B). The main neuronal populations are confined to layers II, III, V and VI. Layer I harbors a small number of interneurons and a thin layer IV, referred to as *lamina dissecans*, features very few neurons in general. Because of the overall scarcity of neurons in layer IV, detailed

studies on its neuronal morphology, connectivity or function have not been performed (Nilssen et al., 2019) and I will therefore exclude this layer from further discussion.

MEC layer I (LI) is a major target layer for afferent fibers from neocortical areas (Witter et al., 2017). Here they contact the apical dendrites of layer II and III but also layer V principal cells which all rise to and ramify in LI (Witter et al., 2017). The layer is sparsely populated by interneurons (Germroth et al., 1989; Miettinen et al., 1997; Wouterlood and Pothuizen, 2000) which were recently shown to be analogous to neocortical neurogliaform and single bouquet-like cells based on axonal morphology (Shi et al., 2023). Whether and how these interneurons modulate the neocortical input stream, however, remains unclear.

Layer II (LII) features a more diverse population of neurons. LII principal neurons can be genetically divided into two main groups – calbindin- and reelin-expressing cells (Fujimaru and Kosaka, 1996; Pesold et al., 1998; Witter et al., 2017). Expression of calbindin typically corresponds with a pyramidal morphology and the expression of reelin with a stellate morphology (Kitamura et al., 2014; Varga et al., 2010). The dendrites of stellate cells ramify in both layers I and II, while the apical dendrites of pyramidal cells similarly extend to LI (Canto and Witter, 2012; Klink and Alonso, 1997). This allows both groups of principal cells to contact the axons of neocortical afferents terminating in LI. Stellate cells form a major source of medial entorhinal input to HF (Nilssen et al., 2019; Tamamaki and Nojyo, 1993), whereas pyramidal cells are primarily a source of intra-entorhinal projections (Ohara et al., 2019).

Layer III (LIII) harbors a relatively homogenous population of large pyramidal neurons whose apical dendrites extend to LI (Canto and Witter, 2012; Gloveli et al., 1997). The neurons form a second major source of medial entorhinal input to HF, targeting area CA1 and the subiculum (Nilssen et al., 2019).

Layer V (LV) can be genetically divided into two sublayers – a thinner more superficial layer Va (LVa) and a thicker deeper layer Vb (LVb). Neurons in LVa express ETS variant 1 (Etv1), while neurons in LVb express COUP-TF interacting protein 2 (Ctip2) (Ramsden et al., 2015). Principal cells in LVa are typically large pyramidal neurons with horizontally oriented basal dendrites that largely remain within LVa and an occasionally absent apical dendrite that reaches and ramifies in LI. LVb principal cells are typically also pyramidal neurons with an apical dendrite that extends to LI but feature a smaller soma size and locally

ramifying basal dendrites (Canto and Witter, 2012; Hamam et al., 2002; Ohara et al., 2021; Sürmeli et al., 2015). Importantly, LVa neurons are a major source of medial entorhinal outputs to various neocortical and subcortical areas (Ohara et al., 2018; Sürmeli et al., 2015), whereas LVb neurons are a source of intra-entorhinal superficially oriented projections (Ohara et al., 2021).

Layer VI (LVI) is the deepest layer of MEC and is situated directly above a sheet of white matter covering the hippocampus, known as the alveus. LVI principal neurons feature a large soma and horizontally oriented dendrites, similarly to cells in LVa (Canto and Witter, 2012). Contrary to neurons in other layers, however, the cells lack a clear apical dendrite (Canto and Witter, 2012). Throughout LVI, principal neurons express molecular markers typical for neocortical LVIIb but not LVIIa, suggesting that MEC LVI lacks an analogue for neocortical LVIIa (Ben-Simon et al., 2022; Feldmeyer, 2023).

1.1.1.3 Principles of extrinsic connectivity

MEC is functionally organized as a bidirectional interface between HF and the neocortex, conveying sensory signals from various neocortical regions to HF and simultaneously transferring processed hippocampal output signals back to different cortical areas. MEC is targeted by a wide range of neocortical afferent fibers, constituting roughly 20% of its total afferent input (Kerr et al., 2007). Neocortical afferents primarily target MEC superficial layers and provide a major source of input to layer II and III principal neurons (Witter et al., 2017). The largest source of superficially terminating afferents originates from the odor-processing piriform cortex, followed by the visual-processing occipital cortex. Lesser input is provided by the associational parietal and orbitofrontal cortices (Kerr et al., 2007). Importantly, neurons in MEC superficial layers do not reciprocate these projections and entorhinal outputs to neocortical, as well as subcortical areas, originate from the deep LVa (Ohara et al., 2019, 2018; Sürmeli et al., 2015; Figure 2). The target areas of LVa projections include the perirhinal, cingulate and retrosplenial cortices, primary and secondary visual cortex, nucleus accumbens and amygdala (Ohara et al., 2018; Sürmeli et al., 2015).

Canonically, projections to HF arise from layers II and III, conveying spatially tuned signals from MEC to hippocampal neurons. LII projections originate from stellate cells and target the dentate gyrus and area CA3 (Tamamaki and Nojyo, 1993; Varga et al., 2010), whereas LIII pyramidal neurons project to area CA1 and the subiculum (Steward and Scoville, 1976;

van Strien et al., 2009; Figure 2). Hippocampal output signals from CA1 and the subiculum, in turn, are received by neurons in MEC layers V and VI (Cenquizca and Swanson, 2007; Swanson and Cowan, 1977; van Strien et al., 2009; Figure 2). LV is thought to be the primary target layer of hippocampal projections, although the exact sublayer specificity of these projections remains unclear. While dorsal CA1 and subiculum have been shown to predominantly target LVb (Rozov et al., 2020; Sürmeli et al., 2015), at intermediate hippocampal levels CA1 and the subiculum innervate layers Va and Vb with similar strength (Rozov et al., 2020). Sublayer specificity of the hippocampal projection to LV might thus depend on the hippocampal level of origin. As entorhinal outputs to the neocortex originate from LVa but not LVb (Sürmeli et al., 2015), how hippocampal signals from different parts of HF propagate to and are relayed between the two sublayers has major implications for the neocortical consolidation of hippocampal output signals.

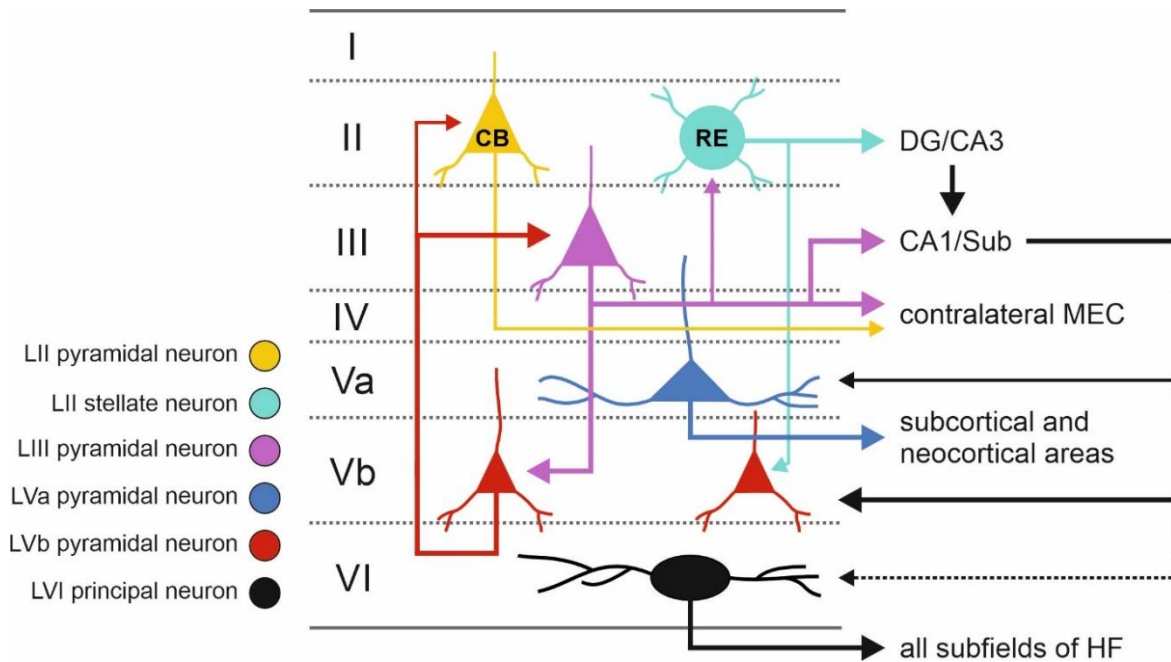


Figure 2. Overview of extrinsic and intrinsic connectivity of principal cells in the medial entorhinal cortex. The figure illustrates major connectivity motifs of MEC excitatory neurons in each layer. Because LI only harbors a small number of interneurons and LIV features very few neurons in general, connectivity for those layers is not shown. Due to a lack of detailed information on the hippocampal output projection to LVI, this projection is shown with a dashed line. CB, calbindin; RE, reelin; DG, dentate gyrus; Sub, subiculum.

Hippocampal efferents have also been shown to project to LVI (Ben-Simon et al., 2022; O'Reilly et al., 2013; Swanson and Cowan, 1977; van Strien et al., 2009) and stimulation of the hippocampal output pathway has been reported to elicit responses in the layer

(Kloosterman et al., 2003a; Tu et al., 2009). The organization of these projections, however, has not been systematically studied and the innervation of LVI neurons by hippocampal output signals remains unclear. Interestingly, non-canonical entorhinal-hippocampal projections have recently been reported for both layers V and VI, finding that LVa neurons project to hippocampal area CA1 (Tsoi et al., 2022), a subpopulation of LVb neurons targets the dentate gyrus (Yamamoto et al., 2024) and LVI neurons project to all subfields of HF (Figure 2) with a preference for area CA3 (Ben-Simon et al., 2022). The function of these projections has only been investigated for LVI neurons, revealing a role in spatial information processing and memory formation (Ben-Simon et al., 2022). Regardless of their function, these pathways challenge the canonical view, according to which only information from superficial entorhinal neurons reaches HF.

1.1.1.4 Principles of intrinsic connectivity

The intrinsic connectivity of MEC features prominent ascending and descending pathways. Descending projections originate from LII stellate and LIII pyramidal neurons and converge on principal cells in LVb (Beed et al., 2020; Sürmeli et al., 2015; Figure 2). Input from LIII has been shown to convey up-down activity to LVb neurons (Beed et al., 2020), suggesting that LVb cells might act as a coincidence detector by integrating cortical up-down activity with hippocampal output patterns (Gerlei et al., 2021). Interestingly, LVb neurons are also the primary source of ascending MEC projections, strongly targeting pyramidal cells in LIII and to a lesser degree in LII (Ohara et al., 2021; Figure 2). LIII pyramidal neurons, in turn, unidirectionally target LII stellate cells (Winterer et al., 2017). The presence of these projections enables hippocampal output signals received by LVb neurons to be integrated with signals processed by superficial entorhinal neurons and for hippocampal output activity to potentially reenter HF circuits. This is particularly important as connections between LVb and LVa principal neurons have been shown to be sparse in both directions (Ohara et al., 2021; Rozov et al., 2020), suggesting that hippocampal signals propagating to LVb are not conveyed to LVa neurons and are thereby not transferred to neocortical areas. Finally, MEC activity in both hemispheres is coordinated by direct commissural projections originating from LIII and LII pyramidal neurons which target superficial layers of the contralateral MEC (Ohara et al., 2019; Tang et al., 2015; Figure 2).

1.1.1.5 Functional cell types

Neurons in all MEC layers are characterized by firing behavior that reflects a variety of spatial aspects of the surrounding environment.

Grid cells feature multiple periodically arranged firing fields, forming a hexagonally structured grid that spans the local environment (Hafting et al., 2005; Tukker et al., 2022; Figure 3A). Grid cells can be both pure or directionally tuned. The firing fields of pure grid cells classically only depend on the location of the animal (Hafting et al., 2005) and these cells have been suggested to compute a universal spatial metric (Buzsáki and Moser, 2013). In contrast, the hexagonal firing fields of directionally tuned grid cells only appear when the animal faces a certain direction (Sargolini et al., 2006). Pure grid cells are predominantly found in LII, whereas directional grid cells are found in all other major layers (Sargolini et al., 2006). The specific types of neurons involved in grid firing have not been definitively determined. This is because extracellular recording techniques that have been used to study neuronal firing behavior *in vivo* do not typically allow the labeling of recorded cells. Furthermore, the firing pattern or action potential shape of a neuron can only be reliably used to distinguish cells with sufficiently distinct firing properties, such as fast-spiking interneurons (Tukker et al., 2022). The remaining cells are commonly grouped together as putative principal neurons and they comprise nearly all pure and directionally tuned grid cells (Sargolini et al., 2006; Tukker et al., 2022). *In vivo* juxtacellular recordings from a small number of LII grid cells have suggested that grid cells in this layer might be predominantly pyramidal neurons (Tang et al., 2014) but this finding remains to be confirmed.

Head direction cells fire when the head of the animal faces in a particular direction relative to its environment (Tukker et al., 2022; Figure 3B). Head direction signals encoded by MEC neurons are not generated locally in MEC but are rather computed subcortically by the ventral tegmentum and mammillary bodies based on cues from the vestibular system and are subsequently relayed to different cortical areas (Taube, 2007). It has been speculated that head direction cells could provide a directional reference frame for medial entorhinal spatial representations (Buzsáki and Moser, 2013). Alternatively, head direction in combination with velocity signals might represent a mechanism by which directionally tuned grid cell firing is generated (Tocker et al., 2015). Convergent input from a population of directional grid cells with different tuning might in turn underlie the directionally independent firing of

pure grid cells (Gerlei et al., 2020). Consistently, head direction cells are found abundantly in LIII and in the deep layers but not in LII (Sargolini et al., 2006; Tukker et al., 2022). Similarly to grid cells, head direction cells are overwhelmingly putative principal neurons (Tukker et al., 2022).

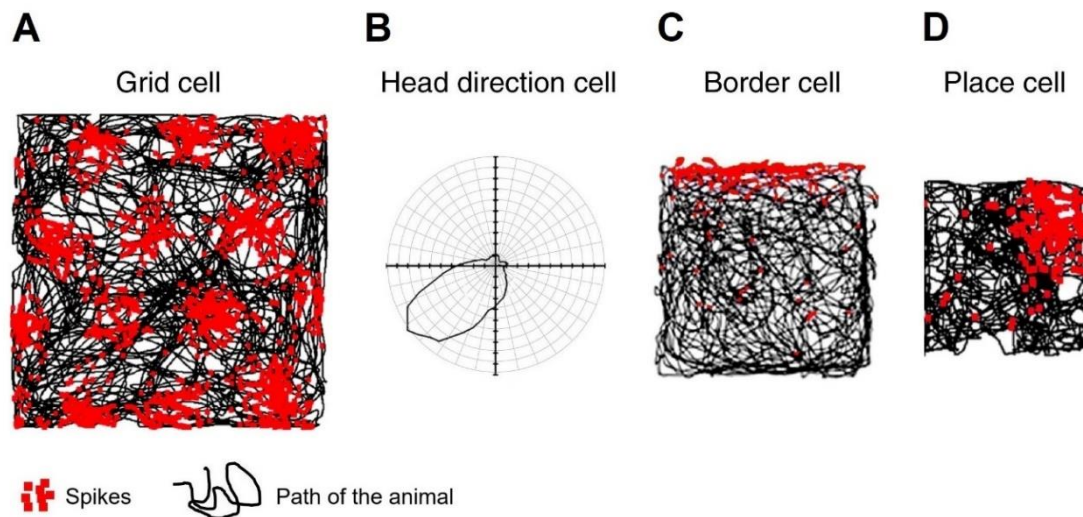


Figure 3. Typical spatially selective firing patterns of neurons in the medial entorhinal cortex and the hippocampal formation. (A) Typical firing pattern of a pure MEC grid cell, showing multiple periodically arranged firing fields that form a hexagonally structured lattice spanning the local environment. (B) Firing rate of a typical head direction cell plotted in polar coordinates. This particular cell is selectively active when the head of the animal is pointed in the southwestern direction. (C) An MEC border cell fires when the animal resides near the northern wall of the enclosure. (D) Spatially selective neurons in HF are typically place cells which usually fire at a single location in the environment. Modified from Marozzi and Jeffery, 2012.

Border cells fire when the animal is at a specific location relative to a geometric border in the environment (Solstad et al., 2008; Tukker et al., 2022; Figure 3C). They are found in all layers of MEC and are again putative principal neurons (Solstad et al., 2008). In vivo juxtacellular recordings have suggested that border cells in LII might be predominantly stellate cells (Tang et al., 2014).

Object-vector cells are found in superficial MEC layers and fire when the animal is at a specific distance and direction from a particular object, independent of the object's properties (Tukker et al., 2022).

The different classes of spatially tuned cells are active across all environments and together encode detailed maps of the surrounding space (Buzsáki and Moser, 2013). The spatial maps

generated by MEC are thought to be fundamental for episodic memory formation and likely navigation as key functions of the hippocampal-medial entorhinal system. First, all of the above-mentioned cell types have been shown to project to HF, providing a stream of detailed spatial information to hippocampal neurons (Zhang et al., 2013). These spatial signals are generally agreed to underlie spatially selective firing in the hippocampus and to thereby provide a spatial component to individual memory episodes (Moser et al., 2015). How each cell type individually contributes to spatial firing in HF, however, remains unclear. While it has been suggested that combined input from several grid cells could result in a single firing field seen in hippocampal neurons (Figure 3D), several lines of evidence suggest the actual mechanisms are more complex and involve simultaneous input from different MEC cell types (Moser et al., 2015).

Second, the different spatially selective cell types have been suggested to encode a spatial metric that would enable the animal to compute spatial relationships between landmarks (Buzsáki and Moser, 2013). These relationships are then mapped onto a reference frame which allows the animal to position itself in the environment. This is commonly referred to as map-based or allocentric navigation. The spatial metric would also provide a mechanism for the calculation of travelled distances which, in combination with the animal's initial location, is essential for self-referenced or egocentric navigation (Buzsáki and Moser, 2013). The ability to explain these two fundamental navigation systems makes the idea of a universal spatial metric encoded by MEC grid cells compelling as a mechanistic explanation of navigation. Nevertheless, the degree to which MEC is essential for different aspects of navigation remains controversial and contributions from other brain areas, such as the retrosplenial cortex, have been suggested to be critical for accurate navigation (Ekstrom and Hill, 2023).

1.1.2 The hippocampal formation

1.1.2.1 Delineation and subdivisions of the rodent hippocampal formation

The term “hippocampal formation” (HF) is used somewhat loosely in the literature and sometimes includes parahippocampal structures, including EC. In a more narrow definition, HF comprises the dentate gyrus (DG), the hippocampus proper with its subfields CA1-CA3 and the subiculum (Sub; van Strien et al., 2009; Figure 1B) and this classification is also

used here. HF is a prominent C-shaped structure situated in the caudal brain directly antero-medially to EC (van Strien et al., 2009; Figure 1). It is typically divided into a ventral, intermediate and dorsal part based on molecular and functional differences (Fanselow and Dong, 2010; Strange et al., 2014). All subregions of HF are present throughout the three dorsoventral domains and the general organization of subregions remains identical at all dorsoventral levels (Fanselow and Dong, 2010; Strange et al., 2014; van Strien et al., 2009).

1.1.2.2 Anatomical architecture

The functional organization of HF supports largely unidirectional signal flow between the subregions, relaying entorhinal afferent signals received by DG through the CA areas to Sub (DG → CA3 → CA1 → Sub) (van Strien et al., 2009; Figure 4). All subdivisions of HF are part of the allocortex which is more primitive than periallocortex and only features a single principal cell layer together with additional relatively cell-free layers where dendritic and axonal fibers of the principal cells are located (Insausti et al., 2017).

The **dentate gyrus (DG)** is a prominent recipient structure of HF. It features a large number of densely packed granule cells which are the primary targets of EC LII stellate cell axons (Cappaert et al., 2015; Figure 4). Granule cells themselves project along the entire length of CA3 and form the main source of input to CA3 pyramidal cells (Cappaert et al., 2015).

Area **CA3** harbors large pyramidal neurons with complex apical dendritic trees (Cappaert et al., 2015). Granule cell axons originating throughout DG target the dendritic domain closest to the pyramidal cell soma and thereby powerfully drive the recipient cells (Figure 4). A second major source of input to CA3 originates from the pyramidal neurons themselves which form extensive recurrent connections with other CA3 pyramidal cells both ipsi- and contralaterally (Figure 4). Finally, collateral fibers of the same EC LII stellate cell axons that project to DG also innervate distal apical dendrites of CA3 pyramidal cells, providing a weak excitatory drive onto the pyramidal neurons (Figure 4). CA3 pyramidal cells project almost exclusively intrahippocampally, heavily targeting hippocampal area CA1 through axon collaterals that ramify from the prominent recurrent fibers (Cappaert et al., 2015).

Area **CA2** is a minor region separating areas CA3 and CA1. It contains large pyramidal cells which receive strong input from CA3 and in turn project to area CA1 (Dudek et al., 2016). The region has recently been shown to play an important role in social behavior and to

participate in the consolidation of socially relevant information into long-term memory (Dudek et al., 2016).

Area CA1 similarly contains a large number of pyramidal cells with prominent apical dendrites which are targeted by the axons of CA3 pyramidal neurons (Cappaert et al., 2015; Figure 4). Additional input to distal parts of the apical dendrites originates from pyramidal cells in EC LIII (Cappaert et al., 2015; Figure 4). CA1 principal cells themselves target extrahippocampal areas, including EC, and project extensively to Sub (Figure 4), following a distinct topography where neurons located more proximally in CA1 (i.e. closer to CA3) project to distal Sub and cells located more distally in CA1 (i.e. closer to Sub) project to proximal Sub (Cappaert et al., 2015). Interestingly, the CA1 projection to EC follows an analogous topography where cells in proximal CA1 target MEC and cells in distal CA1 target LEC (Naber et al., 2001). The hippocampal projection to MEC was described in Section 1.1.1.3.

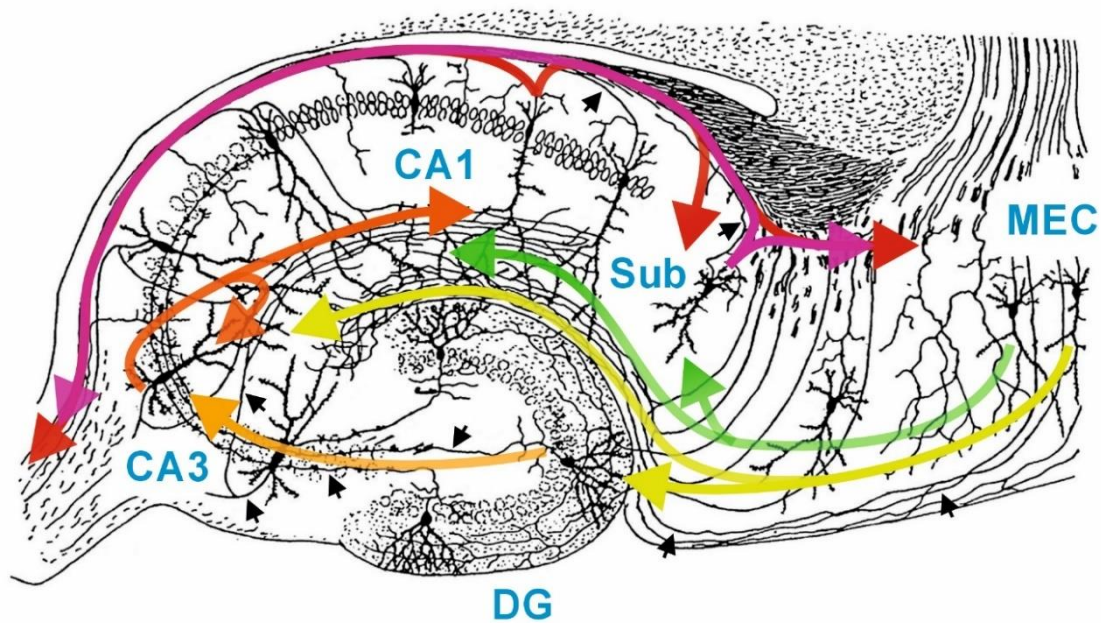


Figure 4. Anatomical architecture and functional organization of the rodent hippocampal formation. Shown is a schematic drawing of HF with its subfields and the adjacent MEC. Select principal neurons in different regions are depicted with their dendritic arbors and axonal fibers (black arrows). Colored arrows indicate major directions of signal flow in the hippocampal-medial entorhinal system. DG, dentate gyrus, Sub, subiculum. Modified from Cajal, 1911.

The **subiculum (Sub)** is the final target of signals propagating within HF and a major hippocampal output structure. Subicular neurons are predominantly large pyramidal cells but in contrast to neurons in the principal cell layers of other HF subdivisions they are distributed more diffusely and might form a number of discrete subregions (Cembrowski et

al., 2018). The different subregions are extensively innervated by axonal fibers from area CA1 and, similarly to CA1 principal cells, receive input from pyramidal neurons in EC LIII (van Strien et al., 2009; Figure 4). Cell populations throughout Sub are a substantial source of projections to extrahippocampal regions, including EC (Figure 4). The subicular projection to EC exhibits a reverse topography to CA1 where distal Sub preferentially targets MEC and proximal Sub LEC (van Strien et al., 2009).

1.1.2.3 Subcortical and neocortical connectivity along the dorsoventral axis

The strong bidirectional connectivity between EC and HF dictates a large part of the hippocampal signal flow and appears to be conserved along the entire dorsoventral axis of both structures (van Strien et al., 2009). Individual HF subregions, however, are additionally connected to a number of cortical and subcortical brain areas with major differences between dorsal and ventral hippocampal levels. In the case of DG and CA3, these connections are largely limited to afferent projections from specific brain stem nuclei and the septal complex (Cappaert et al., 2015) which has been shown to regulate oscillatory activity in the hippocampus (Nuñez and Buño, 2021). Both CA1 and Sub similarly receive input from certain brain stem nuclei and are bidirectionally connected to the septal complex (Cappaert et al., 2015). However, CA1 and Sub receive input from a wider selection of subcortical regions and, importantly, project to different sub- and neocortical areas. While some of these projections are shared between dorsal and ventral CA1 and/or Sub, such as to the orbitofrontal cortex (Jay and Witter, 1991), most projections exhibit clear differentiation between the dorsal and ventral hippocampal poles.

Dorsal CA1/Sub project extensively to the retrosplenial cortex and dorsal Sub additionally sends projections either directly or through mammillary bodies to the anterior thalamus, which also projects to the retrosplenial cortex (Fanselow and Dong, 2010). The mammillary bodies play a central role in computing the head direction of the animal (Taube, 2007), enabling the retrosplenial cortex to integrate head direction information received through the mammillary-anterior thalamic axis with dorsal hippocampal episodic representations. Accordingly, the retrosplenial cortex has been suggested to be involved in the consolidation and retrieval of previously learned spatial relationships and switching between egocentric and allocentric frames of reference (Mitchell et al., 2018). Dorsal Sub also strongly projects to the rostromedial part of the nucleus accumbens shell and to the rostral caudoputamen

(Fanselow and Dong, 2010). In turn, the caudoputamen innervates the reticular part of substantia nigra which is involved in the orientation and adjustment of movements, suggesting a role for the dorsal Sub in motor control (Fanselow and Dong, 2010; Foster et al., 2021).

Ventral CA1/Sub are strongly and bidirectionally connected to amygdalar nuclei, implicating ventral hippocampal output structures in fear learning and general emotional processing (Fanselow and Dong, 2010). Indeed, a role in the regulation of emotional responses is also seen for other ventral CA1/Sub projections, such as to the infralimbic cortex which is involved in fear suppression. Furthermore, both subregions project to several olfactory areas, including the olfactory bulb, and loss of the latter structure has been implicated in depressive-like symptoms. Finally, ventral CA1/Sub innervate the caudomedial part of the nucleus accumbens shell as well as several areas of the hypothalamus, implicating the ventral hippocampus in neuroendocrine and autonomic control (Fanselow and Dong, 2010).

Together, these distinct connectivity schemes suggest significant functional divergence between the dorsal and ventral HF. While the dorsal HF appears to be primarily spatially modulated and participate in spatial learning and exploration, the ventral HF appears to be positioned to regulate emotional experiences and control general affective states (Fanselow and Dong, 2010). This is largely supported by behavioral studies, finding that dorsal but not ventral hippocampal lesions disrupt contextual fear and spatial memory (Moser et al., 1993), while ventral but not dorsal lesions alter stress responses and emotional behavior (Fanselow and Dong, 2010; Henke, 1990).

1.1.2.4 Functional roles of hippocampal formation subregions

While all HF subregions process representations of the external environment, the specific functional roles of individual subregions are distinct. Central to this functional segregation is the unidirectional signal flow between the HF subfields (DG → CA3 → CA1 → Sub).

An effective memory system must be capable of storing a large number of representations while at the same time differentiating between events with a high degree of similarity. HF achieves this through sparse coding, where individual events are represented by a limited population of neurons (Barnes et al., 1990). Neuronal activity is particularly sparse in DG, where only a small minority of granule cells are active during a given task (Diamantaki et

al., 2016). DG thus transforms the ubiquitous firing of medial entorhinal grid and other cell types into a sparse code of neural representations, allowing slight differences in input to be transformed into large differences in the pattern of activated cells. This is referred to as pattern separation (Treves and Rolls, 1994). Granule cells generally retain spatially selective firing but in contrast to the multiple firing fields of entorhinal neurons they tend to only fire at a single location in the environment (GoodSmith et al., 2017). Neurons with this type of firing behavior are referred to as place cells (Figure 3D) and they represent the hallmark firing pattern of spatially tuned neurons throughout the hippocampal subregions (O'Keefe and Dostrovsky, 1971).

Axons of dentate granule cells subsequently relay signals from DG to hippocampal area CA3. Despite sparse innervation, the location of granule cell axon synapses close to CA3 pyramidal cell somata and strong short-term facilitation ensure that CA3 pyramidal cells are powerfully driven by dentate activity (Rebola et al., 2017). Recurrent connectivity with pre-existing connectivity motifs between CA3 pyramidal neurons subsequently enable the formation of enhanced synaptic associations between a select group of interconnected pyramidal cells, resulting in the generation of an interdependent cell ensemble (Rebola et al., 2017). Called engrams, these cell ensembles combine spatial signals from MEC neurons with information about objects from LEC circuits and are thought to represent the neural correlates of memory episodes (Josselyn and Tonegawa, 2020). At shorter time scales, enhanced connectivity between cells is likely formed and retained by forms of Hebbian learning, such as spike-timing-dependent plasticity, while at longer time scales the connections are thought to be maintained by the long-term potentiation of synapses (Rebola et al., 2017). Importantly, because engram cells are interconnected, activation of isolated parts of the ensemble can lead to activation of the full engram. This mechanism, referred to as pattern completion, underlies the recall of whole memories from partial cues and is likely controlled by the direct entorhinal projection onto distal apical dendrites of CA3 pyramidal cells (Rolls, 2013).

Neuronal activity from area CA3 is next relayed to the CA1 subfield. Similarly to CA3, area CA1 also features memory engrams (Josselyn and Tonegawa, 2020) but because the region lacks prominent recurrent connectivity and inherits its activity from the upstream CA3 network, the primary role of CA1 does not appear to be the *de novo* generation of novel memory episodes. Instead, CA1 is hypothesized to play a role in contextual mismatch detection. For this, sensory signals arriving in CA1 directly from EC LIII, which are thought

to contain information about the current experience, are compared with existing representations arriving from the CA3 network (Barrientos and Tiznado, 2016). Based on whether these two input streams match or not, distinct contextual representations are generated by CA1 neurons which enable contextual discrimination in downstream networks (Barrientos and Tiznado, 2016). Engram activity from CA1 is further transmitted to Sub but apart from being an output structure of HF, the specific functions of Sub remain unclear. Ultimately, signals from both CA1 and Sub are conveyed either directly or through EC LV to different cortical and subcortical areas for region-specific processing and long-term consolidation (Cappaert et al., 2015; Kitamura et al., 2017).

1.2 The neurobiology of declarative memory

1.2.1 Types of memory

In everyday use the term ‘memory’ is commonly used to describe the ability to remember the past. A wealth of psychological and neurobiological research into the underlying mechanisms, however, has revealed that memory is not a single entity but rather a collection of systems working together to enable the various aspects of remembering (Squire and Shrager, 2008). These aspects can be classified in a number of ways to emphasize specific distinctions between different types of memory (Squire and Shrager, 2008).

Memories can be conscious or subconscious. Conscious or declarative memories are a collection of knowledge about facts and events that can be consciously recalled (Squire and Shrager, 2008). Knowledge about general facts is referred to as semantic and knowledge about past events as episodic memory (Roediger et al., 2008). Declarative memories depend on diencephalic and cortical networks, including the hippocampal-entorhinal system (Squire and Shrager, 2008). Subconscious or nondeclarative memories encompass a variety of skills, acquired reflexes or representations that cannot be consciously recalled and do not require reflection on the past for their expression (Squire and Shrager, 2008). Examples of these include abilities like knowing how to ride a bicycle, conditioned responses such as anticipatory blinking in response to a tone that repeatedly precedes a mild airpuff to the eye and priming where the ability to produce a word is improved by its prior inadvertent presentation. Depending on the specific type of nondeclarative memory involved, engaged networks can be cerebellar, striatal, brain stem and in some cases also neocortical.

Nondeclarative memories do not, however, depend on the hippocampal-entorhinal system and are generally spared in patients with amnesia (Squire and Zola-Morgan, 2008).

A second common aspect used to distinguish memories is their temporal duration. Short-term memories are only retained for a brief period of time and are rapidly lost if not repeated or rehearsed (Roediger et al., 2008). They generally represent information that a person is consciously aware of and have a relatively small limit to their capacity. A closely related term that is sometimes synonymous with short-term memory is working memory. Working memory encompasses short-term memory but additionally requires the stored information to be manipulated, such as when mentally solving a mathematical equation. Circuits underlying short-term memory have not been unambiguously elucidated. Long-term memories, in contrast, do not have a temporal limit to their retention and also lack apparent restrictions to their capacity. They include both declarative and nondeclarative memories. Declarative long-term memories, including both semantic and episodic representations, are typically not part of actual conscious content but can be consciously recalled. Long-term episodic memory formation is the canonical memory process attributed to the hippocampal-entorhinal system. (Roediger et al., 2008).

1.2.2 Neural circuits underlying short-term and working memory

Despite significant research, the exact mechanisms involved in the encoding and retention of short-term memories remain unclear and it is generally believed that they engage a number of different cortical areas. Information from a single sensory modality entering short-term memory is likely represented in the same cortical region where it is initially processed, including higher sensory and primary association areas (Jonides et al., 2008). This suggests that patients with hippocampal-entorhinal lesions should have intact short-term memory which indeed seemed to be the case in early studies. For example, patient H.M. was able to remember the number '584' for several minutes by keeping the information continuously in his mind. A brief period later after being distracted, however, he failed to remember both the number as well as any mnemonic schemes he had devised for holding the number in mind (Squire and Zola-Morgan, 2008). Based on these initial findings it was postulated that short-term memory does not depend on the hippocampal-entorhinal system (Jonides et al., 2008). More recent studies, however, have challenged this idea, demonstrating that the hippocampus is involved in the short-term encoding and retrieval of

novel associations (Hannula and Ranganath, 2008) and in short-term spatial memory (Hartley et al., 2007). Together, these findings suggest that while simple short-term memory tasks involving unimodal sensory processing might not require hippocampal engagement, multimodal tasks involving the generation of novel associations do appear to require hippocampal participation.

The formation of novel representations for both short- and long-term memory highly likely takes place in area CA3 (Rebola et al., 2017) which, as previously described, transforms multimodal entorhinal signals into the coherent firing of cell ensembles (see Section 1.1.2.4). The encoded representations are subsequently recalled by executive signals from the prefrontal cortex (Jonides et al., 2008) which propagate to area CA3 via direct entorhinal projections from EC LII and activate the memory engram (Rolls, 2013). If focus is shifted away and the short-term memory is not rehearsed, the representation decays rapidly, possibly due to either weakening of synaptic connectivity or progressive desynchronization of individual neurons forming the ensemble (Jonides et al., 2008). As working memory utilizes short-term memory, the same information storage sites are likely used by both (Eriksson et al., 2015). In the case of working memory, however, the stored information is manipulated by the prefrontal cortex which has been consistently shown to be critical for working memory (Curtis and D'Esposito, 2004; Eriksson et al., 2015). The prefrontal cortex maintains and accesses relevant information according to the requirements of the task and can additionally recruit representations from long-term memory if necessary (Eriksson et al., 2015). Similarly to short-term memories, this includes the recruitment of hippocampal representations to access associational and context-related information (Daume et al., 2024).

1.2.3 Neural circuits underlying long-term episodic memory

Episodic memories represent unique experiences that occur in daily life and combine spatial and temporal information with a wealth of details about the experience itself (Dickerson and Eichenbaum, 2010). Long-term episodic memory has consistently been found to rely on the hippocampal-entorhinal system (Dickerson and Eichenbaum, 2010). As described in the previous section, current theories suggest that both short- and long-term episodic associations are generated by the recurrent CA3 circuit (Jonides et al., 2008; Rebola et al., 2017). In the case of short-term memory, these associations decay after a brief period but if the memory engram is repeatedly reactivated, either through rehearsal or repetition, the

synaptic connections are strengthened and the engram stabilized (Rebola et al., 2017). For long-term storage, the memory trace is subsequently transferred to neocortical areas, a process referred to as systems consolidation. Interestingly, neocortical engrams appear to be formed almost concurrently with the hippocampal ensemble but they are initially in an immature form where they cannot be activated by natural retrieval cues (Kitamura et al., 2017). Over time, neocortical engrams are consolidated, allowing their activation to recall the original memory (Kitamura et al., 2017). While it has been shown that for some memories neocortical engram consolidation is paralleled by hippocampal silencing, where the hippocampal ensemble becomes inactive (Kitamura et al., 2017), the role of hippocampal engrams in long-term memory is still widely debated and might depend on the contents of specific memories (Winocur et al., 2010).

The transfer of memory engrams from area CA3 to neocortical networks is mediated by intrinsically generated reactivation of the participating cell ensembles. This reactivation comes in the form of a temporally compressed version of the original neuronal firing sequence, called a sharp wave-ripple complex (SPW-R), which appears when the animal is at rest or sleeping (Buzsáki, 2015). Within an SPW-R, the sharp wave represents the coordinated firing of a large number of interconnected principal cells, whereas the superimposed ripples are generated by the synchronous firing of inhibitory interneurons. SPW-R arise spontaneously within the CA3 network through incompletely understood mechanisms and are subsequently transmitted to area CA1 and Sub, preserving their synchrony (Buzsáki, 2015). In turn, the hippocampal output regions relay SPW-R to MEC LV, where in the case of signals originating at intermediate hippocampal levels they drive local cell populations in both layers Va and Vb (Rozov et al., 2020). The neocortical output pathway from entorhinal LVa appears to be critical for long-term memory formation as disruption of this pathway at early but not late stages of memory formation interferes with neocortical engram consolidation (Kitamura et al., 2017). It remains unclear how information contained within SPW-R is represented by LVa neurons, especially as ripple-related rhythmicity appears to be lost in LV cells (Roth et al., 2016). Because coding schemes in the hippocampus and neocortex differ, it is possible that LVa cells convert hippocampal outputs into a specific form required to drive plasticity in the neocortex (Gerlei et al., 2021).

Conclusion

Since the landmark discovery that the hippocampal-entorhinal system is critical for episodic memory formation, significant research effort has been invested into structural and functional analyses of the underlying circuits. It is now known that a diverse population of spatially tuned cell types in MEC generates an internal map of the external environment. These spatial signals are stabilized and maintained by cell ensembles in the recurrent CA3 network. Ensemble activity is ultimately consolidated in neocortical circuits, requiring the transfer of signals via MEC deep layers. Despite significant advances, both structural and functional understanding of the hippocampal-medial entorhinal system remains incomplete. This includes the organization of basic projections, illustrated by inconsistencies in recent reports on the canonical hippocampal output projection to MEC LV. The present thesis clarifies previous inconsistencies and extends our knowledge of hippocampal-medial entorhinal connectivity, providing a detailed characterization of the hippocampal output pathway to MEC deep layers.

AIMS OF THE STUDY

Functional organization of hippocampal projections to MEC layer V

The hippocampal projection to MEC LV forms a major hippocampal output pathway that is critical for systems consolidation (Kitamura et al., 2017; Roy et al., 2017). LV can be divided into two sublayers – LVa and LVb. Principal cells in LVa project to the neocortex (Ohara et al., 2018; Sürmeli et al., 2015) and this pathway has been shown to mediate the transfer of hippocampal representations to cortical areas for long-term storage (Kitamura et al., 2017). LVb neurons, in contrast, are a source of intraentorhinal projections which target superficial MEC layers (Ohara et al., 2021, 2018). Importantly, direct connections between LVb and LVa principal neurons are sparse, indicating that signals conveyed to the two sublayers are processed in parallel streams of activity (Rozov et al., 2020). How hippocampal outputs target each sublayer therefore has major implications for the flow of hippocampal information to local entorhinal versus remote neocortical networks.

It was initially suggested that projections from dorsal CA1 and Sub exclusively target neurons in LVb (Sürmeli et al., 2015). My own data subsequently confirmed the preferential targeting of LVb neurons by dorsal hippocampal outputs (Rozov et al., 2020), raising the question how hippocampal output signals reach the LVa neocortical output pathway. In the same study we showed that projections from CA1 and Sub at intermediate hippocampal levels innervate LVa and LVb cells with similar strength (Rozov et al., 2020). This suggested that sublayer specificity of the hippocampal projection to MEC LV might depend on the hippocampal level of origin, such that outputs to LVa might disproportionately originate from ventral hippocampal levels.

In order to elucidate these questions, the first aim of the present thesis was thus to determine the functional organization of the hippocampal output projection to MEC LV along the dorsoventral hippocampal and entorhinal axes, focusing on two key questions:

1. How are projections from the dorsal and ventral hippocampal output structures to LV functionally organized along the dorsoventral MEC axis?
2. Do these projections show differential distribution between the Va and Vb sublayers?

Functional organization of MEC layer VI

Although the majority of hippocampal output projections to MEC distribute in LV, projections from both CA1 and Sub have consistently been shown to also target LVI (Ben-Simon et al., 2022; O'Reilly et al., 2013; Swanson and Cowan, 1977; Witter et al., 2000). Indeed, stimulation of the hippocampal output pathway appears to elicit responses not only in LV but also LVI neurons (Kloosterman et al., 2003a; Tu et al., 2009). The organization of this projection along the dorsoventral hippocampal and entorhinal axes, however, has not been studied in detail and the innervation of LVI neurons by hippocampal output signals remains unclear.

Only a single study has so far systematically analyzed the efferent connectivity of LVI neurons, finding that they project to all subfields of HF (Ben-Simon et al., 2022). The functional connectivity of LVI neurons within the MEC deep layer circuitry, however, remains poorly studied. In view of the larger MEC deep layer network, functional connections from LVI neurons to either LVb or LVa cells would allow hippocampal signals arriving in LVI to modulate information flow to MEC superficial layers or to neocortical networks, respectively. Conversely, excitatory connections from either LVb or LVa neurons to LVI cells would provide an additional pathway through which signals processed in either layer could influence hippocampal circuits.

The second aim of the present thesis was thus to determine the functional organization of the hippocampal projection to MEC LVI along the dorsoventral hippocampal and entorhinal axes and to examine functional connectivity between layers VI and V. I specifically focused on the following two questions:

1. How are projections from the dorsal and ventral hippocampal output structures to LVI functionally organized along the dorsoventral MEC axis?
2. How are LVI principal cells and fast-spiking interneurons integrated into the MEC deep layer circuitry?

CONTRIBUTIONS OF OTHERS

An integral part of the study summarized in the present thesis is a complementary anatomical and optogenetic analysis of hippocampal projections to MEC deep layers. All anatomical tracing experiments were performed by Dr. Shinya Ohara in the laboratories of Prof. Menno Witter at the Kavli Institute for Systems Neuroscience of the NTNU Norwegian University of Science and Technology in Trondheim, Norway and Prof. Ken-Ichiro Tsutsui at the Laboratory of Systems Neuroscience of Tohoku University in Sendai, Japan. For the sake of completeness and to ensure that all conclusions and implications of the study are fully supported, a significant fraction of anatomical tracing data related to MEC were included in this thesis.

Additional contributions were made by the following individuals and institutions:

- The Rbp4-Cre mouse line was kindly provided by Prof. Alexander Groh from the Institute of Physiology and Pathophysiology of Heidelberg University. The PV-Cre.tdTomato mouse line was commercially purchased. All animals were housed and bred at the Interfaculty Biomedical Facility of Heidelberg University.
- Assistance with statistical analyses, the preparation of figures and general guidance in his role as a supervisor was provided by Dr. Alexei Egorov in the laboratory of Prof. Andreas Draguhn.
- Technical assistance with immunohistochemical stainings of brain slices was provided by Nadine Zuber in the laboratory of Prof. Andreas Draguhn.

2 MATERIALS AND METHODS

2.1 Electrophysiology

2.1.1 Animals used in electrophysiological experiments

All patch clamp recordings in optogenetic experiments were performed in brain slices obtained from 9-12 week old male mice. To study the innervation of MEC LV and LVI principal cells by hippocampal projections, I used C57BL/6N mice. To characterize the innervation of parvalbumin-positive fast-spiking (FS) interneurons, I used B6.129P2-Pvalb^{tm1(cre)}Arbr/J x B6.Cg-Gt(ROSA)26Sortm14(CAG-tdTomato)/Hze/J (PV-Cre. tdTomato) mice which express the red fluorescent protein tandem dimer Tomato (tdTomato) under the parvalbumin (PV) promoter, allowing visual identification of the PV-expressing FS interneuron population. I optogenetically tested projections from LVa to LVI principal neurons in B6.FVB/CD1-Tg(Rbp4-cre)KL100Gsat/Mmucd (Rbp4-Cre) mice which in MEC express Cre recombinase specifically in LVa principal neurons (Tsoi et al., 2022), allowing direct labeling of this neuronal population.

All paired patch clamp recordings were performed in brain slices obtained from 4-8 week old male mice. I used C57BL/6N mice for paired recordings between principal cells and PV-Cre. tdTomato mice for paired recordings between principal cells and FS interneurons. C57BL/6N mice were purchased from Charles River Laboratories (Sulzfeld, Germany). The PV-Cre. tdTomato mouse line had been originally commercially acquired and subsequently maintained by breeding at the Interfaculty Biomedical Facility of Heidelberg University. The Rbp4-Cre mouse line was a generous gift from Prof. Alexander Groh from the Institute of Physiology and Pathophysiology of Heidelberg University. Mice were housed in groups of up to three animals per cage on a reversed 12 h light/dark cycle with ad libitum access to food and water. All animal experiments were approved by the state government of Baden-Württemberg (Projects G206/20 and G58/21) and were conducted in compliance with German law and the European Communities Council Directive.

2.1.2 Surgical procedures and delivery of viral vectors

For the delivery of viral vectors to target brain areas I used stereotaxic surgery. 30 minutes before and 3 hours after each operation I injected the mice with the opioid receptor modulator buprenorphine (0.1 mg/kg buprenorphine hydrochloride, Temgesic, Indivior), commonly used to relieve pain. I then deeply anesthetized the animals with vaporized isoflurane and mounted them in a stereotaxic frame. Anesthesia was maintained throughout the operation by a continuous flow of isoflurane at concentrations between 1.5–2.5%. After fixing the head, I exposed the skull and drilled a small burr hole above each injection site. For injections targeting dorsal or ventral area CA1, 70–100 nl of the adeno-associated virus (AAV) AAV5-CaMKIIa-hChR2(H134R)-EYFP (UNC vector core, Karl Deisseroth virus stock/Addgene #26969), expressing humanized channelrhodopsin-2 (hChR2) conjugated to enhanced yellow fluorescent protein (EYFP) under the calcium/calmodulin-dependent protein kinase II subunit alpha (CaMKIIa) promoter, was injected at a rate of 100 nl per minute using a stainless steel needle (NF33BV, inner tip diameter = 115 μ m, WPI, Sarasota, FL, USA) connected to a 10 μ l NanoFil Syringe (WPI). Injections targeting area CA1 in the dorsal HF were positioned at coordinates anteroposterior (AP) = -1.5 mm; mediolateral (ML) = \pm 1.2 mm; dorsoventral (DV) = -1.25 mm or AP = -2 mm; ML = \pm 2 mm; DV = -1.5 mm, while injections into ventral CA1 were positioned at coordinates AP = -2.9 mm; ML = \pm 3.4 mm; DV = -4.0 mm. For injections targeting MEC LVa in Rbp4-Cre mice, 150 nl of the Cre-dependent AAV2-Efla-DIO-hChR2(H134R)-EYFP (UNC vector core, Karl Deisseroth virus stock) was injected under identical conditions as before. Injections into ventral LVa were positioned at coordinates AP = -4.3 mm; ML = \pm 3.25 mm; DV = -4.0 mm and injections into dorsal LVa at coordinates AP = -4.4 mm; ML = \pm 3.25 mm; DV = -2.6 mm. To allow the tissue to absorb the viral solution, the needle was left in place for 10 minutes after each injection. I subsequently slowly retracted the needle and sutured the wound. The flow of isoflurane was stopped and the animal allowed to recover from anesthesia, after which it was returned to its home cage. I sacrificed the mice a minimum of two weeks after virus injections to allow adequate expression of the hChR2-EYFP construct.

2.1.3 Preparation of mouse brain slices

I sacrificed mice by decapitation under deep anesthesia induced by the inhalation of CO₂. Following decapitation, the skull was rapidly opened, the brain extracted and the intact brain

immediately transferred to an ice-cold oxygenated cutting solution containing (in mM): 140 K-gluconate, 15 Na-gluconate, 4 NaCl, 10 4-(2-hydroxyethyl)-1-piperazineethanesulfonic acid (HEPES) and 0.2 ethylene-glycol-bis-tetraacetic acid (EGTA), saturated with carbogen gas (95% O₂ and 5% CO₂, pH 7.3). I subsequently prepared the brains for mounting to the specimen disc of a vibratome slicer (Leica VT1200S, Nussloch, Germany). For optogenetic experiments, I removed the cerebellum and the frontal one third of the brain with straight coronal blocking cuts (Figure 5A, top). The dorsal portion of the brain above the hippocampi was then removed with another straight blocking cut, creating a flat transverse surface that was used to attach the brain to the specimen disc (Figure 5A, bottom).

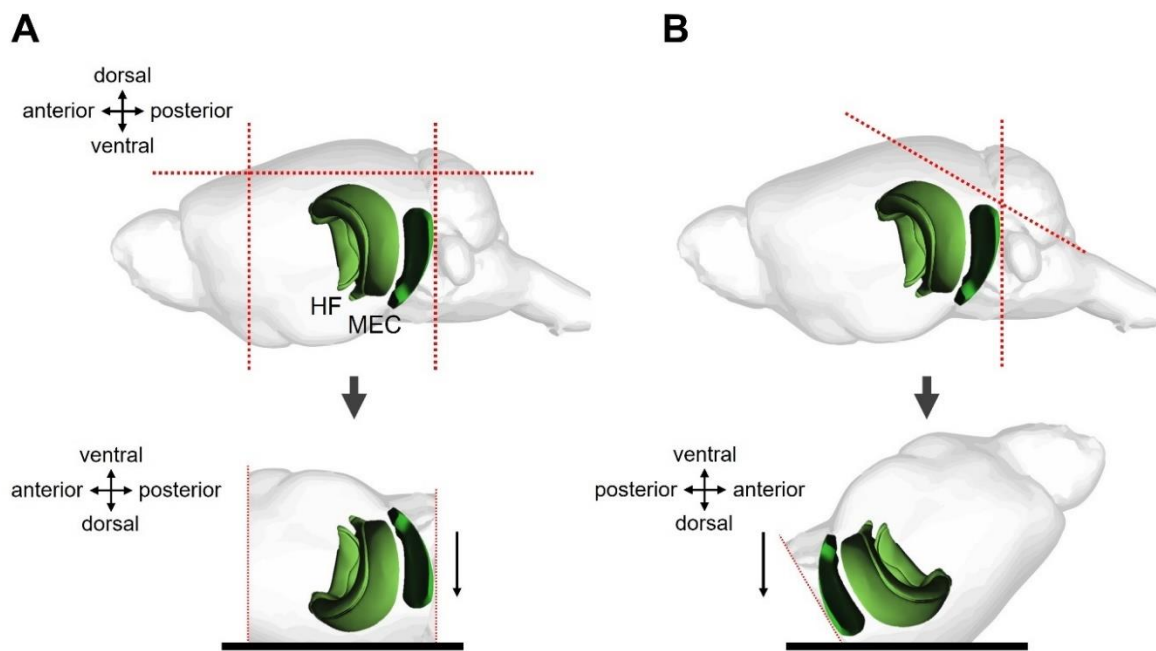


Figure 5. Sectioning planes used to prepare slices for electrophysiological experiments from the mouse medial entorhinal cortex. (A) Illustration of the configuration used to section the brain for optogenetic experiments. Top: three straight blocking cuts (red dashed lines) were made to remove the cerebellum, the frontal part of the brain and the dorsal portion of the brain above the hippocampi. Bottom: the flat dorsal surface created by the dorsal blocking cut was used to attach the brain to the specimen disc (thick black line) of a vibratome slicer. The brain was then sectioned horizontally from ventral to dorsal (thin black arrow) in 350 μ m steps. (B) Sectioning configuration used for paired recordings. Top: a straight blocking cut was first made to remove the cerebellum, followed by a sagittal cut to separate the hemispheres (not shown). For each hemisphere, the dorsal part of the brain above MEC was removed using a \sim 25-30° blocking cut oriented caudally relative to the transverse plane. Bottom: the resulting angled surface was used to attach the brain to the specimen disc. Slices were cut horizontally from ventral to dorsal in 300 μ m steps. Models of HF and MEC were adapted from Allen Brain Explorer (<http://connectivity.brain-map.org/3d-viewer>).

I then sectioned the brain in 350 μm steps, resulting in level slices relative to the transverse plane. Slices in all experiments where hippocampal-medial entorhinal projections were investigated were taken at four distinct dorsoventral levels (Figures 10C, 10D, 16C and 16D). For paired recordings, I adjusted the cutting angle to optimally preserve axonal connectivity. After removal of the cerebellum, I separated the hemispheres with a sagittal blocking cut. A dorso-posterior portion of each hemisphere was then removed at $\sim 25\text{-}30^\circ$ caudally relative to the transverse plane (Figure 5B, top), creating an angled surface which was used to attach the brain to the specimen disc (Figure 5B, bottom). I sectioned the brain in 300 μm steps, resulting in angled slices relative to the transverse plane. Cut slices were incubated for 20 min at 34 $^\circ\text{C}$ in carbogen-saturated artificial cerebrospinal fluid (ACSF) containing (in mM): 124 NaCl, 3 KCl, 1.6 CaCl_2 , 1.8 MgSO_4 , 10 glucose, 1.25 NaH_2PO_4 and 26 NaHCO_3 (pH 7.4 at 34 $^\circ\text{C}$) and subsequently stored in room temperature (RT) carbogen-saturated ACSF for up to six hours. Slices were allowed to recover for a minimum of one hour before the start of electrophysiological recordings.

2.1.4 Patch clamp recordings

2.1.4.1 Overview of the patch clamp technique

Patch clamp recordings are an established technique for studying ionic currents mediated by ion channels embedded in biological membranes. Patch clamping was originally developed by Erwin Neher and Bert Sakmann who used it to study single ion channel dynamics (Neher and Sakmann, 1976) but the technique has since been widely adopted for living cells both in tissue culture and in slices prepared from various animal tissue. Patch clamping involves bringing a microelectrode inserted into a hollow glass micropipette filled with an artificial solution into electrical contact with an individual cell (Figure 6). In the first stage, the micropipette is brought into close proximity of the target cell (Figure 6A, left). Positive pressure applied to the pipette interior forces the pipette solution to stream out of the pipette tip, preventing contamination of the tip by surrounding tissue or the membrane of the target cell. In the second stage, positive pressure is released and negative pressure gently applied which causes the cellular membrane to come into close contact with the pipette tip (Figure 6A, right). The patch of membrane in contact with the pipette tip ultimately forms a tight seal, electrically isolating it from the surrounding environment. While it is possible to record major electrical events, such as action potentials, in this configuration, the highly insulating

nature of the plasma membrane prevents the detection of finer electrical fluctuations. Most patch clamp experiments therefore proceed to whole-cell configuration which is achieved by applying a burst of negative pressure that ruptures the patch of membrane under the pipette tip while leaving the rest of the membrane intact (Figure 6B). This brings the microelectrode into direct electrical contact with the interior of the cell, allowing even miniature currents induced by the activation of a single synapse to be recorded.

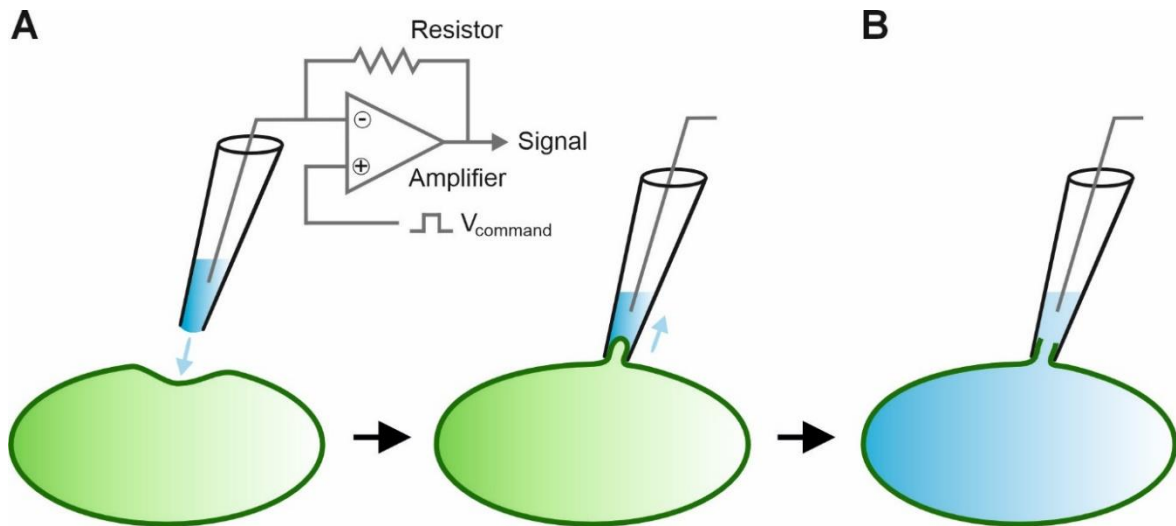


Figure 6. Overview of the whole-cell patch clamp technique. (A) Left: in patch clamp recordings, a hollow glass micropipette (black, not drawn to scale) is filled with an artificial solution (blue) and a microelectrode (gray) is inserted into the filled pipette. The microelectrode is connected to a high resistance feedback resistor, enabling the measurement of very small currents. When the circuitry is operated in voltage clamp mode, a command voltage (V_{command}) can be set through an amplifier to hold a patched cell (green) at a defined potential. In the initial stage of the patching process, positive pressure is applied to the pipette interior and the pipette is brought into close vicinity of the target cell. Right: positive pressure is then released and negative pressure applied, causing the cellular membrane to form a tight seal with the pipette tip. (B) In the final stage, a brief burst of negative pressure ruptures the patch of membrane under the pipette tip while leaving the rest of the membrane intact. This brings the microelectrode into direct electrical contact with the interior of the cell.

The electrical activity is measured by a patch clamp amplifier to which the microelectrode is connected. A typical patch clamp amplifier can be operated in either voltage clamp or current clamp mode. In voltage clamp, a command potential is set by the experimenter to hold the patched cell at a defined potential. Any perturbations to this potential are automatically corrected by the circuitry by injecting an identical amount of current with the opposite sign into the cell (Figure 6A). In current clamp, the amplifier measures changes in

membrane potential in response to current injections defined by the experimenter. The amount of injected current can be zero, corresponding to the resting membrane potential (RMP) of the cell, or large enough to evoke an action potential. The induction of action potentials allows intrinsic firing behavior or connectivity with other cells to be studied. Patch clamp recordings are often combined with optogenetic techniques to functionally interrogate neuronal circuits. This involves introducing light-gated ion channels, such as the cation channel channelrhodopsin (ChR), into a population of putative presynaptic neurons either by viral transduction or generation of a transgenic mouse line. The affected neurons typically express ChR in the soma and axon, where it can be activated by illuminating these structures with light of appropriate wavelength, triggering an action potential. During an experiment, a target neuron is patched and ChR in the putative presynaptic neurons activated. If functional synapses between the presynaptic neurons and the target cell are present, synaptic transmission induced by presynaptic action potentials triggers synaptic currents in the target cell which are recorded by the microelectrode.

2.1.4.2 Experimental details

For patch clamp recordings I transferred individual slices to a submerged recording chamber which was continuously superfused with carbogen-saturated ACSF at 32 ± 1 °C. Excitatory neurons were visualized through a 40x/0.8-NA objective attached to an upright microscope (BX-51WI, Olympus, Japan) using infrared differential interference contrast (IR-DIC) microscopy. To identify FS interneurons in PV-Cre.tdTomato mice, I illuminated the slice with a 565 nm LED (M565L3, ThorLabs, Newton, NJ, USA) through the 40x objective, causing tdTomato in FS cells to fluoresce. I performed all whole-cell patch clamp recordings using AgCl-coated silver wire electrodes inserted into heat-pulled borosilicate glass pipettes (GB200F-8P, Science Products, Hofheim, Germany) with a resistance of 3–4 M Ω . In most experiments the pipettes were filled with a K-gluconate based intracellular solution containing (in mM): 144 K-gluconate, 4 NaCl, 10 HEPES, 4 Mg-adenosine-5-triphosphate (Mg-ATP), 0.3 Na-guanosine-5-triphosphate (Na-GTP) and 10 Na₂-phosphocreatine (pH 7.3, KOH, calculated liquid junction potential -17 mV). For N-methyl-D-aspartate (NMDA) receptor current recordings a Cs-based intracellular solution was used containing (in mM): 144 Cs-gluconate, 4 CsCl, 10 HEPES, 4 Mg-ATP, 0.3 Na-GTP and 10 Na₂-phosphocreatine (pH 7.3, CsOH, calculated liquid junction potential -17 mV). To improve the signal-to-noise

ratio of inhibitory connections, paired recordings between excitatory and FS interneurons were made with a K-gluconate based intracellular solution containing an elevated concentration of Cl⁻ (in mM): 110 K-gluconate, 30 KCl, 8 NaCl, 10 HEPES, 4 Mg-ATP, 0.3 Na-GTP and 10 Na₂-phosphocreatine (pH 7.3, KOH).

Due to inherent limitations of the cutting procedure, slices used in optogenetic experiments did not generally include the hippocampal injection site and thus the somata of infected neurons. However, axonal fibers of infected hippocampal neurons expressing hChR2-EYFP in individual slices remained intact and could be reliably excited. For the activation of both hippocampal and LVA axons, I illuminated the slice above the recording location with a TTL-controlled blue LED (470 nm, M470L4, ThorLabs) through the 40x objective. In some experiments, light intensity was increased stepwise from 0.6 to 11.7 mW/mm² and at each intensity five 1 ms pulses at 10 Hz were repeated three times. In other experiments, only maximum light intensity (11.7 mW/mm²) was used and the same pulse train was repeated ten times. I recorded light-evoked excitatory postsynaptic currents (EPSCs) in voltage-clamp mode while holding the cells at -70 mV. Series resistance compensation was not used and recordings were discarded if the resistance changed by >20%. All recordings were made with an ELC-03XS amplifier (npi electronics, Tamm, Germany) with currents low-pass filtered at 8 kHz. Data were digitized at 20 kHz using a POWER1401 mkII analog-to-digital converter (Cambridge Electronic Design (CED), Cambridge, UK) and saved to a computer using Signal4 and Spike2 (v7) software (CED).

Before paired recordings, I visually assessed the general integrity of intra- and interlaminar axonal fibers in each slice and discarded slices where fibers did not run parallel to the slice surface. I then patched a pair of cells within LVI or in layers VI and V. Patched cells were held in current-clamp mode at RMP which was measured directly after achieving whole-cell configuration without injecting current and without correcting for liquid junction potential. During recordings, series resistance was compensated using the bridge circuitry of the amplifier. I analyzed intrinsic firing behavior by measuring voltage deflections resulting from 25 pA (500 ms) current steps injected through the microelectrode. I subsequently tested connections between pairs of cells by stimulating each cell with a minimum of 50 consecutive sweeps of five 10 Hz suprathreshold current pulses. To analyze excitatory or inhibitory postsynaptic potentials (PSPs), individual sweeps were averaged. All recordings were made with an ELC-03XS and an SEC-05X amplifier (npi electronics) with voltages

low-pass filtered at 3 kHz. Data were digitized at 20 kHz using the POWER1401 mkII analog-to-digital converter and saved to a computer using Signal4 software.

I identified excitatory neurons during recordings based on their location, shape of cell body and firing properties. FS interneurons in PV-Cre.tdTomato mice were identified based on their fluorescence in combination with a typical non-adapting high-frequency firing pattern (Figure A8B). In all recordings, intracellular solutions were supplemented with biocytin (1–5%, Cat. no. B4261, Sigma-Aldrich, Taufkirchen, Germany) to enable the analysis of cell morphology and location by post hoc immunolabeling. Slices were additionally labeled for Ctip2 to precisely delineate the sublayer Vb. LVI excitatory neurons featured a large soma, horizontally ramifying dendrites without a clear apical dendrite (Figures 21B and 24B) and a delayed firing pattern without a sag (Table B1). These properties allowed LVI neurons to be reliably distinguished from neighboring LVb cells which were typically smaller, had a prominent apical dendrite and fired without an extended delay (Ohara et al., 2021). LVb neurons, in turn, were easily distinguished from LVa cells as the latter again featured a large soma, horizontally ramifying dendrites and a distinct firing pattern (Ohara et al., 2021).

2.1.5 Staining and imaging of recorded slices

Brain slices containing biocytin-filled cells were fixed in 4% paraformaldehyde (PFA) in 0.1 M phosphate buffer (PB) for 45–60 min at RT and stored in phosphate-buffered saline (PBS) containing (in mM): 137 NaCl, 2.7 KCl, 8 NaH₂PO₄ (pH 7.2 at 4 °C). For immunolabeling, slices were pretreated in a blocking solution (5% goat serum and 0.3% Triton X-100 in PBS) for 2 h at RT, followed by three 15 min washing steps in PBS. The slices were then incubated overnight (>16 h at RT) with the primary antibody (1:1000, rat anti-Ctip2, #ab18465, Abcam, Cambridge, UK) diluted in antibody solution (1% goat serum and 0.2% Triton X-100 in PBS). The following day, slices were again washed in PBS (3 × 15 min) and subsequently treated with the secondary antibody (streptavidin-conjugated Alexa Fluor 546 (1:1000, #S11225, Invitrogen, Waltham, MA, USA) or Alexa Fluor 647 (1:1000, anti-rat, Invitrogen #A21247)) in the antibody solution for 2 h at RT. The immunolabeled slices were washed in PBS (3 × 15 min) and incubated with 4,6-diamidino-2-phenylindole (DAPI; 1:10 000, Carl Roth, Germany) for 2 min at RT. Finally, slices were quickly rinsed with PBS and embedded in Mowiol 4-88 (Sigma-Aldrich). I imaged the embedded slices with a C2 Nikon confocal microscope (Nikon Imaging Center at Heidelberg University) at 2048x2048 pixel

resolution using 4x (0.13 NA), 10x (0.45 NA) or 20x (0.75 NA) objectives in air. At 20x magnification multiple confocal images were collected as image stacks (2 μm z-steps). I subsequently merged the image stacks as maximum intensity projections and analyzed the images with ImageJ/Fiji (Wayne Rasband, NIH, USA, open source). The section was originally published in Ohara et al., 2023 and has been adopted with minor modifications.

2.1.6 Analysis of electrophysiological data

I analyzed all electrophysiological data manually from raw traces using Signal4 and Spike2 (v7) software. For the analysis of optogenetic recordings, I used the first light-evoked EPSC of the five-pulse-train, averaged across individual sweeps. EPSC amplitudes were defined as the difference between EPSC peak and event-free baseline before EPSC onset, whereas latency values represent the time interval between the onset of light pulse and the onset of EPSC. I measured both parameters by manually placing horizontal or vertical cursors. Responses with a latency <3.5 ms were classified as monosynaptic and responses >3.5 ms polysynaptic (Justus et al., 2017). However, across my optogenetic experiments nearly all recorded cells exhibited a latency either <3.0 ms or >4.0 ms (Figures A7B and A7C), supporting a clear distinction between mono- and polysynaptic responses based on latency. I measured latencies and 20%-80% rise times at maximum light intensity. Cells with a holding current >300 pA at a holding potential of -70 mV or a series resistance >30 M Ω were discarded. Because there were no significant differences in light-evoked EPSC amplitudes between the caudal and rostral dorsal hippocampal injection locations, I pooled data for both injection locations into a single group.

In the case of paired recordings, prior to connectivity analysis I carefully examined the axonal arbors of all recorded cells and excluded cells with truncated axons as presynaptic neurons. I defined the amplitudes of PSPs analogously to EPSCs and measured them for all PSPs induced by the presynaptic train of five action potentials by manually placing horizontal cursors. Latency values were measured for the first PSP using vertical cursors and represent the time interval between the peak of the presynaptic action potential and the onset of the PSP. Cells were discarded if their RMP was more positive than -55 mV or they had a series resistance >30 M Ω .

Quantitative electrophysiological data from multiple recorded slices are given as median, data in figures are presented as median, 25th and 75th percentile [P25; P75] as well as

individual values. I performed statistical analyses using GraphPad (InStat, San Diego, CA, USA) or SigmaPlot software (Systat, Chicago, IL, USA). Two-tailed one-sample t-test was used to test LVI neuron amplitudes normalized to LVa or LVb responses. Two-tailed unpaired t-test was used for statistical comparisons of two groups with normal and Mann-Whitney U test for comparisons of two groups with non-normal distributions. Responses of LVa and LVb neurons at different slice levels along the dorsoventral axis were analyzed with Kruskal-Wallis Test followed by Dunn's pairwise comparison test. Normalized responses of LVb neurons at different dorsoventral levels were tested with one-way analysis of variance (ANOVA) followed by Bonferroni's multiple comparison test. LVa and LVb neuron responses at different dorsoventral slice levels were compared to each other using two-way ANOVA followed by Bonferroni's multiple comparison test. Data for two-way ANOVA were log₁₀-transformed to normal distribution. Short-term plasticity induced by the presynaptic train of five action potentials in paired recordings was tested with Friedman repeated measures ANOVA on ranks. Finally, differences in connectivity probabilities between the dorsal and ventral MEC in paired recordings were compared using Fisher's exact test. A p value <0.05 was regarded as significant and thresholds for significance were placed as follows: *p < 0.05, **p < 0.01 and ***p < 0.001, ns, not significant. This entire section was originally published in Ohara et al., 2023 or will be published in Rannap et al. (in revision) and has been adopted with minor modifications.

2.2 Neuroanatomical tracings

Neuroanatomical tract tracing is a standard method for the study of connections between neuronal populations. Classically, the technique involves delivering small organic molecules to specific regions of the brain, most commonly by microinjection, where they are taken up by neurons in the vicinity of the injection site. Once in the interior of the neuron, the molecules diffuse or are actively transported throughout neuronal processes, including the axon. For visualization, the molecules can be directly conjugated to dyes or fluorescent proteins or stained by immunohistochemical or other methods. This results in detailed labeling of axonal projections of the originally affected neuronal population throughout the brain. More recently with advances in recombinant DNA technology, viral tracers have become commonplace due to their high degree of specificity and permanent reporter protein expression (Saleeba et al., 2019). Viral tracers are genetically modified viruses whose

genome has been altered to exclude genes responsible for replication of the virus and include a genetic sequence encoding for the reporter protein. The reporter is typically a fluorescent protein that can be expressed independently for general axonal labeling or be conjugated to a cellular protein for the labeling of specific axonal structures, such as synaptophysin for the labeling of synapses. The reporter protein gene can be controlled by a variety of ubiquitous or cell-type specific neuronal promoters and be conditionally activated by integrating recombination sequences for Cre or a similar site specific recombinase (Saleeba et al., 2019). This enables precise cell-type specific axonal tracing not possible with classical tracers.

2.2.1 Animals used in neuroanatomical tracing experiments

Projections from the hippocampus to MEC layers V and VI were anatomically characterized using adult male C57BL/6N mice and adult male or female Sprague Dawley rats. Mice and rats were purchased from Japan SLC (Shizuoka, Japan) or Charles River Laboratories (Sulzfeld, Germany). The animals were group housed on a reversed 12 h light/dark cycle with ad libitum access to food and water. All animal experiments were approved by the Tohoku University Center for Laboratory Animal Research (Projects: 2017LsA-017; 2017LsA-018) and were conducted in accordance with Tohoku University Guidelines for Animal Care and Use, the European Communities Council Directive and the Norwegian Experiments on Animals Act.

2.2.2 Surgical procedures and delivery of tracers or viral vectors

Neuroanatomical tracers and viral vectors were delivered to dorsal or ventral hippocampal area CA1 or Sub using stereotaxic surgery which was performed similarly to stereotaxic operations described for electrophysiology (see Section 2.1.2). Before each operation, animals were injected subcutaneously with buprenorphine hydrochloride (0.1 mg/kg), meloxicam (1 mg/kg Metacam, Boehringer Ingelheim Vetmedica, Ingelheim am Rhein, Germany) and at the incision site with bupivacaine hydrochloride (1 mg/kg Marcain, AstraZeneca, Cambridge, UK) to relieve pain. Injected tracers were anterogradely labeling and included either 2.5% phaseolus vulgaris leucoagglutinin (PHA-L; #L-1110, Vector Laboratories, Newark, CA, USA) or 3.5–5.0% 10 kDa biotinylated dextran amine (BDA; Invitrogen #D1956) which were injected iontophoretically with positive 6–12 mA current

pulses (6 s on, 6 s off) for 15 min. In some mouse experiments, 200 nl of an AAV cocktail consisting of AAV1-Syn1(S)-FLEX-tdTomato-T2A-SypEGFP (1.8×10^{13} GC/ml, 133 nl, Addgene #51509) and AAV9.CaMKII 0.4.Cre (2.1×10^{13} GC/ml, 67 nl, Addgene #105558) was pressure injected using a glass micropipette (outer tip diameter = 20–40 μ m) connected to a 1 μ l Hamilton microsyringe. After each injection, the pipette was left in place for 15 minutes before being withdrawn. The wound was sutured and the animal was allowed to recover from anesthesia, after which it was returned to its home cage. Animals were sacrificed ten days after tracer or 3–4 weeks after viral injections. The section was originally published in Ohara et al., 2023 and has been adopted with minor modifications.

2.2.3 Staining and imaging of neuroanatomical tracing samples

Injected animals were anesthetized with isoflurane and euthanized with a lethal intraperitoneal injection of pentobarbital (100 mg/kg). The animals were subsequently transcardially perfused, first with Ringer's solution (0.85% NaCl, 0.025% KCl, 0.02% NaHCO₃) and then with 4% PFA in 0.1 M PB. The perfused brains were removed from the skull and post-fixed overnight in PFA. After fixing, brains were put in a cryo-protective solution containing 20% glycerol and 2% dimethylsulfoxid (DMSO) diluted in 0.125 M PB and 40 μ m sections spaced 240 μ m apart were cut with a freezing microtome (Thermo Scientific, Pittsburgh, PA, USA). Sections were cut in either the horizontal or sagittal plane throughout the dorsoventral or mediolateral extent of MEC.

Sections from animals injected with PHA-L were stained with primary (1:1000, rabbit anti-PHA-L, Vector Laboratories #AS-2300) and secondary antibodies (1:400, Alexa Fluor 647 goat anti-rabbit IgG, #111-605-144, Jackson ImmunoResearch, West Grove, PA, USA). Sections containing neurons traced with BDA were labeled with Cy3-streptavidin (1:400, Jackson ImmunoResearch #016-160-084). GFP signal was enhanced using a primary (1:500, mouse anti-GFP, Invitrogen #A11120) and a secondary antibody (1:400, Cy3 goat anti-mouse IgG, Jackson ImmunoResearch #115-165-146). To delineate individual MEC layers, sections were stained with antibodies against Fox-3 (NeuN), which is expressed in a large majority of all neuronal cell types, and PCP-4 which is expressed by neurons in MEC layers Vb and III (Ohara et al., 2021). The primary antibodies included guinea pig anti-NeuN (1:1000, #ABN90P, Merck Millipore, Burlington, MA, USA), mouse anti-NeuN (1:1000, Merck Millipore #MAB377) and rabbit anti-PCP4 (1:300, Sigma Aldrich #HPA005792)

which were combined with corresponding secondary antibodies (Alexa Fluor 647 goat anti-guinea pig IgG, Jackson ImmunoResearch #106-605-003; Alexa Fluor 647 goat anti-mouse IgG, Jackson ImmunoResearch #115-605-003 and Alexa Fluor 647 goat anti-rabbit IgG).

For all immunostainings, floating sections were rinsed in PBS supplemented with 0.1% Triton X-100 (PBS-Tx) and subsequently treated with a blocking solution (5% goat serum in PBS-Tx) for 60 min at RT. Depending on the experiment, sections were then incubated with a primary antibody diluted in the blocking solution for 20–40 h at 4 °C. Labeled sections were repeatedly washed with PBS-Tx (3 × 10 min) and incubated with the corresponding secondary antibody, diluted in PBS-Tx, for 4–6 h at RT. The sections were subsequently washed in PBS (3 × 10 min) and prepared for imaging by mounting them on gelatin-coated slides which were coverslipped with Entellan new (#107961, Merck Chemicals, Darmstadt, Germany). Sections were imaged with the Zeiss Axio Scan Z1 automated scanner (Carl Zeiss Microscopy, Jena, Germany) using a 20x (0.8 NA) objective in air. The precise location of injection sites in horizontally or sagittally sectioned samples were determined by identifying the corresponding location of the injection site in the coronal plane using either the Waxholm space three-plane architectonic atlas of the rat hippocampal region (Boccarda et al., 2015; Kjonigsen et al., 2015; Papp et al., 2014) or Allen Brain Explorer (<http://connectivity.brain-map.org/3d-viewer>). This entire section was originally published in Ohara et al., 2023 and has been adopted with minor modifications.

2.2.4 Analysis of neuroanatomical tracing data

The distribution of labeled axons in MEC layers V and VI was quantified in either horizontal or sagittal sections spaced 240 µm apart. After identifying EC and its respective layers, EC deep layers were divided into columnar bins by first dividing layer IV into 100–200 µm wide bins and subsequently extending the bins to layers Va, Vb and VI (Figure 7). Fluorescence intensity of immunohistochemically labeled axons within each bin was quantified using ImageJ/Fiji. Intensity values for all bins were then normalized to the bin with the highest intensity in the same sample and in the case of experiments where hippocampal projections to layers Va and Vb were investigated, the normalized intensities were further plotted onto an unfolded map of EC or MEC (Figure 7). To visualize differences in labeling patterns between layers Va and Vb, individual maps for both layers were combined into a composite image using MATLAB (MathWorks, Natick, MA, USA) (Figure 7).

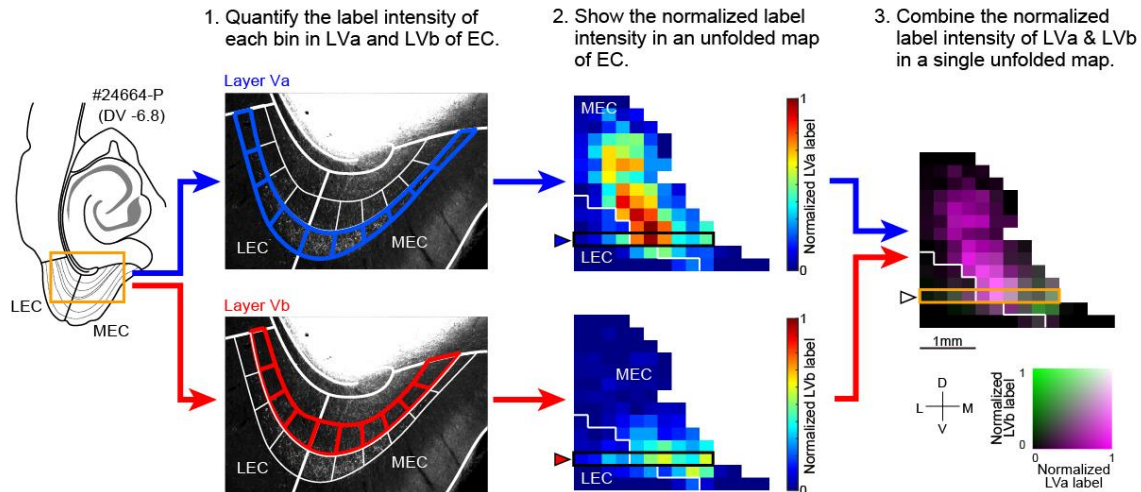


Figure 7. Schematic diagram illustrating the quantitative analysis of labeled axons in EC deep layers. Samples were analyzed in sections spaced 240 μm apart in either coronal, sagittal, or horizontal planes. Layers Va, Vb and VI were divided into columnar bins (shown for layers Va and Vb) and the label intensity in each bin was quantified (step 1). The intensity of each bin was then normalized for every sample. For layers Va and Vb, the normalized intensities were further mapped onto an unfolded map of EC (step 2) and the two maps were ultimately combined into a single unfolded map (step 3). Green indicates bins with axonal labeling in LVb and magenta bins with axonal labeling in LVa. Bins with labeling in both layers Va and Vb are shown in white and bins with no labeled axons are shown in black. The figure was created by Dr. Shinya Ohara and was adapted from Ohara et al., 2023.

Quantitative anatomical data are shown as mean \pm standard error of the mean (SEM). To compare the differences in hippocampal projection patterns between MEC layers Va, Vb and VI, normalized fluorescence intensities of bins within each layer were summed and the proportion of labeled fibers in each layer relative to all labeled fibers calculated. Differences in fluorescence intensity between layers Va and Vb were tested using paired two-tailed t-tests and differences between layers Va, Vb and VI were analyzed using one-way ANOVA followed by Bonferroni's multiple comparison test. A p value <0.05 was regarded as significant and thresholds for significance were placed identically to electrophysiological data. This entire section was originally published in Ohara et al., 2023 or will be published in Rannap et al. (in revision) and has been adopted with minor modifications.

3 RESULTS

3.1 Organization of hippocampal projections to MEC layer V

3.1.1 Distribution of dorsal hippocampal projections in MEC layer V

To understand how the innervation of MEC LV by hippocampal output projections differs along the dorsoventral axis, we conducted a series of anatomical tracing experiments. Anterograde tracers PHA-L and BDA or alternatively an AAV expressing presynapse-targeting synaptophysin-GFP were injected into hippocampal output structures CA1 and Sub at different dorsoventral and proximodistal levels in both rats and mice. Following an incubation period, brains of the injected animals were sectioned and tracers in the sections visualized. The distribution of labeled axonal fibers in MEC layers Va and Vb was then quantified along the entire dorsoventral MEC axis in different anatomical planes and normalized label intensities for both sublayers were transferred onto an unfolded map of EC (see Section 2.2.4 for details). Hippocampal-medial entorhinal projections were first examined following tracer injections into the dorsal HF. In the rat horizontal plane, strong axonal labeling in MEC LV was seen following injections into dorsal proximal CA1 and dorsal distal Sub (Figures 8A-8C and A1). Labeling intensity in MEC decreased when the injection was located closer to the CA1/Sub border (Figure A1), consistent with a topographical gradient along the proximodistal axis reported in previous studies (Naber et al., 2001; van Strien et al., 2009). For all injections, the distribution of fibers in LV was almost entirely confined to the dorsal half of MEC with labeling intensity gradually weakening and eventually disappearing when transitioning from the dorsal to the ventral MEC half (Figures 8B-8D and A1C). Consistently with previous reports (Rozov et al., 2020; Sürmeli et al., 2015; Wozny et al., 2018), dorsal hippocampal fibers originating in proximal CA1 and distal Sub distributed preferentially in LVb (Figures 8B-8D and A1C). However, in contrast to the study by Sürmeli et al., 2015, weak axonal labeling was regularly also seen in LVa (Figures 8B-8D). This labeling constituted roughly 20% of the total label intensity in MEC LV (Figure 8E), confirming the distribution of dorsal hippocampal axonal fibers in dorsal LVa.

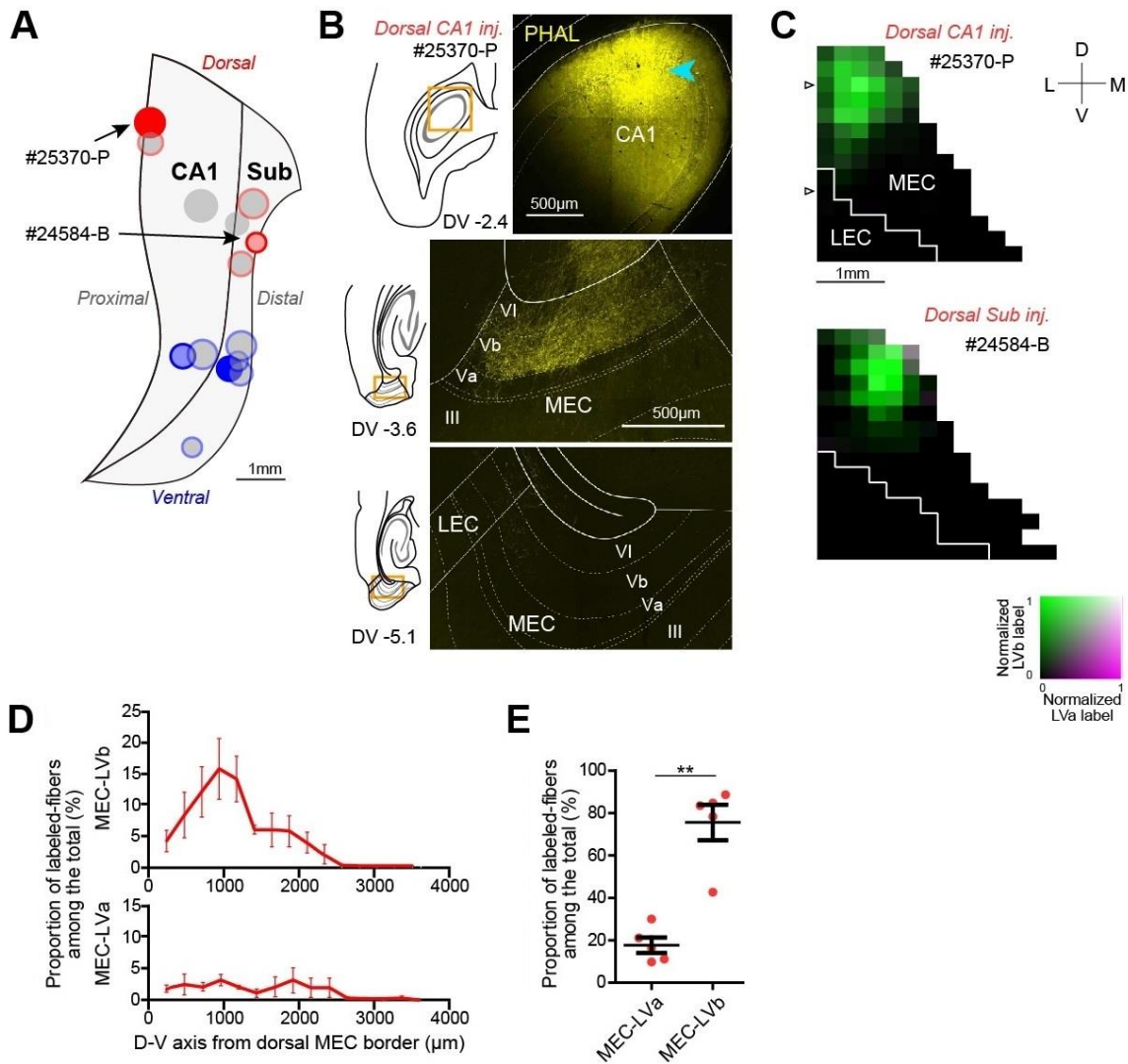


Figure 8. Projections from the dorsal HF preferentially target LVb in the dorsal MEC in rats.

(A) Two-dimensional unfolded map of CA1 and Sub showing the positions of anterograde tracer (PHA-L or BDA) injection sites for rat samples in the horizontal plane. Injection sites in the dorsal HF are shown in red. (B) Representative sample with an injection in dorsal CA1 (case 25370-P), showing the injection site (top, cyan arrowhead) and the distribution of anterogradely labeled axons in MEC at different dorsoventral (DV) levels (middle, bottom). (C) Representative two-dimensional density maps showing the patterns of anterogradely labeled axons in MEC following anterograde tracer injections into dorsal proximal CA1 or distal subiculum. Arrowheads in 25370-P show the positions of images shown in B. (D) Proportion of labeled fibers in layers Va and Vb along the dorsoventral MEC axis as a percentage of total label intensity in MEC LV for samples injected into the dorsal HF (five rats). (E) Proportion of labeled fibers in MEC layers Va and Vb as a percentage of total label intensity in EC LV for samples injected into the dorsal HF (five rats; $t_4 = 4.90$, $p = 0.008$, two-tailed paired t-test). Data are presented as mean \pm SEM. Experiments performed by Dr. Shinya Ohara; the figure was modified from Ohara et al., 2023.

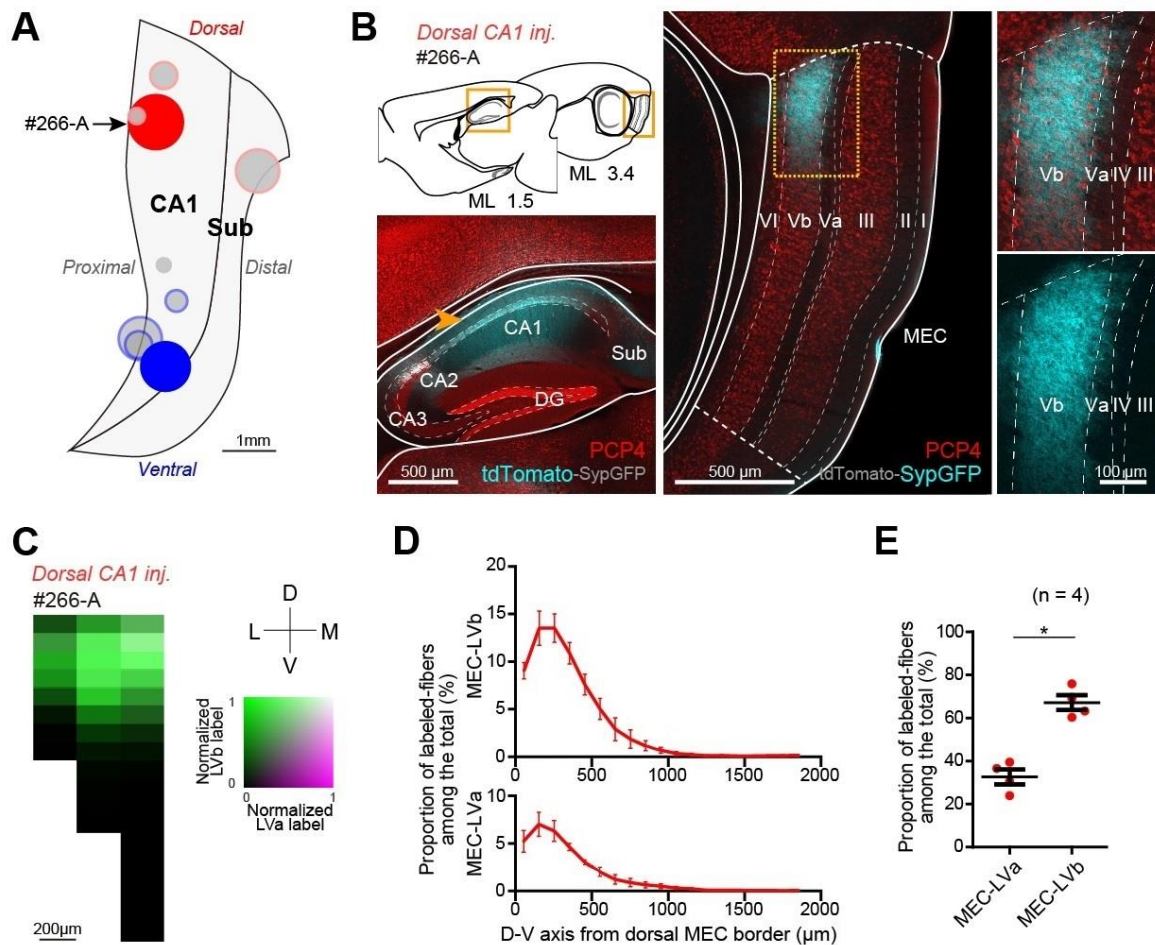


Figure 9. Projections from the dorsal HF preferentially target LVb in the dorsal MEC in mice.

(A) Two-dimensional unfolded map of CA1 and Sub showing the positions of anterograde tracer (PHA-L, BDA or AAV1-Syn1(S)-FLEX-tdTomato-T2A-SypGFP) injection sites for mouse samples in the sagittal plane. Injection sites in the dorsal HF are shown in red. (B) Representative sample with AAV injection in dorsal CA1 (case 266-A), showing the injection site (left, orange arrowhead) and the distribution of synaptophysin-GFP (SypGFP)-labeled axons in MEC (right). Samples are immunolabeled for PCP4 to identify the PCP4-positive layers III and Vb. (C) A two-dimensional density map showing the patterns of anterogradely labeled axons in MEC for the sample shown in B. (D) Proportion of labeled fibers in MEC layers Va and Vb along the dorsoventral MEC axis as a percentage of total label intensity in MEC LV for samples injected into the dorsal HF (four mice). (E) Proportion of labeled fibers in layers Va and Vb as a percentage of total label intensity in MEC LV for samples injected into the dorsal HF (four mice; $t_3 = 5.03$, $p = 0.015$, two-tailed paired t-test). Experiments performed by Dr. Shinya Ohara; the figure was modified from Ohara et al., 2023.

To determine whether an analogous connectivity scheme is also present in mice, the anterograde tracers or the AAV expressing synaptophysin-GFP were injected into mouse dorsal hippocampal area CA1 or Sub (Figures 9A, 9B, A2A and A2B). Labeling patterns

were then analyzed in the sagittal plane. Consistently with data from rats, dorsal hippocampal injections in mice resulted in axonal labeling in dorsal MEC LV, where labeled fibers preferentially distributed in LVb (Figures 9B-9D and A2C). Weaker axonal labeling, however, was regularly also observed in LVa (Figures 9B-9D and A2C). Quantification of the total label intensity in each layer revealed that the fraction of fibers in LVa in mouse sagittal slices was even higher than in rat horizontal slices, amounting to approximately one third of the total label intensity (Figure 9E). The general organization of dorsal hippocampal projections to MEC LV in the mouse was thus comparable to the projection patterns observed in rat samples.

3.1.2 Functional connectivity between the dorsal HF and MEC layer V

Although the presence of dorsal hippocampal axons in MEC LV is a strong indication of functional innervation, axonal fibers regularly pass through brain regions without forming synapses or form morphological synapses that are not functional. Furthermore, traditional anatomical tracings do not inform about the nature of postsynaptic cells. To test whether the dorsal hippocampal projections identified in anatomical tracing experiments form functional synapses with LV principal cells, I used an optogenetic approach where I expressed hChR2 in CA1 principal cells in mice. The channelrhodopsin protein was delivered to area CA1 using an AAV vector expressing hChR2 conjugated to EYFP (hChR2-EYFP) under the CaMKIIa promoter (Figures 10A and 10B). This allowed hChR2-EYFP to be specifically expressed in CA1 principal cells as in the rodent hippocampus CaMKIIa is exclusively expressed in glutamatergic neurons (Benson et al., 1992). Following a two week incubation period, I prepared brain sections from the virus-injected mice and in these sections recorded light-evoked EPSCs from both LVa and LVb principal neurons. Recordings were made at four different levels along the dorsoventral MEC axis (Figure 10C), allowing functional innervation patterns to be characterized throughout the dorsoventral extent of MEC.

Dorsal CA1 injections resulted in strong fluorescent labeling in the dorsal half of MEC (Figure 10D). Consistently with the tracing experiments, labeled axons distributed extensively in LVb, with a small fraction of fibers also extending to LVa (Figure 10D). Across all injections, I was unable to detect fluorescent fibers in the ventral half of MEC (Figure 10D). Based on the difference in labeling between the dorsal and ventral MEC, in the initial analysis I combined the two ventral section levels (1 and 2) and the two dorsal levels (3 and 4) together into a ventral and a dorsal group, respectively.

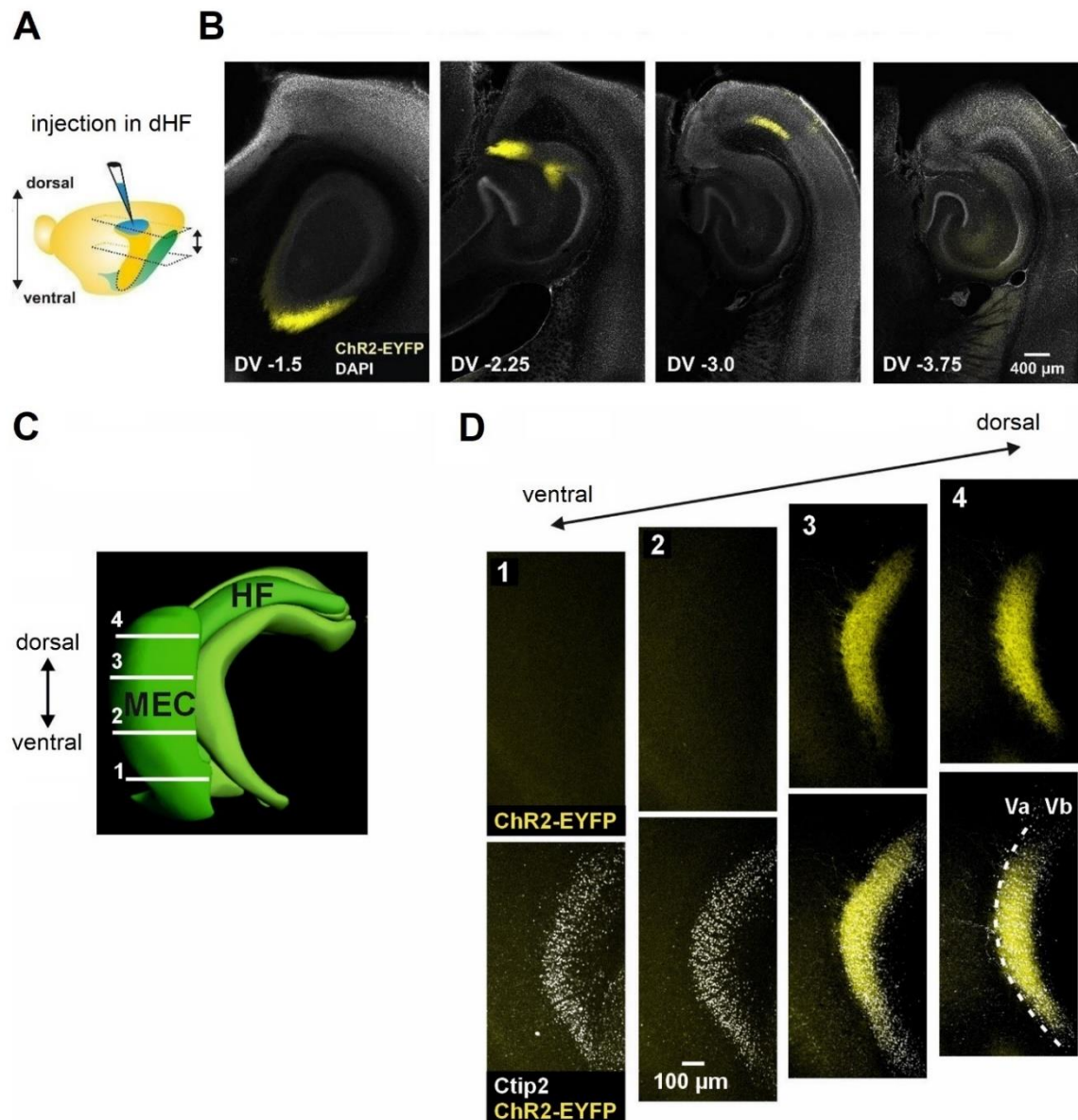


Figure 10. Representative AAV-CaMKIIa-hChR2-EYFP injection site in the dorsal HF and the distribution of labeled fibers along the dorsoventral MEC axis. (A) Illustration of the injection site (blue) in the dorsal HF (dHF). The approximate range of horizontal sections shown in B is indicated by arrows. (B) Low magnification confocal images of horizontal sections taken at different dorsoventral levels showing the injection site in dorsal CA1. (C) 3D model of the mouse HF and the adjacent MEC. The approximate location and order of horizontal sections used in experiments is indicated with numbered horizontal lines. Modified from Allen Brain Explorer (<http://connectivity.brain-map.org/3d-viewer>). (D) Confocal images of a fluorescent staining of hippocampal axons expressing hChR2-EYFP at different levels of MEC. The bottom panels show images from the top overlaid with Ctip2 labeling. Horizontal sections along the dorsoventral axis are indicated as shown in C. Modified from Ohara et al., 2023.

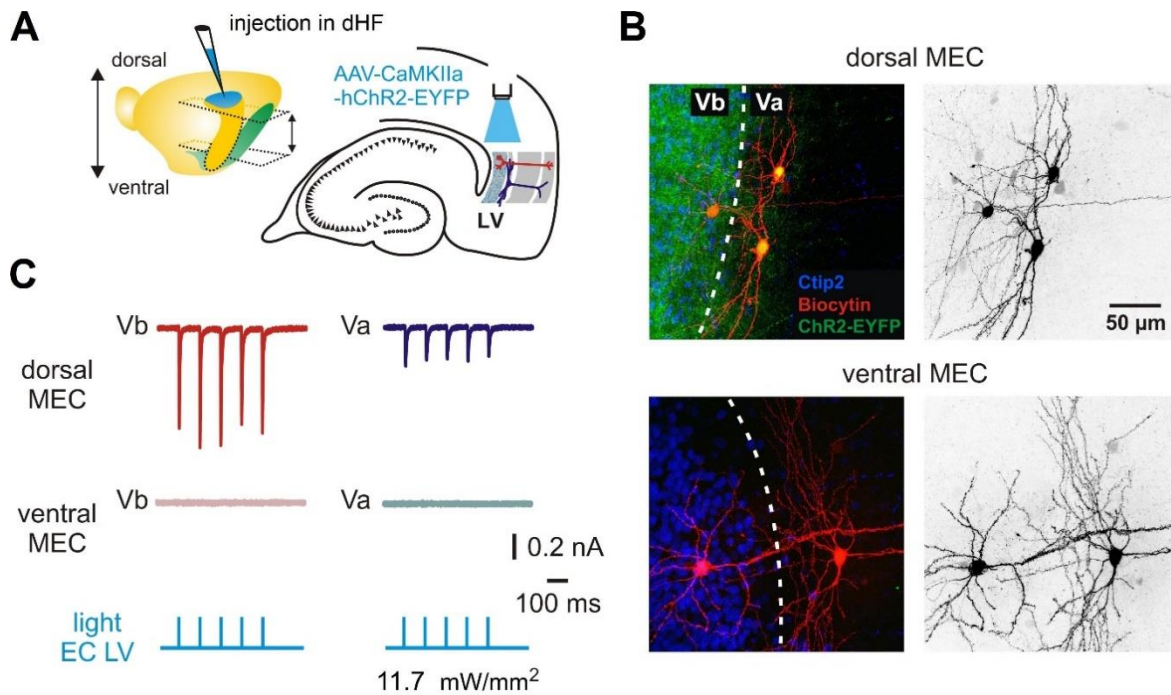


Figure 11. Functional connectivity between the dorsal HF and MEC LVA and LVb principal neurons. (A) Left: illustration of the injection site (blue) in the dorsal HF (dHF) with the approximate range of horizontal sections used in experiments indicated by arrows. Right: schematic drawing of a horizontal hippocampal-MEC slice showing the position of light stimulation used to activate the axons of dorsal hippocampal neurons infected with AAV-CaMKIIa-hChR2-EYFP. (B) Maximum intensity projection confocal images of representative horizontal slices from the dorsal (top) and ventral MEC (bottom), showing recorded LVA and LVb principal neurons labeled with biocytin, overlaid with Ctip2 labeling and fluorescent staining of hippocampal axons expressing hChR2-EYFP. Note the weak but recognizable fluorescence in Ctip2-negative LVA in the dorsal MEC (top). Right images show the same neurons in black and white contrast. (C) Example EPSC traces recorded from LVA and LVb neurons in the same slice in the dorsal (top) and ventral MEC (middle) in response to 1 ms blue light pulses (bottom). Modified from Ohara et al., 2023.

I first recorded light-evoked postsynaptic responses from 10 LVA and 9 LVb principal neurons at the two ventral section levels (Figures 11A and 11B). As predicted by the lack of fluorescence, all recorded cells failed to respond to light stimulation (Figures 11C and 12B), confirming the absence of functional projections from the dorsal HF to ventral MEC LV. I then recorded responses from 22 LVb and 34 LVA principal neurons at the two dorsal section levels (Figures 11A and 11B). All LVb and 26/34 LVA neurons exhibited EPSCs with short latencies (median: LVb: 2.09 ms, $n = 22$; LVA: 1.96 ms, $n = 26$, $p = 0.788$, Mann-Whitney U test) and comparably fast 20%-80% EPSC rise times (median: LVb: 0.85 ms, $n = 22$; LVA: 0.79 ms, $n = 26$; $p = 0.482$, Mann-Whitney U test), suggesting monosynaptic input from the

dorsal hippocampus. Four LVa cells failed to respond to light stimulation and the remaining four cells responded with latencies above 3.5 ms (median 4.99 ms), indicating polysynaptic input to these cells. In line with the stronger labeling intensity seen in LVb, EPSC amplitudes in LVb neurons were almost threefold higher across most light intensities, compared to monosynaptically innervated LVa neurons (11.7 mW/mm², median: LVb: -0.55 nA; LVa: -0.20 nA; Figures 11C and 12A, left panel). Because absolute hChR2 expression levels can vary widely between injections, I compared LVa and LVb responses after normalizing EPSC amplitudes recorded from neurons in both layers to the highest LVb current amplitude at maximum light intensity in each slice. EPSC amplitudes in LVb neurons following normalization were still roughly twofold higher across most light intensities than responses recorded from LVa neurons (11.7 mW/mm², median: LVb: 1.00; LVa: 0.48; Figure 12A, right panel).

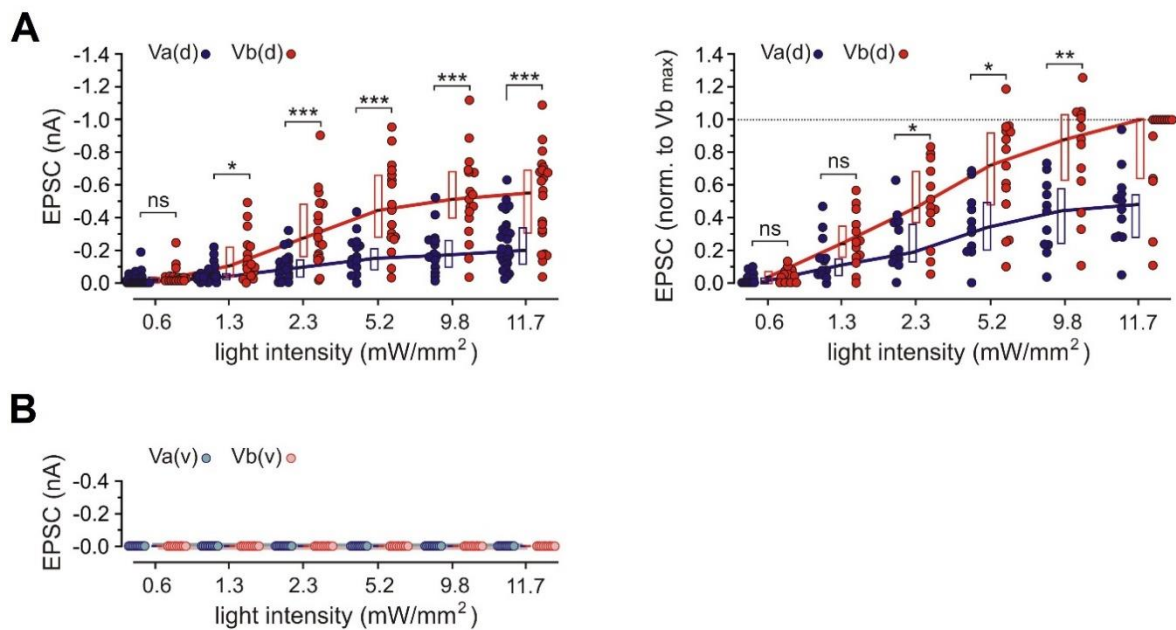


Figure 12. Quantification of dorsal hippocampal responses measured from LVa and LVb principal neurons in the dorsal and ventral MEC. (A) Quantification of synaptic responses from LVa [Va(d)] and LVb neurons [Vb(d)] recorded in the dorsal MEC. Left: plots of EPSC amplitudes induced by light pulses with increasing intensities (Va(d), 26 cells from 14 mice; Vb(d), 22 cells from 11 mice; 11.7 mW/mm², $p = 0.0007$, Mann-Whitney U test). Right: values from the left graph normalized to the highest LVb response at maximum light intensity (11.7 mW/mm²) in each slice (LVa(d), 12 cells from 7 mice; LVb(d), 14 cells from 7 mice). (B) Same analysis as in A for LVa [Va(v)] and LVb neurons [Vb(v)] recorded in the ventral MEC (LVa(v), 10 cells from 3 mice; LVb(v), 9 cells from 3 mice). All data are presented as median (black line), 25th and 75th percentiles (box). Circles represent individual values. Mann-Whitney U test: *** $p < 0.001$; ** $p < 0.01$; * $p < 0.05$; ns, not significant. Modified from Ohara et al., 2023.

In order to examine dorsal hippocampal innervation of dorsal LV in more detail, I analyzed the EPSC amplitudes of LVA and LVb cells at the two dorsal section levels individually. At both section levels, LVb neurons received comparably strong input (11.7 mW/mm², median: level 3: -0.47 nA; level 4: -0.56 nA; Figure 13B). In contrast, LVA responses exhibited a clear dorsoventral gradient where EPSC amplitudes at section level 3 were significantly smaller than responses at level 4 (11.7 mW/mm², median: level 3: -0.16 nA; level 4: -0.34 nA; Figure 13A). This gradient was also present relative to LVb neurons, revealed by normalizing LVA responses to the highest LVb amplitude in each slice (11.7 mW/mm², median: level 3: 0.28; level 4: 0.54; Figure A3). Overall, the electrophysiological data were consistent with results from anatomical tracing experiments, confirming that dorsal hippocampal projections are restricted to the dorsal half of MEC where they preferentially innervate LVb over LVA principal cells.

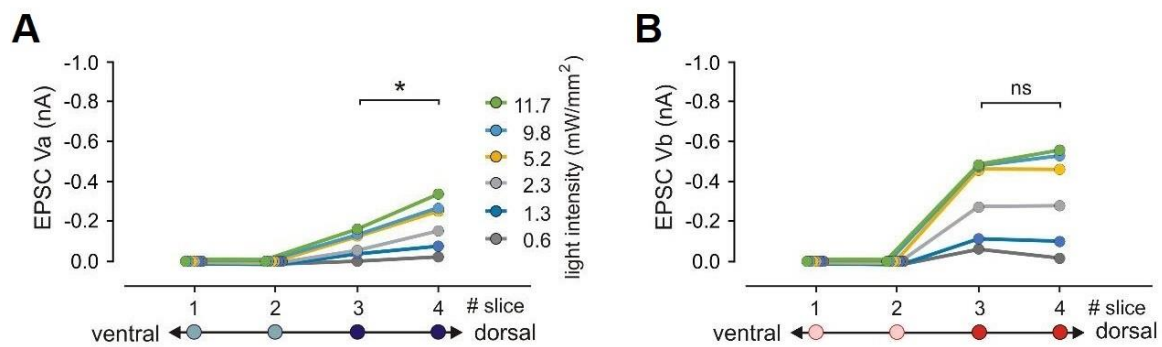
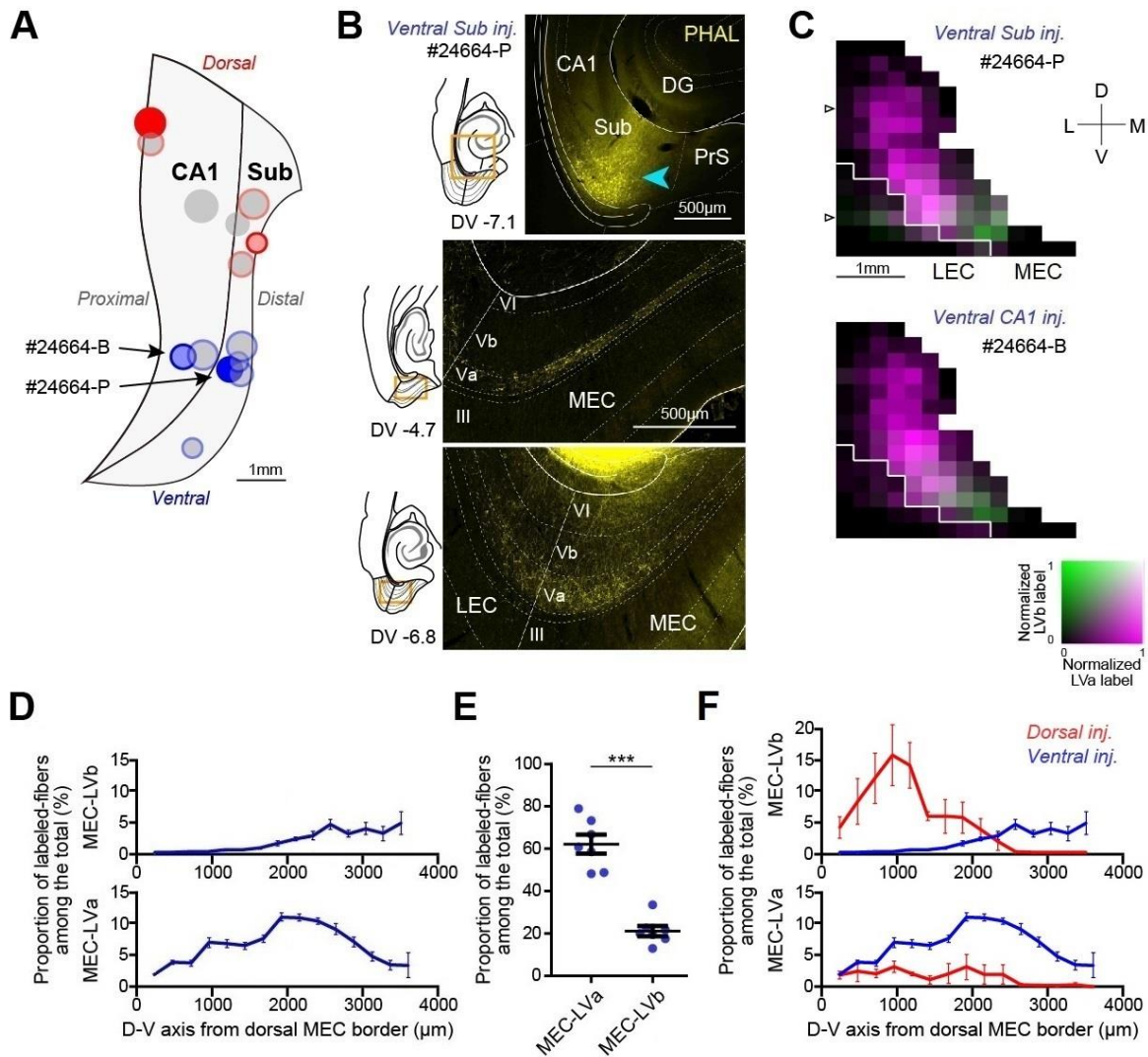


Figure 13. Quantification of dorsal hippocampal responses measured from LVA and LVb principal neurons along the dorsoventral MEC axis. (A) Quantification of synaptic responses recorded from LVA neurons at four different slice levels along the dorsoventral MEC axis. The panels show plots of EPSC amplitudes induced by light pulses with increasing intensities (level 3: 16 cells from 10 mice; level 4: 10 cells from 7 mice; 11.7 mW/mm², $p = 0.023$, Mann-Whitney U test). (B) Same analysis as in A for responses recorded from LVb neurons (level 3: 11 cells from 5 mice; level 4: 11 cells from 8 mice; 11.7 mW/mm², $p = 0.869$, Mann-Whitney U test). Data for both panels are analyzed at four different section levels along the dorsoventral MEC axis for light pulses with increasing intensities (none of the neurons in ventral slices responded). All data are presented as median. Mann-Whitney U test for response values at maximum light intensity: * $p < 0.05$; ns, not significant. Modified from Ohara et al., 2023.

3.1.3 Distribution of ventral hippocampal projections in MEC layer V

Anterograde tracers PHA-L and BDA were next injected into area CA1 and Sub in the ventral HF. The brains of injected animals were then sectioned, the tracers visualized and the distribution of labeled axonal fibers in layers Va and Vb along the dorsoventral MEC axis quantified as before. Similarly to injections into the dorsal HF, hippocampal-medial entorhinal projections were first examined in the rat horizontal plane. Consistently with the proximodistal gradient seen for dorsal hippocampal injections, anterograde tracer injections into ventral proximal CA1 and ventral distal Sub resulted in strong axonal labeling in MEC LV (Figures 14A-14C and A4). However, the sublayer specificity of ventral hippocampal fibers was different from dorsal hippocampal projections as ventral fibers distributed extensively in LVa (Figures 14B-14D, 14F and A4C). In the ventral half of MEC, prominent axonal labeling was present in both layers Va and Vb (Figures 14B-14D and A4C). At more dorsal levels, labeling between the sublayers diverged: while axonal fibers in LVb disappeared when transitioning from the ventral to the dorsal MEC, fibers in LVa extended throughout the dorsal half of MEC (Figures 14B-14D and A4C). The widespread distribution of ventral hippocampal output projections across the entire dorsoventral MEC axis thus uniquely contrasted with both the ventral hippocampal projection to LVb as well as dorsal hippocampal projections to both layers Vb and Va, which were all confined to their respective MEC halves. Consistently with the extensive axonal distribution, the total label intensity of ventral hippocampal fibers in LVa was found to be significantly higher than in LVb (Figure 14E).

Ventral hippocampal projections were then examined in the mouse sagittal plane. In agreement with rat data, the injection of anterograde tracers or the AAV expressing synaptophysin-GFP into mouse ventral hippocampal area CA1 or Sub resulted in extensive labeling in LVa throughout the dorsoventral MEC axis (Figures 15 and A2). Indeed, synaptophysin-GFP labeling was observed in the dorsalmost portion of LVa (Figures 15B and 15D), indicating that ventral hippocampal projections target LVa neurons along the entire dorsoventral extent of MEC. In contrast, prominent labeling in LVb was only seen in the ventral MEC (Figures 15B-15D and A2), consistent with the projection patterns observed in rat samples.



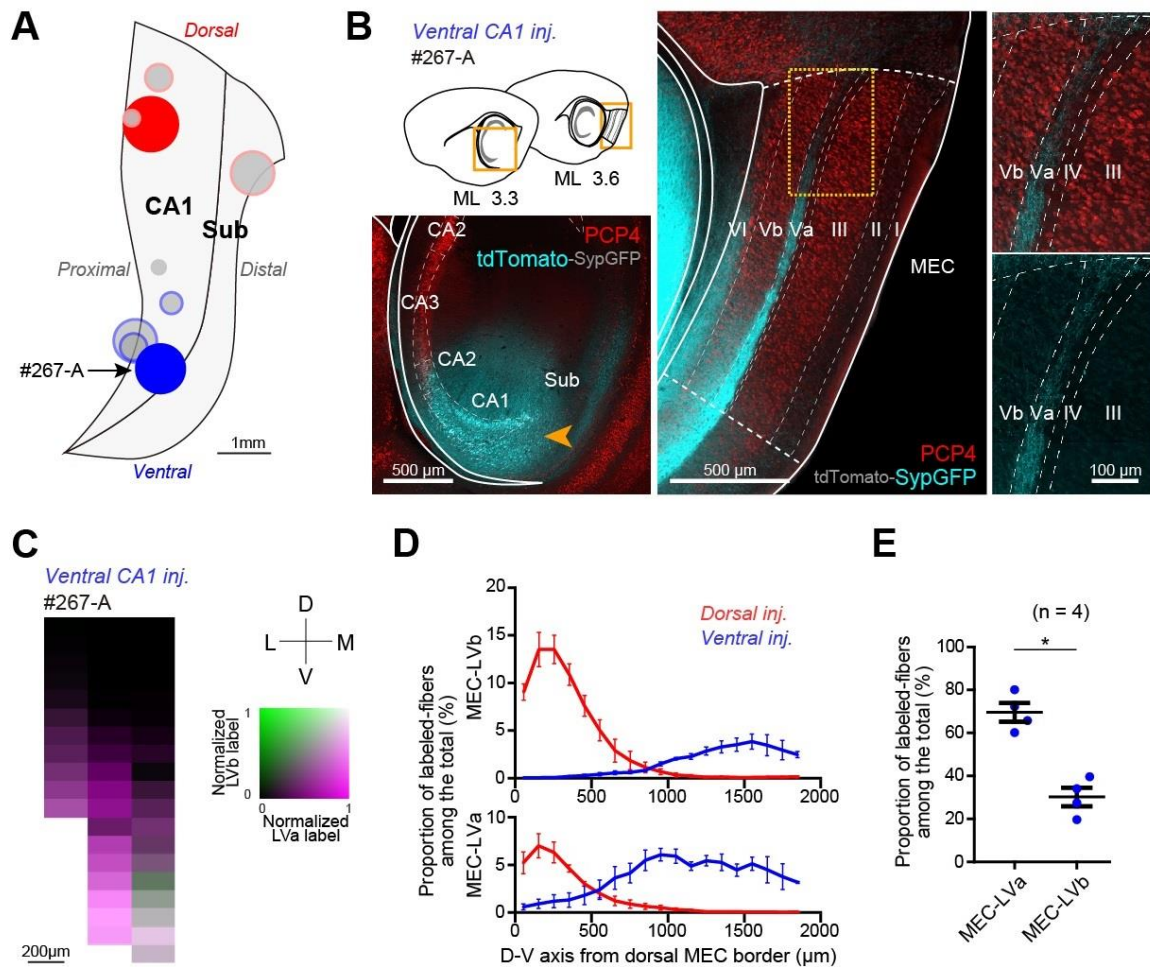


Figure 15. Projections from the ventral HF target LVa throughout the dorsoventral MEC axis in mice. (A) Two-dimensional unfolded map of CA1 and Sub showing the positions of anterograde tracer (PHA-L, BDA or AAV1-Syn1(S)-FLEX-tdTomato-T2A-SypGFP) injection sites for mouse samples in the sagittal plane. Injection sites in the ventral HF are shown in blue. (B) Representative sample with AAV injection in ventral CA1 (case 267-A), showing the injection site (left, orange arrowhead) and the distribution of synaptophysin-GFP (SypGFP)-labeled axons in MEC (right). Samples are immunolabeled for PCP4 to identify the PCP4-positive layers III and Vb. (C) A two-dimensional density map showing the patterns of anterogradely labeled axons in MEC for the sample shown in B. (D) Proportion of labeled fibers in layers Va and Vb along the dorsoventral MEC axis as a percentage of total label intensity in MEC LV for samples injected into the ventral HF (blue, four mice). Data for ventral injections are overlaid with data for dorsal hippocampal injections (red) from Figure 9D. (E) Proportion of labeled fibers in MEC layers Va and Vb as a percentage of total label intensity in MEC LV for samples injected into the ventral HF (four mice; $t_3 = 4.56$, $p = 0.020$, two-tailed paired t-test). Data are presented as mean \pm SEM. Experiments performed by Dr. Shinya Ohara; the figure was modified from Ohara et al., 2023.

3.1.4 Functional connectivity between the ventral HF and MEC layer V

To functionally test the innervation of LV principal neurons by ventral hippocampal projections, I injected the AAV vector expressing hChR2-EYFP into ventral hippocampal area CA1 (Figures 16A and 16B). I consistently observed widespread axonal labeling in LVa that extended throughout all four dorsoventral section levels (Figures 16C and 16D). In contrast, while labeled fibers in LVb were clearly present at the two ventral section levels, labeling in the two dorsal sections was markedly weaker to minimal (Figure 16D).

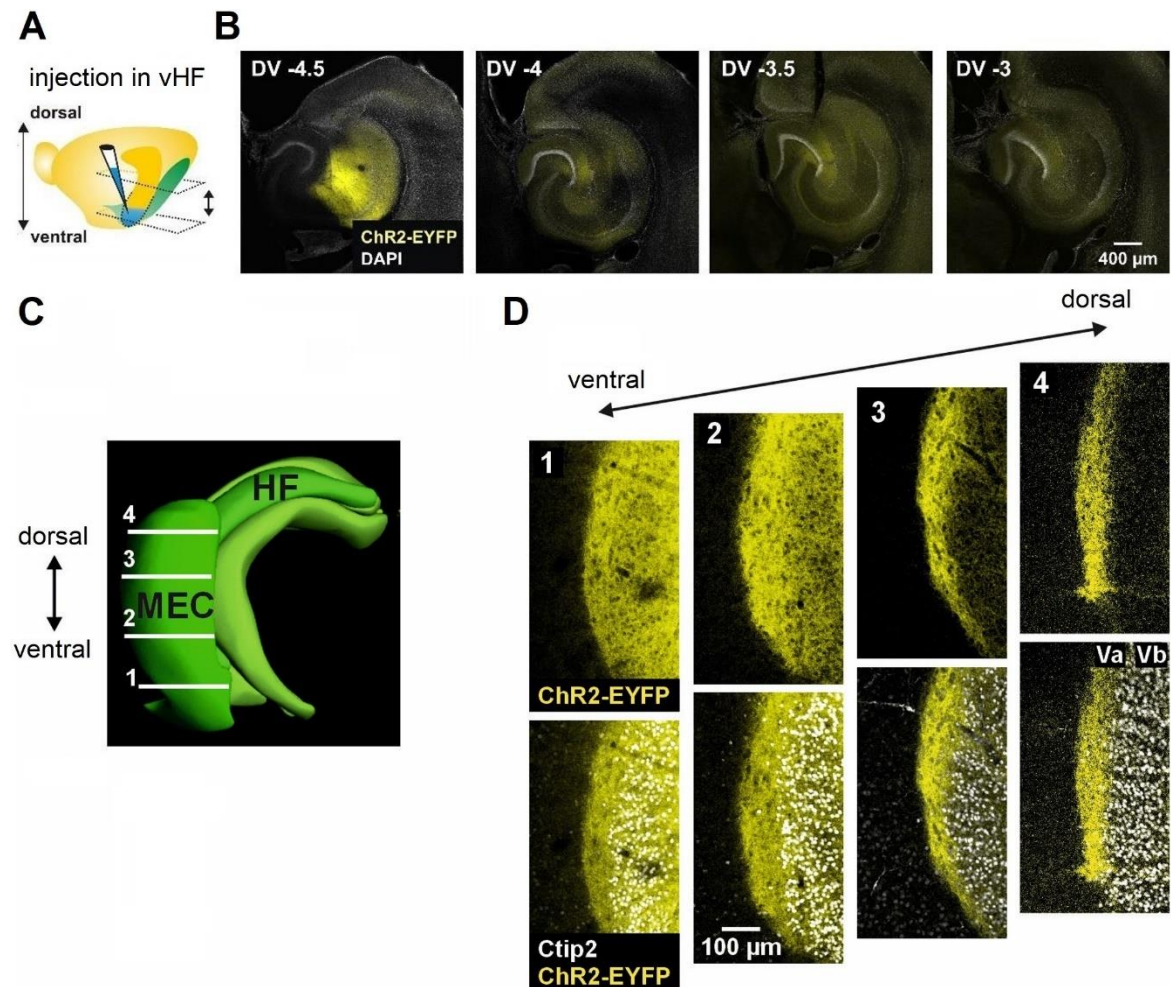


Figure 16. Representative AAV-CaMKIIa-hChR2-EYFP injection site in the ventral HF and the distribution of labeled fibers along the dorsoventral MEC axis. (A) Illustration of the injection site (blue) in the ventral HF (vHF). (B) Low magnification confocal images of horizontal sections taken at different dorsoventral levels showing the injection site in ventral CA1. (C) 3D model of the mouse HF and the adjacent MEC. The approximate location and order of horizontal sections used in experiments is indicated with numbered horizontal lines. Modified from Allen Brain Explorer (<http://connectivity.brain-map.org/3d-viewer>). (D) Confocal images of a fluorescent staining of hippocampal axons expressing hChR2-EYFP at different levels of MEC. The bottom panels show images from the top overlaid with Ctip2 labeling. Modified from Ohara et al., 2023.

I subsequently recorded light-evoked EPSCs from both LVa and LVb principal neurons at all four section levels along the dorsoventral MEC axis. Similarly to dorsal hippocampal injections, in the initial analysis I grouped the two ventral and the two dorsal section levels together into a ventral and a dorsal group, respectively. I first recorded responses from 11 LVa and 20 LVb principal neurons at the two ventral section levels (Figures 17A and 17B). All recorded LVa and LVb cells showed EPSCs with short latencies (median: LVa: 2.27 ms, $n = 11$; LVb: 2.29 ms, $n = 20$; $p = 0.934$, Mann-Whitney U test) and comparably fast 20%-80% EPSC rise times (median: LVa: 1.07 ms, $n = 11$; LVb: 1.02 ms, $n = 20$; $p = 0.664$, Mann-Whitney U test), consistent with monosynaptic innervation by the ventral hippocampus.

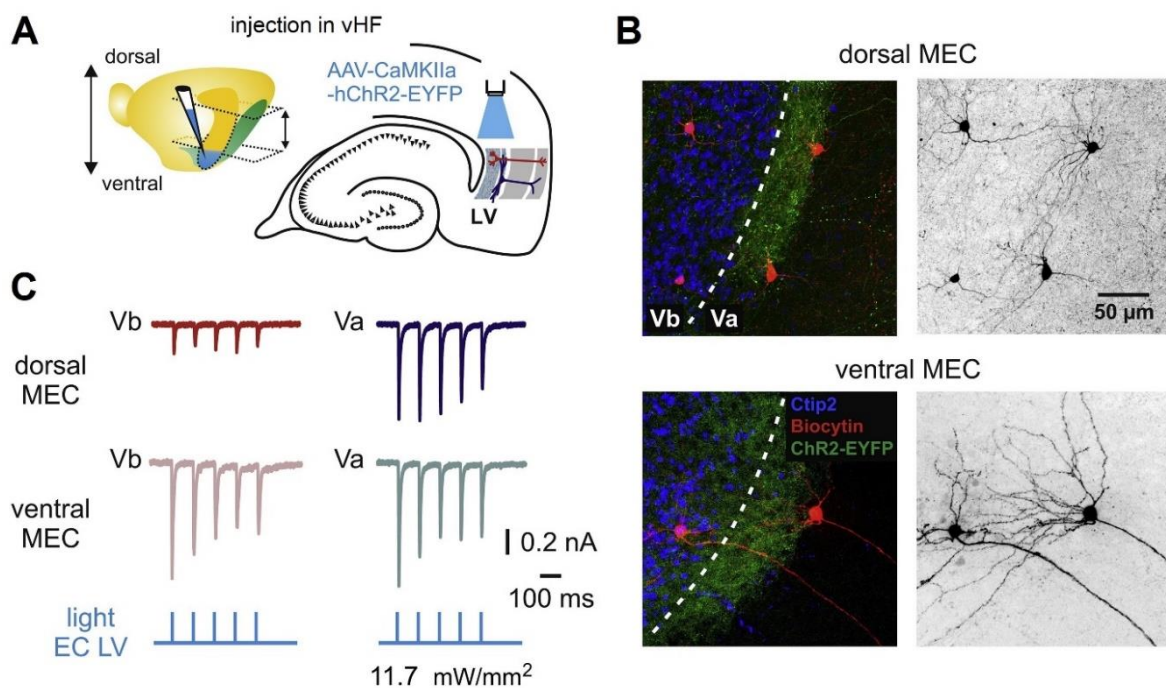


Figure 17. Functional connectivity between the ventral HF and MEC LVa and LVb principal neurons. (A) Left: illustration of the injection site (blue) in the ventral HF (vHF) with the approximate range of horizontal sections used in experiments indicated by arrows. Right: schematic drawing of a horizontal hippocampal-MEC slice showing the position of light stimulation used to activate the axons of ventral hippocampal neurons infected with AAV-CaMKIIa-hChR2-EYFP. (B) Maximum intensity projection confocal images of representative horizontal slices from the dorsal (top) and ventral MEC (bottom), showing recorded LVa and LVb principal neurons labeled with biocytin, overlaid with Ctip2 labeling and fluorescent staining of hippocampal axons expressing hChR2-EYFP. Note the strong fluorescence of axonal fibers around Ctip2-negative LVa neurons in the dorsal MEC (top). Right images show the same neurons in black and white contrast. (C) Example EPSC traces recorded from LVa and LVb neurons in the same slice in the dorsal (top) and ventral (middle) MEC in response to 1 ms blue light pulses (bottom). Modified from Ohara et al., 2023.

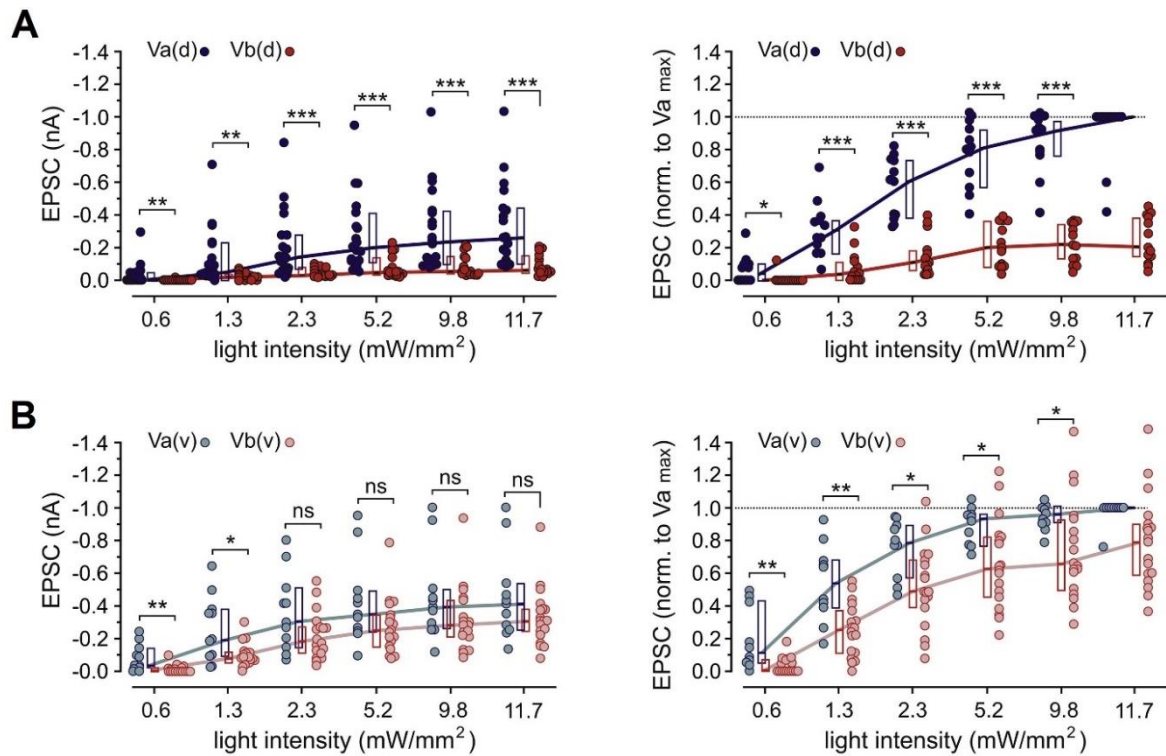


Figure 18. Quantification of ventral hippocampal responses measured from LVa and LVb principal neurons in the dorsal and ventral MEC. (A) Quantification of synaptic responses from LVa [LVa(d)] and LVb neurons [LVb(d)] recorded in the dorsal MEC. Left: plots of EPSC amplitudes induced by light pulses with increasing intensities (LVa(d), 19 cells from 14 mice; LVb(d), 16 cells from 11 mice; 11.7 mW/mm², $p = 0.0001$, Mann-Whitney U test). Right: values from the left graph normalized to the highest LVa response at maximum light intensity (11.7 mW/mm²) in each slice (LVa(d), 12 cells from 9 mice; LVb(d), 13 cells from 9 mice). (B) Quantification of LVa [LVa(v)] and LVb responses [LVb(v)] recorded in the ventral MEC. Left: plots of EPSC amplitudes induced by light pulses with increasing intensities (LVa(v), 11 cells from 8 mice; LVb(v), 20 cells from 8 mice; 11.7 mW/mm², $p = 0.223$, Mann-Whitney U test). Right: values from the left graph normalized to the highest LVa response at maximum light intensity (11.7 mW/mm²) in each slice (LVa(v), 10 cells from 7 mice; LVb(v), 19 cells from 7 mice). All data are presented as median (black line), 25th and 75th percentiles (box). Circles represent individual values. Mann-Whitney U test: *** $p < 0.001$; ** $p < 0.01$; * $p < 0.05$; ns, not significant. Modified from Ohara et al., 2023.

Ventral EPSC amplitudes tended to be higher in LVa than LVb neurons (11.7 mW/mm², median: LVa: -0.41 nA; LVb: -0.31 nA; Figures 17C and 18B, left panel) but this difference did not reach significance. To account for differences in fluorescence intensity between injections, I normalized both LVa and LVb responses to the highest LVa current amplitude at maximum light intensity in each slice. Although the relative difference between LVa and LVb current amplitudes changed only marginally with normalization (11.7 mW/mm²,

median: LVa: 1.00; LVb: 0.79; Figure 18B, right panel), in this case the difference was found to be significant across the stimulation intensities. I next recorded light-evoked responses from 19 LVa and LVb principal neurons at the two dorsal section levels (Figures 17A and 17B). All 19 LVa and 16/19 LVb neurons exhibited short latency EPSCs (LVa: 2.31 ms, n = 19; LVb: 2.45 ms, n = 16; p = 0.179, Mann-Whitney U test) with comparably fast 20%-80% EPSC rise times (LVa: 1.16 ms, n = 19; LVb: 0.91 ms, n = 16; p = 0.09, Mann-Whitney U test), suggesting monosynaptic input from the ventral hippocampus. One LVb cell failed to respond and the remaining two cells responded with latencies above 3.5 ms (median 5.13 ms), indicating polysynaptic input. Importantly, EPSC amplitudes recorded from dorsal LVa neurons were over fourfold higher than LVb amplitudes (11.7 mW/mm², median: LVa: -0.26 nA; LVb: -0.06 nA; Figures 17C and 18A, left panel) and this difference was even greater when the responses were normalized to the highest LVa amplitude in each slice, reaching a fivefold difference (11.7 mW/mm², median: LVa: 1.00; LVb: 0.20; Figure 18A, right panel).

To explore the innervation of LV principal cells by ventral hippocampal outputs along the dorsoventral MEC axis in detail, I examined the EPSC amplitudes of LVa and LVb neurons at all four section levels individually. I first analyzed responses recorded from LVa neurons, finding a slight non-significant trend towards smaller amplitudes at more dorsal section levels (11.7 mW/mm², median: level 1: -0.41 nA; level 2: -0.38 nA; level 3: -0.22 nA; level 4: -0.26 nA; Figure 19A). In contrast, while at the two ventral section levels LVb EPSC amplitudes were also relatively large, the amplitudes decreased over fivefold when transitioning from ventral to dorsal sections (11.7 mW/mm², median: level 1: -0.31 nA; level 2: -0.31 nA; level 3: -0.06 nA; level 4: -0.05 nA; Figure 19B). I then compared LVa and LVb amplitudes to each other, finding them to be comparable at the two ventral but to significantly differ at the two dorsal section levels (Figure 19C). Furthermore, LVa and LVb responses were different when compared across all section levels (Figure 19C). Finally, I examined LVb responses after normalizing LVb amplitudes to the highest LVa amplitude in each slice. This analysis revealed a similar overall dynamic as seen for absolute amplitudes, where responses at the two ventral and the two dorsal section levels were comparable but there was a sharp decline in amplitudes between section levels 2 and 3 (11.7 mW/mm², median: level 1: 0.87; level 2: 0.66; level 3: 0.23; level 4: 0.20; Figure 19D). Together, the electrophysiological results thus corroborated anatomical tracing data, confirming that the ventral HF forms a major source of input to LVa principal neurons along the entire dorsoventral MEC axis, whereas LVb cells are predominantly innervated in the ventral MEC.

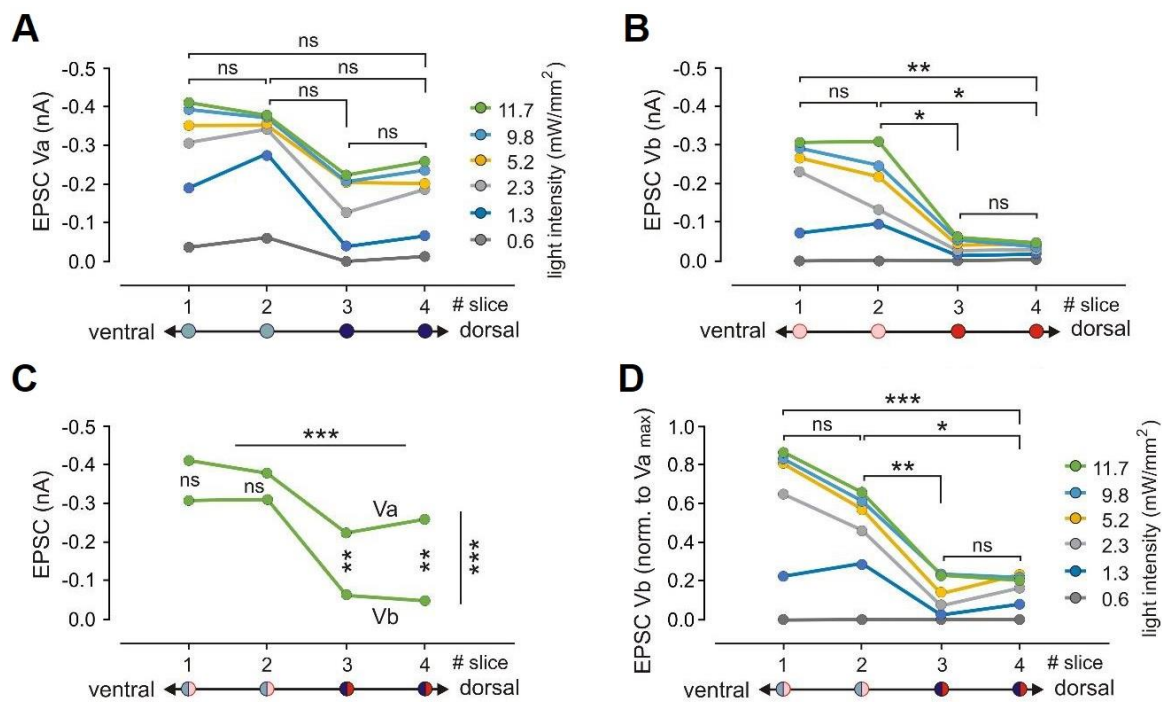


Figure 19. Quantification of ventral hippocampal responses measured from LVa and LVb principal neurons along the dorsoventral MEC axis. (A) Quantification of synaptic responses recorded from LVa neurons at four different slice levels along the dorsoventral MEC axis. The graph shows median EPSC amplitudes induced by light pulses with increasing intensities. (level 1: 5 cells from 4 mice; level 2: 6 cells from 6 mice; level 3: 12 cells from 10 mice; level 4: 7 cells from 5 mice; 11.7 mW/mm², $H = 2.23$, $p = 0.527$, $p > 0.05$ between all slice levels, Kruskal-Wallis test with Dunn's post hoc comparison). (B) Same analysis as in A for responses recorded from LVb neurons (level 1: 11 cells from 5 mice; level 2: 9 cells from 5 mice; level 3: 11 cells from 8 mice; level 4: 5 cells from 3 mice; 11.7 mW/mm², $H = 21.42$, $p < 0.001$; 1 vs. 2, $p > 0.05$; 2 vs. 3, $p < 0.05$; 2 vs. 4, $p < 0.05$; 3 vs. 4, $p > 0.05$; 1 vs. 4, $p < 0.01$, Kruskal-Wallis test with Dunn's post hoc comparison). (C) Comparison of LVa and LVb responses at maximum light intensity along the dorsoventral MEC axis, revealing that the responses are significantly different ($F_{(1,58)} = 21.04$, $p < 0.001$; Va vs. Vb for level 1, $p = 1$; for level 2, $p = 1$; for level 3, $p = 0.008$; for level 4, $p = 0.007$, two-way ANOVA followed by Bonferroni's comparison test) and also differ when compared across all section levels ($F_{(3,58)} = 10.10$, $p < 0.001$, two-way ANOVA). (D) Quantification of synaptic responses recorded from LVb neurons normalized to the highest LVa response at maximum light intensity (11.7 mW/mm²) in each slice (level 1: 10 cells from 4 mice; level 2: 9 cells from 5 mice; level 3: 8 cells from 6 mice; level 4: 5 cells from 3 mice; $F_{(3,28)} = 14.86$, $p < 0.001$; 1 vs. 2, $p = 0.852$; 2 vs. 3, $p = 0.002$; 2 vs. 4, $p = 0.011$; 3 vs. 4, $p = 1.000$; 1 vs. 4, $p < 0.001$, one-way ANOVA followed by Bonferroni's test). Data for all panels are analyzed at four different section levels along the dorsoventral MEC axis for light pulses with increasing intensities. All data are presented as median. For all statistical tests: *** $p < 0.001$; ** $p < 0.01$; * $p < 0.05$; ns, not significant. Modified from Ohara et al., 2023.

3.2 Organization of hippocampal projections to MEC layer VI

3.2.1 Distribution of hippocampal projections in MEC layer VI

Having characterized the organization of hippocampal output projections to MEC LV, we next focused on the dorsoventral topography of hippocampal projections to MEC LVI. We again started with a detailed anatomical analysis by reexamining mouse sagittal samples that had been previously injected with the anterograde tracers PHA-L and BDA or the AAV expressing synaptophysin-GFP into area CA1 or Sub in the dorsal or ventral HF (Figure A2). Injections into dorsal proximal CA1 or dorsal distal Sub resulted in axonal labeling in the dorsal half of MEC LVI (Figure 20A), mirroring the dorsal hippocampal projection to MEC LV. Subsequent quantification of label intensity in layers VI, Vb and Va revealed that labeled fibers in LVI distributed almost identically to LVa (Figure 20B, top panel). Accordingly, total label intensity was found to be comparable between layers VI and Va, whereas label intensity in LVb was significantly higher (Figure 20C, left panel).

When injections were placed in ventral proximal CA1, axonal labeling was primarily observed in the ventral half of MEC LVI (Figure 20A). The distribution of labeled fibers along the dorsoventral axis in LVI was nearly identical to LVb (Figure 20B, bottom panel), indicating that ventral hippocampal projections to LVI do not exhibit the widespread projection pattern seen for LVa. Consistently, total label intensity was significantly higher in LVa, compared to layers VI or Vb (Figure 20C, right panel). In summary, hippocampal projections to MEC LVI exhibited a parallel topographical organization where dorsal hippocampal projections target dorsal and ventral projections ventral LVI.

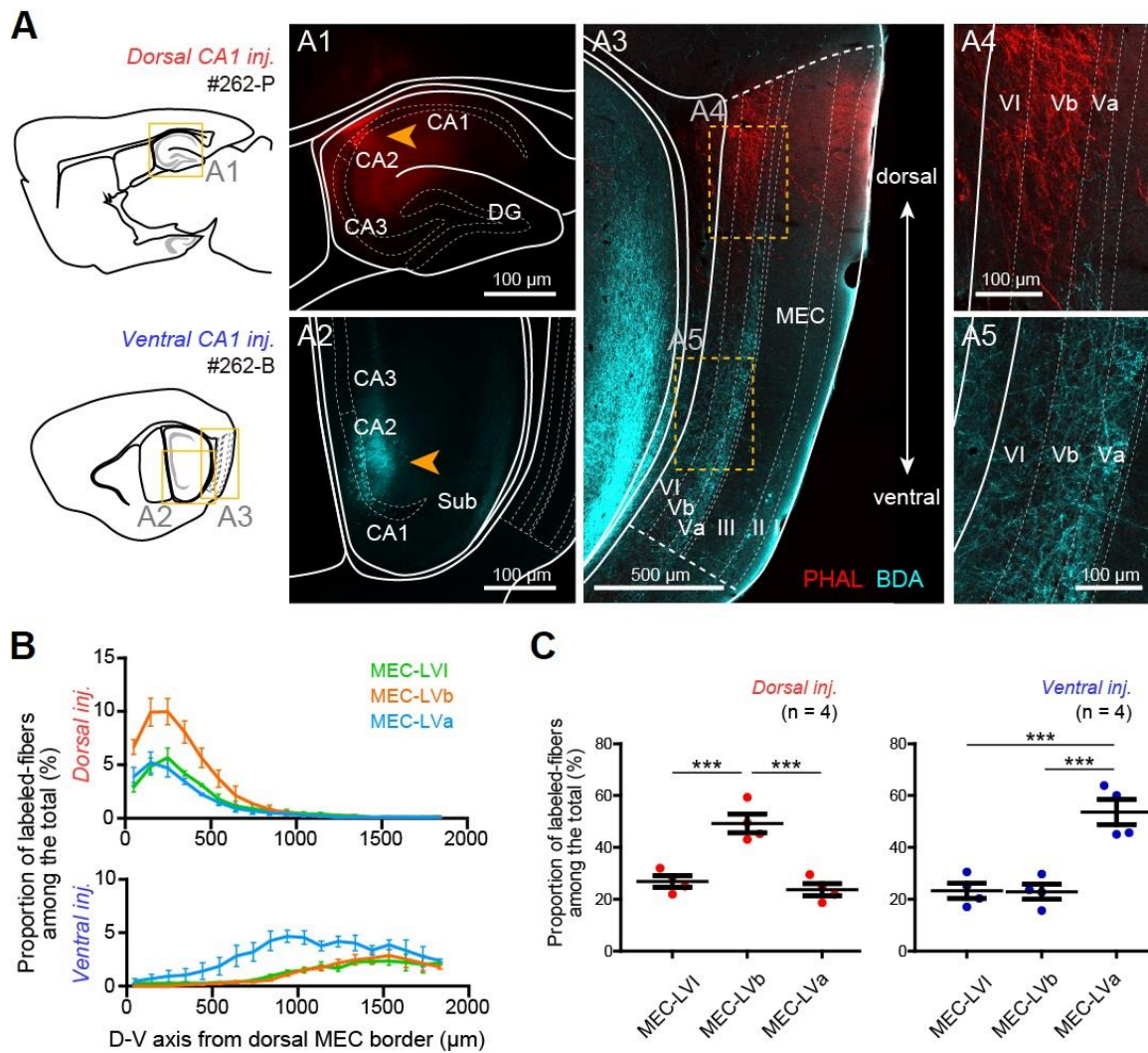


Figure 20. Dorsal and ventral hippocampal projections to MEC layer VI exhibit a parallel topographical organization. (A) Representative sample with a PHA-L injection in dorsal CA1 (case #262-P) and a BDA injection in ventral CA1 (case #262-B). The injection sites are shown in A1–A2 (orange arrowheads) and the distribution of labeled axons in MEC in A3–A5. (B) Proportion of labeled fibers in layers VI, Vb, and Va along the dorsoventral MEC axis as a percentage of total label intensity in MEC deep layers for samples injected into the dorsal (top, 4 mice) or ventral HF (bottom, 4 mice). (C) Proportion of labeled fibers in MEC layers VI, Vb, and Va as a percentage of total label intensity in MEC deep layers for samples injected into the dorsal HF (red, four mice; $F_{(2,9)} = 25.3$, $p < 0.001$; $p < 0.001$ for LVb vs. LVI and LVb vs. LVa, one-way ANOVA followed by Bonferroni’s multiple comparison test) or ventral HF (blue, four mice; $F_{(2,9)} = 23.03$, $p < 0.001$; $p < 0.001$ for LVa vs. LVI and LVa vs. LVb, one-way ANOVA followed by Bonferroni’s multiple comparison test). Data are presented as mean \pm SEM. Experiments performed by Dr. Shinya Ohara; the figure was modified from Rannap et al. (in revision).

3.2.2 Functional connectivity between the dorsal HF and MEC layer VI

To functionally assess dorsal hippocampal innervation of MEC LVI, I used the same optogenetic approach as previously. I expressed hChR2-EYFP in dorsal CA1 pyramidal neurons by injecting the respective AAV vector into dorsal hippocampal area CA1 (Figures A5A and A5B). In line with the distribution of fibers seen in tracing experiments, dorsal CA1 injections resulted in relatively weak axonal labeling in LVI that was confined to the dorsal MEC (Figures 21B and A6B). To confirm the absence of functional projections from the dorsal HF to ventral LVI, I recorded from 14 LVI principal neurons in the ventral MEC (Figures 21A and 21B), all of which failed to respond to light stimulation (Figures 21C and 22A).

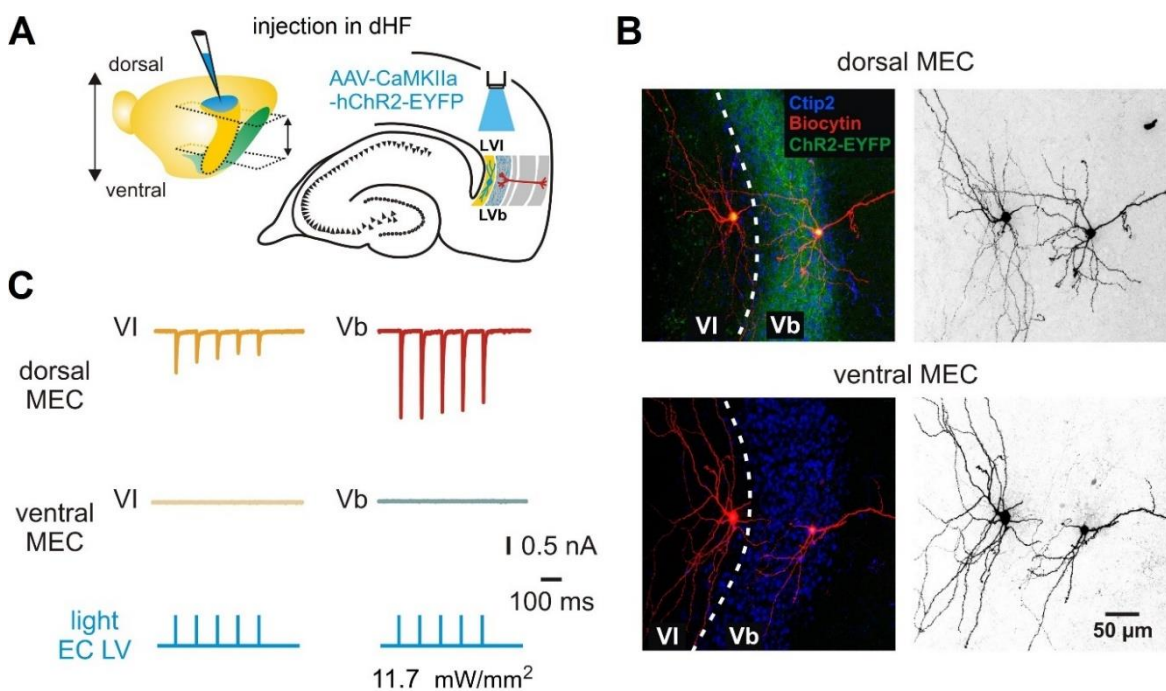


Figure 21. Functional connectivity between the dorsal HF and MEC layer VI principal neurons. (A) Left: illustration of the injection site (blue) in the dorsal HF with the approximate range of horizontal sections used in experiments indicated by arrows. Right: schematic drawing of a horizontal hippocampal-MEC slice showing the position of light stimulation used to activate the axons of dorsal hippocampal neurons infected with AAV-CaMKIIa-hChR2-EYFP. (B) Maximum intensity projection confocal images of representative horizontal slices from the dorsal (top) and ventral MEC (bottom), showing recorded LVI and LVb principal neurons labeled with biocytin, overlaid with Ctip2 labeling and fluorescent staining of hippocampal axons expressing hChR2-EYFP. Right images show the same neurons in black and white contrast. (C) Example EPSC traces recorded from LVI and LVb neurons in the same slice in the dorsal (top) and ventral MEC (middle) in response to 1 ms blue light pulses (bottom). Modified from Rannap et al. (in revision).

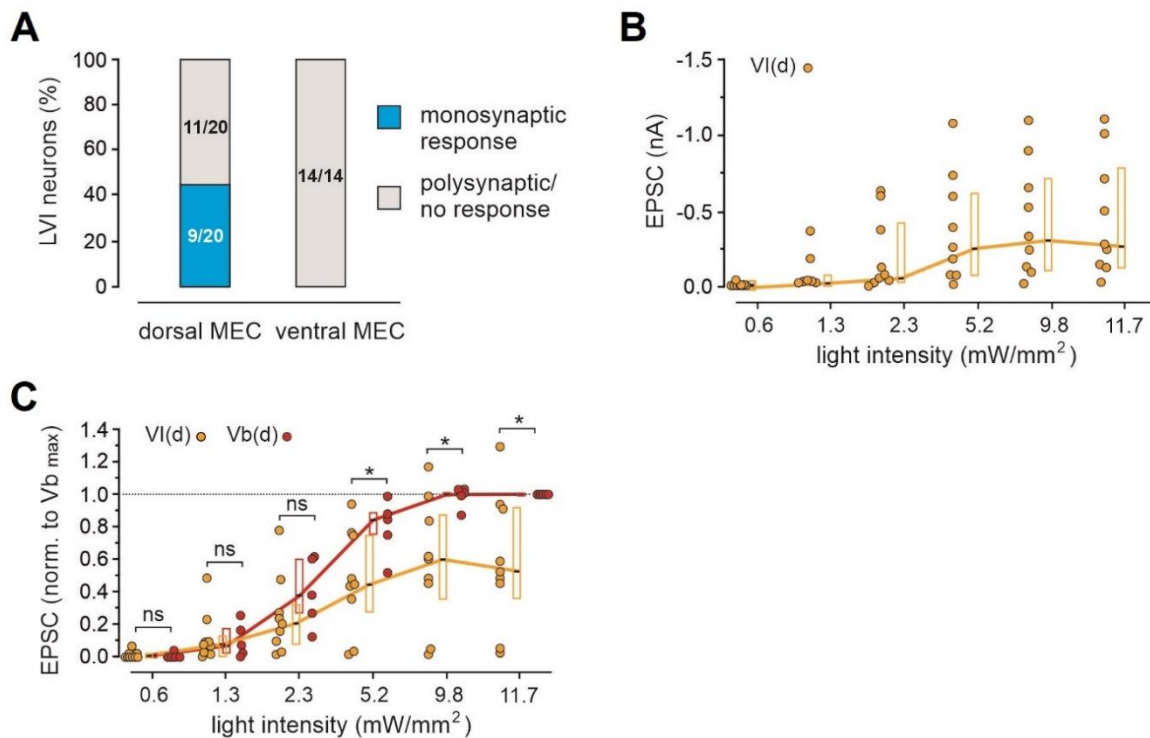


Figure 22. Quantification of dorsal hippocampal responses measured from LVI and LVb principal neurons in the dorsal and ventral MEC. (A) Proportion of monosynaptic responses recorded from LVI neurons in the dorsal or ventral MEC. (B) Quantification of EPSC amplitudes recorded from LVI neurons in the dorsal MEC in response to light pulses with increasing intensities (9 cells from 4 mice). (C) Values from B normalized to the highest LVb response at maximum light intensity (11.7 mW/mm²) in each slice in the dorsal MEC (VI(d), 9 cells from 4 mice; Vb(d), 5 cells from 4 mice; 11.7 mW/mm², $p = 0.016$, one-sample t-test). All data are presented as median (black line), 25th and 75th percentiles (box). Circles represent individual values. Mann-Whitney U test or one-sample t-test: * $p < 0.05$; ns, not significant. Modified from Rannap et al. (in revision).

Next, I recorded light-evoked responses from 20 LVI principal neurons in the dorsal half of MEC (Figures 21A and 21B). Roughly half (9/20) of the recorded cells exhibited EPSCs with short latencies and fast 20%-80% rise times (11.7 mW/mm², median: amplitude -0.29 nA, latency 2.27 ms, 20%-80% rise time 0.78 ms; Figures 21C, 22A and 22B), suggesting monosynaptic input to these cells. Two recorded cells did not respond to light stimulation and the remaining nine cells responded with latencies above 3.5 ms (median 6.52 ms), indicating polysynaptic input. Having previously analyzed the innervation of LV by dorsal hippocampal projections in detail, I subsequently compared the strength of innervation between monosynaptically innervated LVI and LV principal neurons by recording light-evoked EPSCs from LVb principal cells in the same slices as LVI responses (Figures 21B and 21C). I then normalized the LVI responses in each slice to LVb EPSC amplitudes at

maximum light intensity. This analysis revealed that dorsal hippocampal projections drive LVI neurons only half as strongly as LVb cells (11.7 mW/mm^2 , median: LVb, 1.00; LVI, 0.52; Figure 22C). A similar difference in innervation strength for dorsal hippocampal projections was previously seen for LVa principal cell amplitudes after normalization to LVb responses (Figure 12A, right panel).

Finally, I investigated how dorsal hippocampal projections target LVI FS interneurons by recording light-evoked responses from 15 FS cells in the dorsal half of MEC (Figures A6A and A6B). The majority (12/15) of recorded interneurons exhibited EPSCs with latencies below 3.5 ms (median 1.85 ms, Figures 23A and A6C), representing a larger fraction of monosynaptically responding cells, compared to LVI principal neurons. Nevertheless, EPSC amplitudes in FS interneurons were similar to amplitudes measured from principal cells (11.7 mW/mm^2 , median -0.32 nA; Figure 23B). The electrophysiological data thus fully aligned with results from anatomical tracing experiments, confirming that in the dorsal MEC dorsal hippocampal projections innervate both LVI principal cells and FS interneurons comparably strongly to LVa principal neurons.

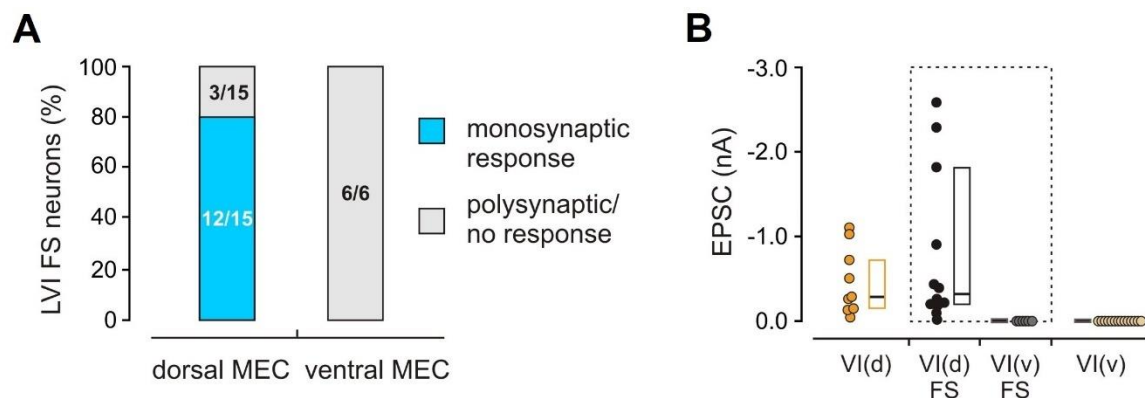


Figure 23. Quantification of dorsal hippocampal responses measured from LVI FS interneurons in the dorsal and ventral MEC. (A) Proportion of monosynaptic responses recorded from LVI FS interneurons recorded in the dorsal or ventral MEC. (B) Quantification of EPSC amplitudes recorded from LVI FS cells in the dorsal [VI FS(d)] or ventral MEC [VI FS(v)] in response to maximum intensity light pulses (11.7 mW/mm^2 , VI FS(d), 12 cells from 5 mice; VI FS(v), 6 cells from 4 mice). Amplitude values for FS cells are compared with respective LVI principal neuron amplitudes from Figure 22B. All data are presented as median (black line), 25th and 75th percentiles (box). Circles represent individual values. Modified from Rannap et al. (in revision).

3.2.3 Functional connectivity between the ventral HF and MEC layer VI

Next, I functionally evaluated ventral hippocampal projections to MEC LVI by injecting the AAV vector expressing hChR2-EYFP into ventral hippocampal area CA1 (Figures A5C and A5D). Across individual injections, I consistently observed moderately strong axonal labeling in LVI in the ventral half of MEC and weak to minimal labeling in the dorsal MEC (Figures 24B and A8B). I first recorded light-evoked responses from 14 LVI principal neurons in the ventral half of MEC (Figures 24A and 24B).

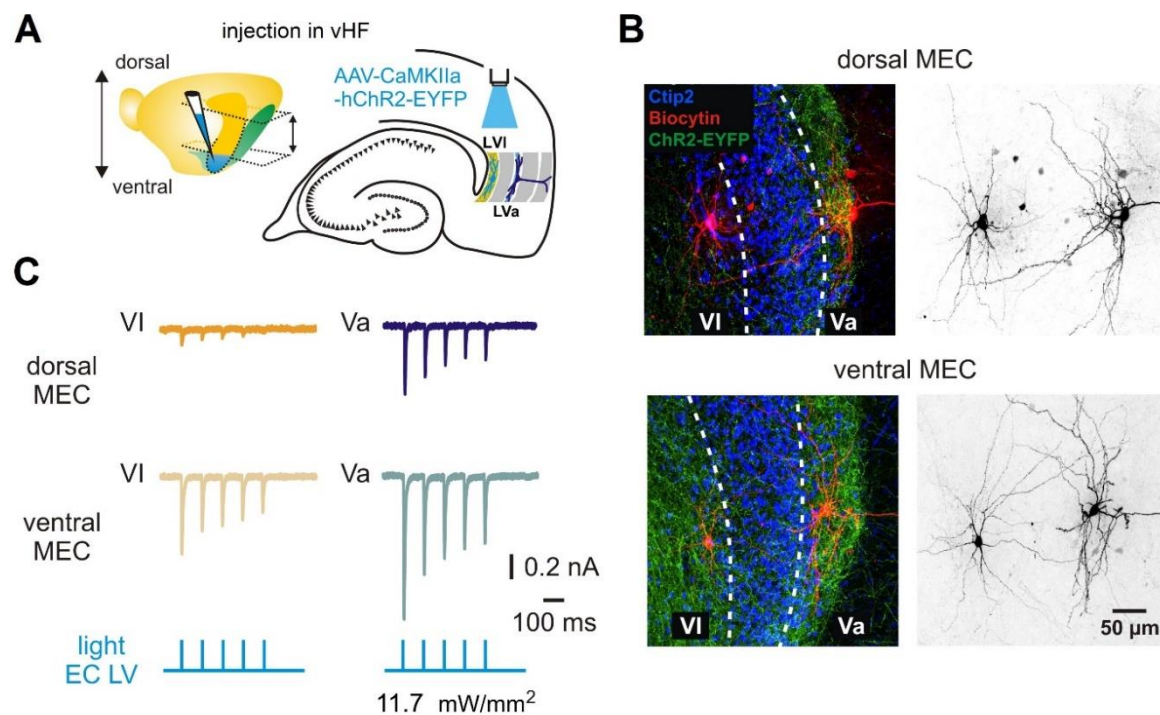


Figure 24. Functional connectivity between the ventral HF and MEC layer VI principal neurons. (A) Left: illustration of the injection site (blue) in the ventral HF with the approximate range of horizontal sections used in experiments indicated by arrows. Right: schematic drawing of a horizontal hippocampal-MEC slice showing the position of light stimulation used to activate the axons of ventral hippocampal neurons infected with AAV-CaMKIIa-hChR2-EYFP. (B) Maximum intensity projection confocal images of representative horizontal slices from the dorsal (top) and ventral MEC (bottom), showing recorded LVI and LVa principal neurons labeled with biocytin, overlaid with Ctip2 labeling and fluorescent staining of hippocampal axons expressing hChR2-EYFP. Right images show the same neurons in black and white contrast. (C) Example EPSC traces recorded from LVI and LVa neurons in the same slice in the dorsal (top) and ventral MEC (middle) in response to 1 ms blue light pulses (bottom). Modified from Rannap et al. (in revision).

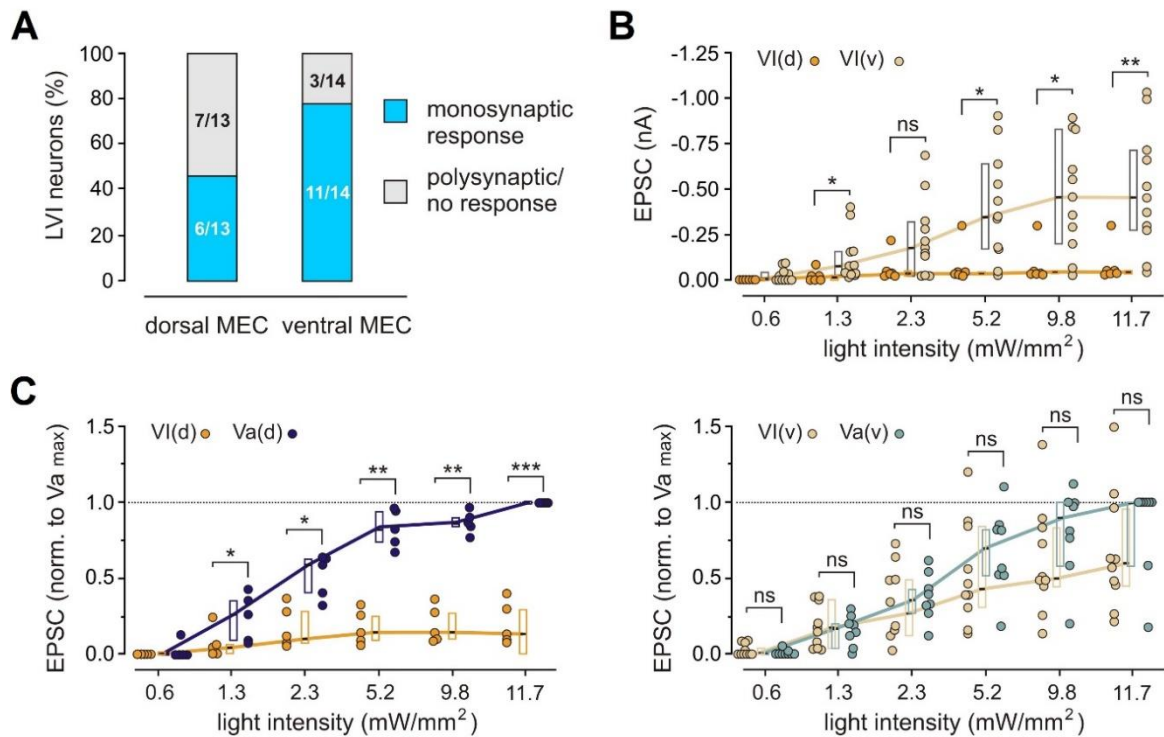


Figure 25. Quantification of ventral hippocampal responses measured from LVI and LVA principal neurons in the dorsal and ventral MEC. (A) Proportion of monosynaptic responses recorded from LVI neurons in the dorsal or ventral MEC. (B) Quantification of EPSC amplitudes recorded from LVI neurons in the dorsal [VI(d)] or ventral MEC [VI(v)] in response to light pulses with increasing intensities (VI(d), 6 cells from 4 mice; VI(v), 11 cells from 5 mice; 11.7 mW/mm², $p = 0.0057$, Mann-Whitney U test). (C) Values from B normalized to the highest LVA response at maximum light intensity (11.7 mW/mm²) in each slice in the dorsal (left, VI(d), 5 cells from 4 mice; Va(d), 5 cells from 4 mice; 11.7 mW/mm², $p = 0.0002$, one-sample t-test) or ventral MEC (right, VI(v), 10 cells from 5 mice; Va(v), 8 cells from 5 mice; 11.7 mW/mm², $p = 0.258$, Mann-Whitney U test). All data are presented as median (black line), 25th and 75th percentiles (box). Circles represent individual values. For all statistical tests: *** $p < 0.001$; ** $p < 0.01$; * $p < 0.05$; ns, not significant. Modified from Rannap et al. (in revision).

The majority (11/14) of recorded ventral LVI cells responded to light stimulation with short latency EPSCs showing fast 20%-80% rise times (11.7 mW/mm², median: amplitude -0.45 nA, latency 2.36 ms, 20%-80% rise time 1.22 ms; Figures 24C, 25A and 25B), suggesting monosynaptic innervation of these cells. The remaining three cells responded with considerably longer latencies (median 8.32 ms), consistent with polysynaptic input. In this case, I additionally confirmed the monosynaptic glutamatergic nature of the synaptic inputs using pharmacology. I first perfused the slice with the GABAA receptor antagonist gabazine and subsequently with the AMPA and kainate receptor antagonist CNQX (Figure A7A).

While light-evoked EPSC amplitudes were unaffected by gabazine, the responses were almost completely blocked by CNQX (Figure A7A). This indicated that the currents were indeed induced by glutamate release. Importantly, during CNQX perfusion I was still able to reliably record NMDA receptor currents by holding the cell at a positive holding potential (+40 mV, Figure A7A). As all polysynaptic activity in the slice would have been blocked by CNQX, the release of glutamate driving the NMDA receptor currents must have been monosynaptic (Ben-Simon et al., 2022).

I next recorded light-evoked responses from 13 LVI principal neurons in the dorsal half of MEC (Figures 24A and 24B). In contrast to the reliable monosynaptic responses observed in ventral LVI, less than half (6/13) of the recorded neurons in dorsal LVI exhibited short latency EPSCs (11.7 mW/mm², median: latency 2.36 ms, 20%-80% rise time 1.04 ms; Figures 24C and 25A). Moreover, EPSC amplitudes in the responding cells were minimal (11.7 mW/mm², median: amplitude -45 pA; Figure 25B). I then compared the strength of ventral hippocampal innervation between layers VI and V. As LVA neurons were previously shown to receive strong ventral hippocampal input along the entire dorsoventral MEC axis, I recorded light-evoked EPSCs from LVA principal cells in the same slices as LVI responses (Figures 24B and 24C) and subsequently normalized the LVI responses in each slice to LVA EPSC amplitudes at maximum light intensity. In the ventral MEC, this analysis revealed a non-significant trend towards weaker responses in LVI neurons, compared to LVA cells (11.7 mW/mm², median: LVA, 1.00; LVI, 0.60; Figure 25C, right panel). In the dorsal MEC, in contrast, normalized EPSC amplitudes recorded from LVI neurons were over sevenfold smaller than amplitudes recorded from LVA cells (11.7 mW/mm², median: LVA, 1.00; LVI, 0.13; Figure 25C, left panel).

Lastly, I examined the innervation of LVI FS interneurons by ventral hippocampal projections by recording light-evoked responses from 8 FS cells in both ventral and dorsal LVI (Figures A8A and A8B). Overall, the innervation patterns for FS interneurons were comparable to LVI principal cells. In ventral LVI, light stimulation evoked putative monosynaptic EPSCs (median latency 1.97 ms) in the majority (6/8) of FS cells (Figure 26A), with the responding cells exhibiting similar amplitudes to LVI principal neurons (11.7 mW/mm², median -0.41 nA; Figures 26B and A8C). In contrast, only half (4/8) of the recorded dorsal FS interneurons responded to light stimulation (Figure 26A), displaying consistently smaller amplitudes (11.7 mW/mm², median: amplitude -86 pA, latency 2.11 ms; Figures 26B and A8C). Together, these results revealed that ventral hippocampal innervation

of LVI principal cells and FS interneurons is mostly confined to the ventral MEC, mirroring the topography seen for ventral hippocampal projections to LVb.

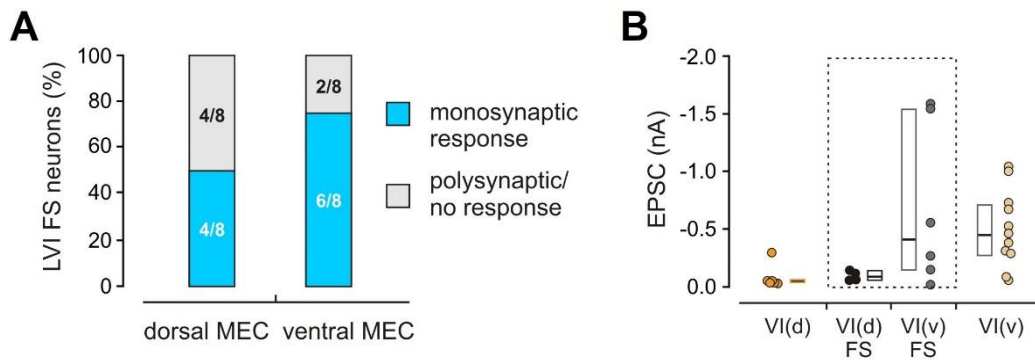


Figure 26. Quantification of ventral hippocampal responses measured from LVI FS interneurons in the dorsal and ventral MEC. (A) Proportion of monosynaptic responses recorded from LVI FS interneurons recorded in the dorsal or ventral MEC. (B) Quantification of EPSC amplitudes recorded from LVI FS interneurons in the dorsal [VI FS(d)] or ventral MEC [VI FS(v)] in response to maximum intensity light pulses (11.7 mW/mm^2 , VI FS(d), 4 cells from 3 mice; VI FS(v), 6 cells from 6 mice). Amplitude values for FS cells are compared with respective LVI excitatory neuron amplitudes from Figure 25B. All data are presented as median (black line), 25th and 75th percentiles (box). Circles represent individual values. Modified from Rannap et al. (in revision).

3.3 Layer VI microcircuitry in MEC deep layers

3.3.1 Local connectivity within layer VI

While the connectivity between LVA and LVb principal cells and FS interneurons has recently been investigated in detail (Ohara et al., 2021; Rozov et al., 2020), how LVI neurons are integrated into the MEC deep layer circuitry remains unknown. Having established an intricate layer-specific connectivity scheme between HF output structures and different MEC deep layers, I next investigated how LVI neurons participate in the processing of hippocampal output signals received by the MEC deep layer network. As signal flow within neuronal networks is constrained by connectivity between individual neurons, I characterized functional connectivity between different combinations of LVI and LV principal cells and FS interneurons using a series of paired patch clamp recordings.

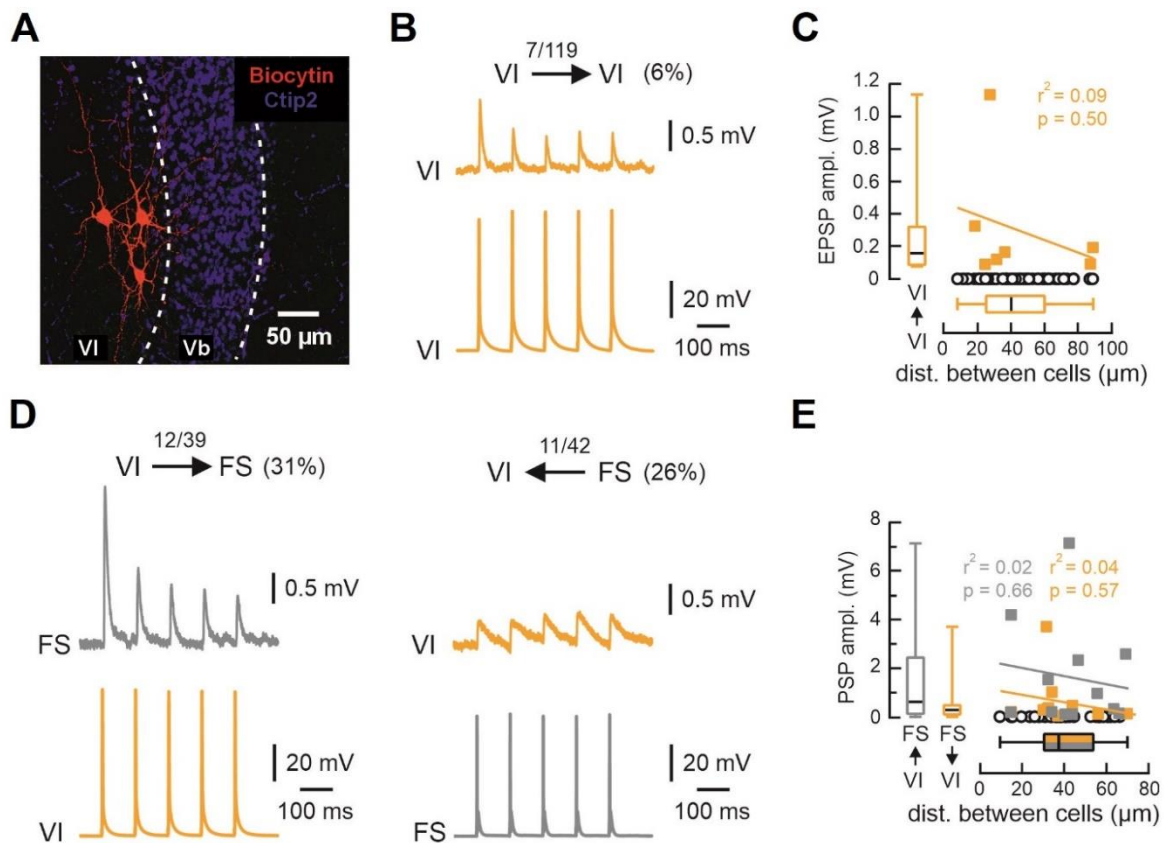


Figure 27. Local connectivity within MEC layer VI. (A) Maximum intensity projection confocal image of a typical horizontal slice showing recorded MEC LVI principal neurons labeled with biocytin, overlaid with Ctip2 staining. (B) Example traces from a paired recording between connected LVI excitatory neurons, showing presynaptic action potentials and associated PSPs. (C) PSP amplitudes from all tested VI-to-VI pairs relative to the distance between recorded neurons. Yellow squares represent connected and open black circles non-connected pairs (note the large number of non-connected pairs). The box plot for PSP amplitudes and the correlation analysis represent data from connected pairs only, while the box plot for distances represents all recorded cells. (D) Example traces from paired recordings between connected LVI excitatory and FS interneurons. (E) Same analysis as in C for all tested VI-to-FS (connected pairs in gray) and FS-to-VI pairs (connected pairs in yellow). Modified from Rannap et al. (in revision).

To gain insight into signal propagation within LVI, I first examined local connectivity between LVI neurons. Paired recordings between LVI principal cells revealed relatively sparse interconnectivity (5.9%, 7 of 119 pairs; Figures 27A-27C). In all connected pairs, repeated presynaptic stimulation caused marked depression of the postsynaptic responses (Figure A9A, top panel), indicating robust attenuation of locally transmitted signals. In contrast, connections between LVI principal cells and FS interneurons were relatively frequent in both directions: LVI principal cells innervated local FS interneurons in 30.8% of

tested pairs (12 of 39 pairs; Figures 27D, left, 27E, and A9A, middle panel) and FS interneurons were connected to LVI principal cells in 26.2% of tested pairs (11 of 42 pairs; Figures 27D, right, 27E and A9A, bottom panel). To determine whether these connectivity patterns differ along the dorsoventral MEC axis, I combined all recorded sections from the dorsal MEC into a dorsal and sections from the ventral MEC into a ventral group. I then compared connection frequencies and various PSP parameters between the two groups, finding no significant differences in connectivity and a single difference in PSP properties (Table B2).

3.3.2 Interlaminar connectivity between layers VI and Vb

I next investigated signal transmission between neurons in MEC layers VI and Vb. Paired recordings between LVI and LVb principal cells revealed minimal connectivity: I only found a single weak connection from LVI to LVb principal neurons (1 of 120 pairs; Figures 28A and 28B, left) and failed to find any connections in the opposite direction (0 of 122 Vb-to-VI pairs; Figures 28A and 28B, right). In stark contrast, I observed relatively frequent connections between principal cells and FS interneurons. Principal cells in LVb innervated LVI FS interneurons in 23.8% of tested pairs (10 of 42 pairs; Figures 29D, 29E, left and 29F) and LVI FS interneurons innervated LVb principal cells in 30% of tested pairs (12 of 40 pairs; Figures 29D, 29E, right, 29F, and A9B, bottom panel).

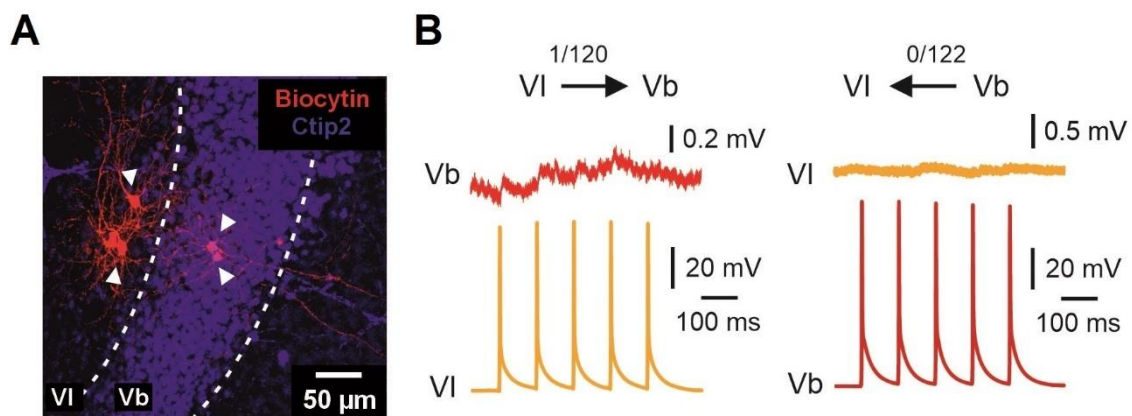


Figure 28. Interlaminar connectivity between MEC LVI and LVb principal cells. (A) Maximum intensity projection confocal image of a typical horizontal slice showing recorded MEC LVI and LVb principal neurons (white arrowheads) labeled with biocytin, overlaid with Ctip2 staining. (B) Example traces from paired recordings between LVI and LVb principal neurons, showing presynaptic action potentials and for the single VI-to-Vb connection the associated PSPs.

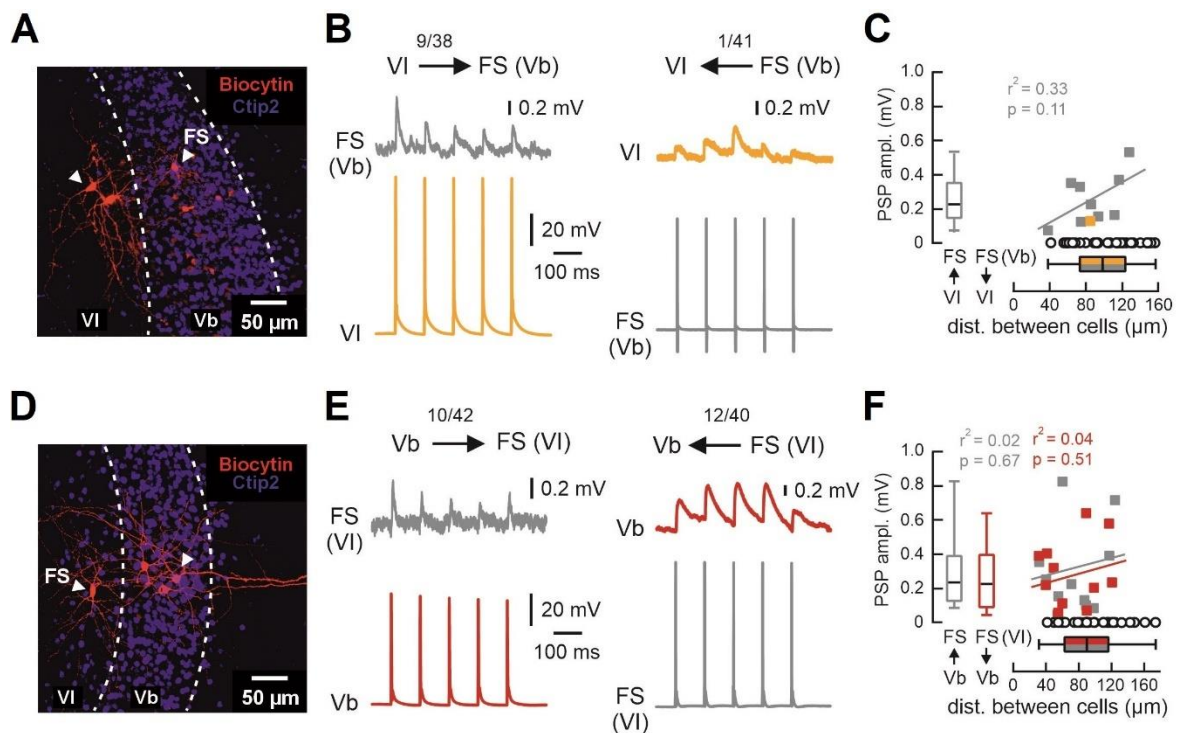


Figure 29. Interlaminar connectivity between MEC LVI and LVb principal cells and fast-spiking interneurons. (A) Maximum intensity projection confocal image showing recorded LVI principal cells and a LVb FS interneuron labeled with biocytin, overlaid with Ctip2 staining. The LVI cell indicated by the white arrowhead was connected to the FS interneuron. (B) Example traces from paired recordings between connected LVI excitatory and LVb FS interneurons, showing presynaptic action potentials and the associated PSPs. (C) PSP amplitudes from all tested pairs relative to the distance between recorded neurons. Gray squares represent connected VI-to-FS (Vb) pairs, the yellow square the single connected FS (Vb)-to-VI pair, and open black circles non-connected pairs (note the large number of non-connected pairs). The box plot for PSP amplitudes and the correlation analysis represent data from connected pairs only, while the box plot for distances represents all recorded cells. (D) Maximum intensity projection confocal image showing a recorded LVI FS interneuron and LVb principal cells labeled with biocytin, overlaid with Ctip2 staining. The LVb cell indicated by the white arrowhead was reciprocally connected to the FS interneuron. (E) Example traces from paired recordings between connected LVb excitatory and LVI FS interneurons. (F) Same analysis as in C for all tested Vb-to-FS (VI) (connected pairs in gray) and FS (VI)-to-Vb pairs (connected pairs in red). Modified from Rannap et al. (in revision).

Interestingly, while connections from principal cells to FS interneurons are generally depressing, presynaptic action potential trains in LVb principal neurons induced facilitating responses in most connected LVI FS cells (Figure A9B, middle panel). LVI principal cells were connected to LVb FS interneurons in 23.7% of tested pairs (9 of 38 pairs; Figures 29A, 29B, left, and 29C), with the postsynaptic responses expectedly depressing (Figure A9B, top

panel). As a notable exception, connectivity from LVb FS interneurons to LVI principal cells was very sparse (1 of 41 pairs; Figures 29A, 29B, right, and 29C). To examine whether the observed connectivity patterns vary along the dorsoventral MEC axis, I again combined sections from dorsal and ventral MEC levels into a dorsal and a ventral group, respectively. As before, there were no significant differences in connection frequencies and only two differences in PSP properties between the two groups (Table B3). Overall, my recordings revealed a general lack of excitatory and a prevalence of inhibitory connections between layers VI and Vb (summarized in Figure 30), suggesting the layers predominantly communicate via inhibitory interneurons.

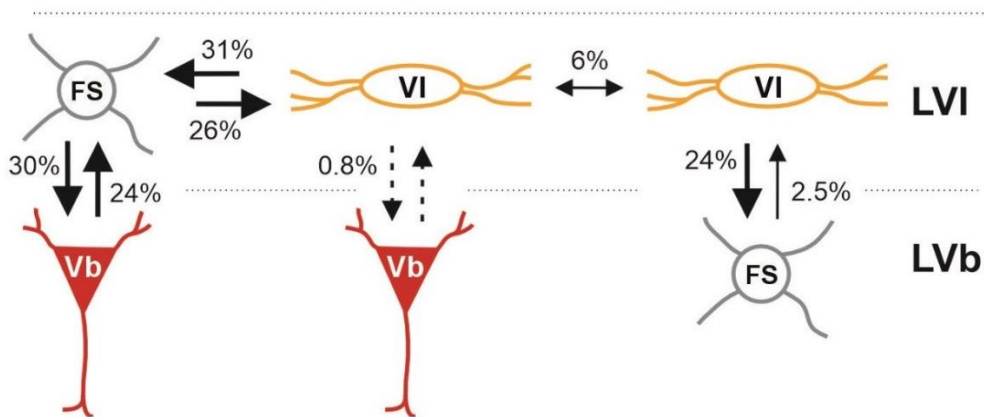


Figure 30. Overview of functional connectivity within LVI and between layers VI and Vb. Shown is a schematic representation of intra- and interlaminar connectivity between LVI and LVb principal cells and FS interneurons. No functional connections from LVb to LVI principal cells were found. Modified from Rannap et al. (in revision).

3.3.3 Interlaminar connectivity between layers VI and Va

Finally, I explored whether MEC LVI principal neurons form functional connections with LVa principal cells and thereby potentially modulate entorhinal output signals to neocortical networks. Similarly to the minimal connectivity observed between LVI and LVb principal cells, paired recordings between LVI and LVa principal neurons revealed only one functional connection from LVa to LVI cells (1 of 94 pairs; Figures 31A and 31B, right) and no connections from LVI to LVa neurons (0 of 89 pairs; Figures 31A and 31B, left). An important caveat when interpreting data from paired recordings is that the chance of finding connections between pairs of neurons decreases with distance. The recorded LVI and LVa neuron pairs were routinely separated by more than 200 μm (median 195.8 μm), representing a distance at which the chance of finding connections under normal circumstances may be low (Jiang et al., 2015). To mitigate the effect of distance, I sectioned

the brains using a specific cutting angle that had been optimized to best preserve axonal connectivity (see Section 2.1.3 for details). This resulted in slices where the axons of both LVa and LVI cells were oriented parallel to the slice surface and could be regularly traced for considerable distances. For all tested pairs, I further quantified the proximity of LVa axons to recorded LVI cells by measuring the nearest distance between an axonal fiber of the LVa cell and the soma of the LVI neuron. This analysis revealed that in 82% of tested pairs at least one LVa axon collateral passed within 50 μm of the LVI cell soma, with a median distance of 25 μm ($n = 94$). This lends additional support to low connectivity between LVa and LVI principal neurons, as strong connectivity would likely have been detected with my approach.

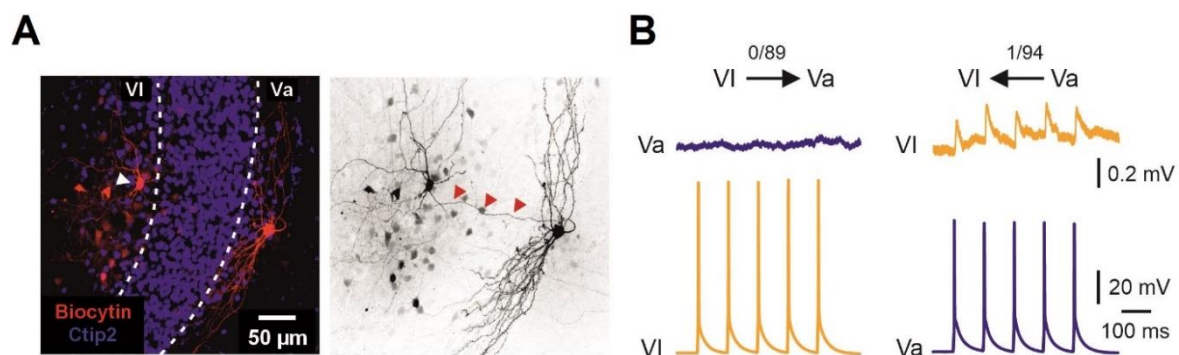


Figure 31. Interlaminar connectivity between MEC layers VI and Va. (A) Maximum intensity projection confocal image of a typical horizontal slice showing a recorded MEC LVI (white arrowhead) and a LVa principal neuron labeled with biocytin, overlaid with Ctip2 staining. The right image shows the same neurons in black and white contrast, red arrowheads indicate the axon of the LVa cell. (B) Example traces from paired recordings between LVI and LVa excitatory neurons showing presynaptic action potentials and for the single Va-to-VI connection the associated PSPs. Modified from Rannap et al. (in revision).

3.3.4 Functional connectivity from LVa to layers VI and Vb

Access to the Rbp4-Cre mouse line, which in MEC expresses Cre recombinase specifically in LVa principal neurons (Tsoi et al., 2022), allowed me to additionally examine projections from LVa to LVI neurons at the population level. Similarly to the interrogation of hippocampal projections, I again used an optogenetic approach where I expressed hChR2-EYFP specifically in MEC LVa principal cells. For this I used an AAV vector containing an inverted hChR2-EYFP transgene placed between two Cre recombination sequences. Because the transgene is only expressed in the correct orientation and inversion of the sequence depends on Cre recombinase, hChR2-EYFP is only produced in cells that express

Cre. I injected the AAV vector into dorsal or ventral LVa in Rbp4-Cre mice, resulting in strong fluorescent labeling in the layer (Figures 32A and 32B). I then recorded light-evoked EPSCs from 14 LVI principal neurons in the dorsal and 16 LVI principal cells in the ventral MEC (Figures 32A and 32B). For comparison, in each slice I additionally recorded responses from LVb principal neurons (Figures 32A and 32B) which have been shown to be sparsely innervated by LVa principal cells (Rozov et al., 2020). In all recorded LVI neurons, light stimulation evoked short latency responses (median: 2.15 ms, n = 30; LVI dorsal, 2.10 ms, n = 14; LVI ventral, 2.26 ms, n = 16) with fast 20%-80% EPSC rise times (median: 1.07 ms, n = 30; LVI dorsal, 1.05 ms, n = 14; LVI ventral, 1.11 ms, n = 16), consistent with mono-synaptic input from LVa principal cells. EPSC amplitudes in the recorded neurons, however, were generally small (11.7 mW/mm^2 , median -88 pA, n = 30). Further comparison of LVI amplitudes between the dorsal and ventral MEC revealed them to be comparable (11.7 mW/mm^2 , median: LVI dorsal, -110 pA; LVI ventral, -88 pA; Figures 32C and 32D).

I next analyzed responses recorded from LVb principal neurons. All LVb cells similarly exhibited short latency EPSCs (median: 2.21 ms, n = 26; LVb dorsal, 2.32 ms, n = 12; LVb ventral, 2.18 ms, n = 14) with fast 20%-80% EPSC rise times (median: 0.79 ms, n = 26; LVb dorsal, 0.78 ms, n = 12; LVb ventral, 0.80 ms, n = 14). Furthermore, combined LVb EPSC amplitudes across both dorsal and ventral MEC halves (11.7 mW/mm^2 , median -71 pA, n = 26) were comparable to responses measured from LVI neurons ($p = 0.941$, Mann-Whitney test). In contrast to LVI amplitudes, however, LVb responses displayed a clear difference along the dorsoventral MEC axis, where responses recorded in the dorsal MEC were almost six times weaker than ventral responses (11.7 mW/mm^2 , median: LVb dorsal, -31 pA; LVb ventral, -176 pA; Figures 32C and 32D). To verify that this discrepancy in LVI and LVb responses is not due to differences in hChR2 expression levels between individual injections, I normalized EPSC amplitudes recorded from both LVI and LVb neurons to the highest LVb current amplitude in each slice. Comparison of the normalized amplitudes revealed that the minimal responses recorded from LVb neurons in the dorsal MEC were significantly weaker than amplitudes recorded from LVI neurons, whereas in the ventral MEC this dynamic was reversed with significantly stronger responses seen in LVb neurons (11.7 mW/mm^2 , median: LVb dorsal, 1.00; LVI dorsal, 3.05; LVb ventral, 1.00; LVI ventral, 0.47; Figure 32E). These results were thus in general agreement with the sparse innervation of LVI neurons by LVa principal cells observed in paired recordings and additionally revealed a previously unknown dorsoventral topography from LVa to LVb principal neurons.

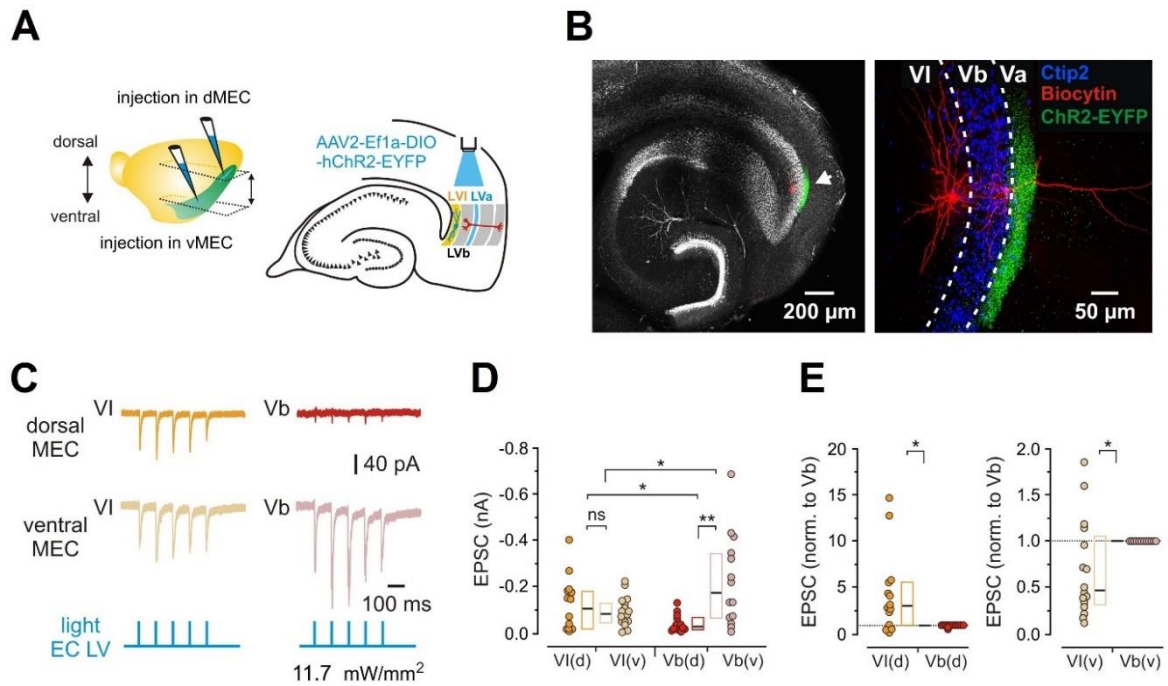


Figure 32. Functional connectivity from LVA to LVI principal neurons. (A) Left: illustration of the AAV2-Ef1a-DIO-hChR2-EYFP injection site (blue) in dorsal (dMEC) or ventral MEC (vMEC) LVA in Rbp4-Cre mice. Right: schematic drawing of a horizontal hippocampal-MEC slice showing the position of light stimulation used to activate the axons of LVA neurons expressing hChR2-EYFP. (B) Left: low magnification confocal image of a representative horizontal slice from a virus-injected Rbp4-Cre mouse showing the specific expression of hChR2-EYFP in MEC LVA. Right: maximum intensity projection confocal image from the indicated region in the left image showing a recorded MEC LVI and a LVb principal neuron labeled with biocytin, overlaid with Ctip2 labeling and hChR2-EYFP staining. (C) Example EPSC traces recorded from LVI and LVb neurons in the dorsal (top) and ventral MEC (middle) in response to 1 ms blue light pulses (bottom). (D) Quantification of EPSC amplitudes from LVI and LVb neurons in the dorsal (d) or ventral MEC (v) in response to maximum intensity (11.7 mW/mm²) light pulses (VI(d), 14 cells from 7 mice; VI(v), 16 cells from 6 mice; Vb(d), 12 cells from 7 mice; Vb(v), 14 cells from 6 mice; $p = 0.372$ for VI(d) vs. VI(v), $p = 0.017$ for VI(v) vs. Vb(v) and $p = 0.036$ for VI(d) vs. Vb(d), all unpaired t-test). (E) Values from D normalized to the highest LVb response in each slice in the dorsal (left, VI(d), 14 cells from 7 mice; Vb(d), 12 cells from 7 mice; $p = 0.013$, one-sample t-test) or ventral MEC (right, VI(v), 16 cells from 6 mice; Vb(v), 14 cells from 6 mice; $p = 0.031$, one-sample t-test). All data are presented as median (black line), 25th and 75th percentiles (box). Circles represent individual values. For all statistical tests: ** $p < 0.01$; * $p < 0.05$; ns, not significant. Modified from Rannap et al. (in revision).

4 DISCUSSION

In the present study, we combined anatomical and optogenetic circuit mapping to comprehensively characterize the organization of the hippocampal output pathway to MEC deep layers. Our results confirm that hippocampal output projections preferentially target MEC LV but extend earlier tracing studies to uncover a previously unknown sublayer-specific connectivity scheme. We show that while projections originating in the dorsal HF primarily target principal cells in LVb, ventral hippocampal projections preferentially innervate principal neurons in LVa (Figure 33A). Importantly, the ventral hippocampal projection to LVa exhibits a unique widespread connectivity pattern where target cells are innervated along the entire dorsoventral MEC axis (Figure 33A). As LVa principal neurons form the main source of entorhinal outputs to telencephalic structures, the different targeting of LVa by the dorsal and ventral HF has major implications for the transfer of signals from hippocampal to neocortical networks. Our data additionally reveal that hippocampal projections reliably target principal cells and FS interneurons in MEC LVI (Figure 33A). The strength of this innervation, however, is weaker than for LV, being comparable to LVa in the case of dorsal and LVb in the case of ventral hippocampal outputs.

Secondly, I used paired patch clamp recordings to investigate the integration of LVI neurons into the MEC deep layer circuitry. I find that interlaminar connections between principal cells in LVI and both LV sublayers are very sparse, whereas connections between principal cells and FS interneurons are considerably more frequent (Figure 30). The lack of excitatory connectivity between layers VI and V suggests that hippocampal output signals received by either layer are processed largely independently of the other subnetwork. As excitatory connections were previously also found to be sparse between sublayers Va and Vb (Ohara et al., 2021; Rozov et al., 2020), together these results indicate that parallel signal processing through different neuronal subnetworks might be a general feature of all MEC deep layers.

4.1 Dorsoventral organization of hippocampal projections to MEC deep layers

Reciprocal connections between MEC and HF are classically thought to follow a roughly parallel topography along the dorsoventral axes of both structures. Efferent entorhinal

projections originating at dorsal MEC levels project to the dorsal HF and efferent projections from ventral MEC levels to the ventral HF (Dolorfo and Amaral, 1998; van Groen et al., 2003). In turn, hippocampal output projections from the dorsal HF have been reported to target dorsal MEC levels and projections from the ventral HF ventral MEC levels (Cenquizca and Swanson, 2007; Kloosterman et al., 2003b). Our present results confirm this parallel topography for all hippocampal-medial entorhinal projections originating in the dorsal half of HF and corroborate a generally parallel topography for hippocampal output projections to layers VI and Vb originating in the ventral half of HF (Figure 33A).

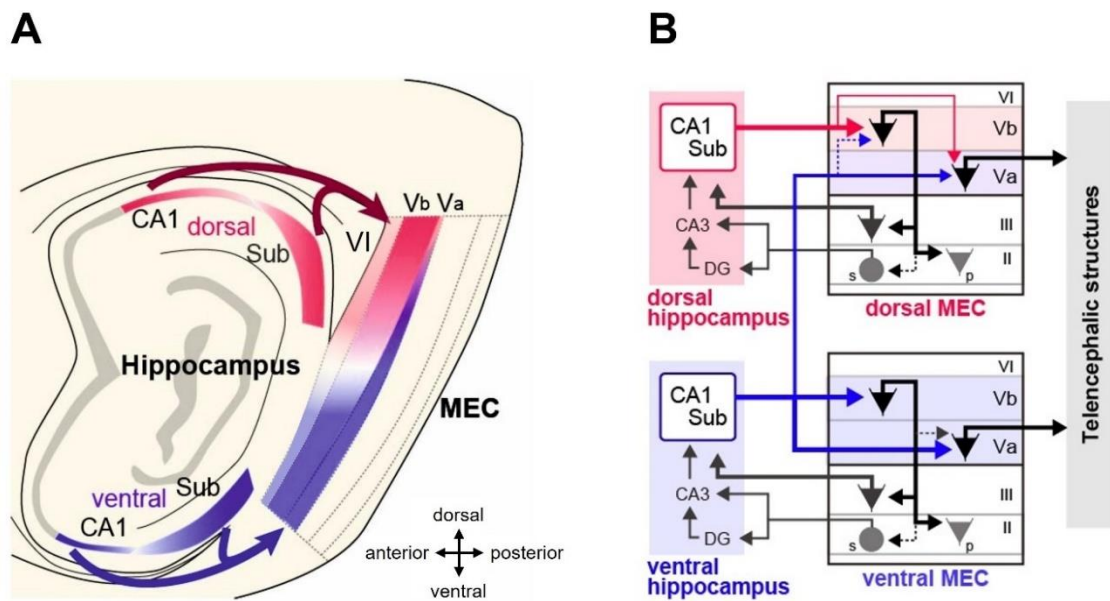


Figure 33. Schematic diagram of the hippocampal output circuit via the medial entorhinal cortex. (A) Hippocampal output projections from dorsal CA1 and Sub distribute in the dorsal MEC, where they predominantly innervate LVb and to a lesser extent LVa and LVI neurons. In turn, output projections from ventral CA1 and Sub innervate LVa, LVb and more weakly LVI neurons in the ventral MEC. Importantly, the ventral hippocampal projection to LVa is not confined to the ventral MEC but also distributes extensively in the dorsal MEC. Ventral hippocampal outputs thus target LVa neurons throughout the dorsoventral MEC axis. (B) Dorsal hippocampal output signals are mainly conveyed back to the hippocampus via the MEC LVb → MEC LIII → hippocampus loop circuit. In contrast, information from the ventral hippocampus is sent out to telencephalic structures via the MEC layer Va output circuit. Notably, weak dorsal hippocampal innervation of LVa neurons in the dorsal MEC raises the possibility that dorsal and ventral hippocampal output signals converge in dorsal LVa neurons, potentially allowing dorsal hippocampal information to reach telencephalic structures. See also Figure 2. s, stellate cell; p, pyramidal cell. The figure was created by Dr. Shinya Ohara and was modified from Ohara et al., 2023.

Surprisingly, we find that ventral hippocampal output projections to MEC LVa fundamentally deviate from this general pattern. We observed ventral hippocampal fibers in the dorsalmost portion of LVa and saw strong activation of LVa principal neurons by ventral hippocampal outputs in the dorsal MEC, indicating that ventral hippocampal projections prominently target dorsal LVa (Figure 33). The discrepancy between previous anatomical reports and our current findings is likely explained by the choice of anatomical plane used to section the brain for analysis. Previous studies have generally examined the terminal distribution of hippocampal fibers in the coronal plane, where labeled fibers in dorsal LVa are difficult to follow due to the thinness and suboptimal angle of the layer relative to the coronal plane. Notably, in the study by Cenquizca and Swanson the authors described a band of hippocampal fibers originating in ventral CA1 that distributed in layer V at dorsal MEC levels (Figures 10D and 11B in Cenquizca and Swanson, 2007) but the authors nevertheless concluded an overall parallel topography.

4.2 Sublayer specificity of hippocampal projections to layer V

The recent discovery that MEC LV can be divided into two functionally distinct sublayers – Va and Vb – raises important questions about the processing of hippocampal output signals by the respective subnetworks. Principal cells in LVa project to the neocortex (Ohara et al., 2018; Sürmeli et al., 2015) and mediate the transfer of transient hippocampal representations to cortical areas for long-term storage (Kitamura et al., 2017). LVb neurons, in contrast, are a source of intraentorhinal projections which strongly target pyramidal cells in LIII (Ohara et al., 2021). How hippocampal output signals propagate to and are relayed between the two sublayers therefore has major implications for the flow of hippocampal information to local entorhinal versus remote neocortical networks.

It was initially suggested that dorsal hippocampal projections exclusively target neurons in LVb (Sürmeli et al., 2015). My own data subsequently confirmed the preferential targeting of LVb neurons by the dorsal HF but also identified a weak projection to LVa cells (Rozov et al., 2020). Intriguingly, efferent projections originating at intermediate hippocampal levels were found to innervate LVa and LVb cells with roughly similar strength (Rozov et al., 2020), suggesting that sublayer specificity of the hippocampal projection to MEC LV might depend on the dorsoventral level of origin. Our present data confirm this hypothesis, corroborating the preferential targeting of LVb by dorsal hippocampal outputs and revealing

that LVA is strongly targeted by the ventral HF (Figure 33). While we also observed dorsal hippocampal projections to LVA and ventral hippocampal projections to LVb, these were in both cases weaker than projections to the other LV sublayer. In particular, dorsal hippocampal outputs activated LVA principal cells less frequently and only half as strongly as neurons in LVb, indicating significantly reduced efficiency of dorsal hippocampal signal transmission to LVA. As excitatory interconnectivity between sublayers Va and Vb is sparse (Ohara et al., 2021; Rozov et al., 2020), these findings implicate the ventral HF in the transfer of hippocampal information to downstream neocortical networks (Figure 33B). In contrast, the dorsal HF appears to predominantly activate local projections to superficial entorhinal layers (Figure 33B). Because signals received by superficial entorhinal neurons are relayed back to HF (van Strien et al., 2009), this creates a hippocampal-medial entorhinal-hippocampal loop circuit (Figure 33B) that would support reverberating activity patterns which might stabilize current hippocampal representations. It should be noted that hippocampal output signals could also reenter the hippocampal network through LVA, as collateral fibers of LVA principal neurons were recently shown to directly target pyramidal neurons in area CA1 (Tsoi et al., 2022).

4.3 Convergence of dorsal and ventral hippocampal output signals in dorsal layer Va

The relatively weak activation of MEC LVA neurons by dorsal hippocampal outputs (Figure 33) suggests the efficiency of information transfer from the dorsal HF to the neocortex through the deep MEC network is significantly limited. Simultaneously, an interaction between dorsal hippocampal signals and downstream neocortical circuits must exist as selective dorsal HF lesions have been shown to disrupt long-term spatial memory (Fanselow and Dong, 2010). Output signals from the dorsal HF might reach downstream neocortical areas indirectly through extensive dorsal hippocampal projections to the retrosplenial cortex (Mitchell et al., 2018) or through dorsal subicular projections to anterior thalamic nuclei (Fanselow and Dong, 2010), as both of these structures are interconnected with various neocortical brain regions. Dorsal activity might partially also reach the neocortex directly through weak subicular projections to the orbitofrontal cortex (Jay and Witter, 1991). Alternatively, dorsal hippocampal signals could propagate within area CA1 to more ventral hippocampal levels through a network of longitudinally oriented associational connections

between CA1 pyramidal cells (Yang et al., 2014). Strong ventral hippocampal projections to MEC LVa would subsequently transmit the signals to the medial entorhinal-neocortical output pathway, circumventing the weak direct dorsal hippocampal projection to LVa.

Intriguingly, the innervation of dorsal LVa neurons by ventral hippocampal outputs, revealed by our present data (Figure 33), raises an additional possibility for dorsal hippocampal signals to reach the neocortex through the deep MEC network. In my recordings, I observed monosynaptic responses in all dorsal LVa neurons following the activation of ventral hippocampal fibers and 76% of LVa neurons following the activation of dorsal fibers, suggesting that a significant fraction of dorsal LVa neurons integrate signals from both the dorsal and ventral HF. While I have previously shown that in acutely prepared brain slices input from the dorsal HF in isolation is insufficient to evoke action potentials in dorsal LVa cells (Rozov et al., 2020), simultaneous input from the dorsal and ventral HF might provide sufficient excitation to induce spiking in a large enough fraction of neurons. Indeed, the aggregate absolute amplitude of dorsal and ventral hippocampal outputs to dorsal LVa cells in my recordings approached the amplitude of dorsal hippocampal outputs to LVb cells, which in our previous study were found to evoke action potentials in roughly half of all recorded LVb neurons (Rozov et al., 2020). Although compelling, future studies are needed to confirm the presence of this convergent pathway *in vivo*.

4.4 Potential functions of the convergent hippocampal output pathway to dorsal layer Va

The dorsal and ventral hippocampal halves are associated with fundamentally different functional roles. While the dorsal HF is strongly implicated in spatial memory, the ventral HF has been repeatedly shown to regulate stress responses and emotional behavior (Fanselow and Dong, 2010). The convergence of dorsal and ventral hippocampal output signals in dorsal LVa would thus allow spatial representations to be integrated with emotionally relevant stimuli. The requirement for simultaneous input from both hippocampal poles for sufficient activation of LVa cells would thereby create a gating mechanism, where a certain degree of emotional engagement is necessary for information to be committed to long-term memory. This mechanism might be involved in the association of spatial representations with aversive stimuli during contextual fear conditioning, which

was recently shown to depend on projections from MEC LVA to the prefrontal cortex (Kitamura et al., 2017).

Propagation of spatially modulated signals along the longitudinal hippocampal axis from dorsal to ventral levels was recently suggested to enable an animal to sense changes in the environmental context, where the contextual change would be communicated to other brain areas by ventral hippocampal outputs (Maurer and Nadel, 2021). Different oscillatory patterns within the hippocampus are known to travel from dorsal to ventral along the longitudinal axis (Lubenov and Siapas, 2009; Patel et al., 2013), accompanied by a gradual increase in the size of place cell firing fields (Jung et al., 1994). Dorsal hippocampal place fields are relatively small and alter their firing pattern in response to more modest changes in input, whereas place fields in the most ventral part of the hippocampus are much larger and require significant changes in input for their firing pattern to change. In the theory proposed by Maurer and Nadel, alterations in place cell firing patterns would propagate from clusters of cells with smaller place fields to cell clusters with progressively larger place fields (Maurer and Nadel, 2021). If the change in context is minor, the number of dorsal hippocampal cells that change their firing pattern would be small and the overall change in signal transmitted to the next cluster would be limited. Consequently, the number of cells in the next cluster that alter their firing would be even smaller and propagation of the signal towards ventral hippocampal levels would cease. In contrast, sufficiently large changes in context would cause a significant number of dorsal hippocampal cells to change their firing, allowing the altered firing behavior to reach the ventral hippocampal pole, from where it would be transmitted to the rest of the brain to signal a change in context (Maurer and Nadel, 2021). The strong ventral and weak dorsal hippocampal projection to MEC LVA, revealed by our present data (Figure 33), lends anatomical support to this theory. It further provides a mechanism by which contextual information could reach the entire LVA output pathway and, together with dorsal hippocampal signals, participate in the consolidation of contextual fear memories (Kitamura et al., 2017).

4.5 The hippocampal output projection to MEC layer VI

Several previous reports have noted the distribution of efferent hippocampal fibers in MEC LVI (Ben-Simon et al., 2022; Kloosterman et al., 2003b; O'Reilly et al., 2013; Swanson and Cowan, 1977) and two studies have demonstrated functional connectivity from Sub to LVI

using either field potential measurements (Kloosterman et al., 2003a) or patch clamp recordings combined with pharmacological activation of subicular neurons (Tu et al., 2009). Our present data confirm that both the dorsal and ventral HF send functional projections to MEC LVI, where they innervate both LVI principal cells and FS interneurons. At the same time, the distribution of labeled fibers in LVI in our experiments mirrored the distribution of fibers in the more weakly innervated LV sublayer – LVA in the case of dorsal and LVb in the case of ventral hippocampal projections. Furthermore, LVI neurons responded to the activation of hippocampal fibers less frequently and more weakly than neurons in LVb in the case of dorsal and LVA in the case of ventral hippocampal outputs. Our present results are thus consistent with previous studies that have established LV as the primary target layer of hippocampal projections to MEC (Kloosterman et al., 2003a, 2003b; O'Reilly et al., 2013; Swanson and Cowan, 1977; van Strien et al., 2009; Witter et al., 2000). Similarly to the weak dorsal hippocampal output to LVA, the limited efficiency of hippocampal signal transmission to LVI neurons might indicate that the cells integrate hippocampal information with input signals from other neuronal populations. These might include anterior thalamic nuclei which process head direction and episodic memory signals (Aggleton and O'Mara, 2022; Taube, 2007), the claustrum which is involved in multisensory integration and attention (Benarroch, 2021) but also deep layers of LEC, all of which have been shown to project to MEC LVI in anatomical tracing studies (Ben-Simon et al., 2022; Köhler, 1988). Future studies will have to determine how inputs from each of these brain regions contribute to signal processing in LVI neurons.

4.6 Local and interlaminar connectivity of LVI neurons

My paired recordings revealed relatively sparse interconnectivity between principal cells in MEC LVI (5.9%, Figure 30). In combination with the prominent short-term depression seen for all connections, this suggests LVI principal cells do not form a recurrent network for local signal amplification but rather function as a relay station for signal transmission to downstream targets. Similarly low connectivity values have been previously reported for connections between MEC LVb (5.9%, Rozov et al., 2020) and LIII principal neurons (5.7%, Winterer et al., 2017), whereas connectivity between principal cells in the recurrent LVA network is considerably higher (15.6%, Rozov et al., 2020).

Importantly, across my paired recordings I found almost no functional interlaminar connections between LVI and LVb or LVI and LVa principal cells. I additionally observed relatively weak postsynaptic responses in LVI neurons following optogenetic activation of the LVa principal neuron population in Rbp4-Cre mice. Light-evoked EPSC amplitudes measured from LVI neurons across the full dorsoventral MEC axis were comparable to responses measured from LVb neurons, which in previous paired recordings were shown to be sparsely innervated by LVa neurons (connectivity 3.4%, Rozov et al., 2020). Very sparse excitatory interconnectivity between MEC layers VI and V is consistent with recent anatomical tracing experiments that have demonstrated weak to minimal bidirectional connectivity between both LVI and LVb (Ben-Simon et al., 2022) as well as LVI and LVa (Ben-Simon et al., 2022; Shao et al., 2024). Furthermore, the vast majority of LVI neurons targeted by projections originating in LVa were recently shown to be interneurons, rather than principal cells (Shao et al., 2024). My present results are thus in line with these tracing studies and indicate that signals received by the LVI subnetwork are processed largely independently of LV circuits. As mentioned above, functional connectivity was previously also found to be sparse between principal neurons in MEC sublayers Va and Vb (Ohara et al., 2021; Rozov et al., 2020). The lack of excitatory connections was particularly striking in the dorsal MEC, where the innervation of LVa neurons by LVb cells was effectively absent (Ohara et al., 2021). My present optogenetic data in Rbp4-Cre mice confirm weak functional connections from LVa to LVb principal neurons and uncover an analogous dorsoventral gradient observed by Ohara et al., 2021, where connectivity from LVa to LVb cells in the dorsal MEC is almost absent. Together with the sparse excitatory connectivity between layers VI and V, these data suggest that independent signal processing within individual deep layer subnetworks is a general feature of all MEC deep layers. This is especially prominent in the dorsal MEC, where the complete functional segregation of sublayers Va and Vb highlights the separation of the hippocampal-medial entorhinal-hippocampal loop circuit from the LVa entorhinal output pathway.

In contrast to the sparse connectivity between principal cells, I observed relatively frequent connections between principal cells and FS interneurons both within LVI as well as between layers VI and Vb (Figure 30). Strong bidirectional connectivity between principal cells and FS interneurons within LVI indicates the presence of prominent excitatory-inhibitory loops that could give rise to local network oscillations. Oscillatory activity in the ripple frequency range has indeed been reported in MEC deep layers of behaving rodents *in vivo* (Chrobak

and Buzsáki, 1996). In turn, the inhibitory interactions between layers VI and V may serve to synchronize oscillatory activity between the layers, potentially recruiting different deep layer subnetworks into common oscillatory regimes (Klausberger and Somogyi, 2008). The activation of FS interneurons in the neighboring layer by both LVI and LVb principal cells might also suppress activity in the other subnetwork, inhibiting signal propagation in alternative pathways.

4.7 Potential functions of the hippocampal output pathway to layer VI

Until lately, the efferent connectivity and functional roles of MEC LVI neurons have remained almost entirely unexplored. Recently, the first detailed functional analysis of LVI principal neurons revealed that LVI neurons project back to all subfields of HF, providing the strongest excitatory drive onto CA3 pyramidal cells (Ben-Simon et al., 2022). This pathway is likely involved in the regulation of spatial information processing and memory formation, as both functions were impaired following the ablation or optical inhibition of the LVI cell population in vivo (Ben-Simon et al., 2022). In the same study, it was suggested that weak but highly orchestrated output from LVI neurons might help precisely coordinate the activation of hippocampal subnetworks, which might underlie the formation and stabilization of hippocampal place fields. Our present results indicate that within this model, LVI neurons could be recruited by direct hippocampal output projections from area CA1 or Sub. Due to the limited efficiency of hippocampal signal transmission to LVI, sufficient activation of the cells might require concurrent input from further neuronal populations. Highly orchestrated firing of LVI neurons might subsequently be achieved through precise excitatory-inhibitory interactions governed by the strong bidirectional connections between principal cells and FS interneurons within the layer.

Direct projections from hippocampal output structures to LVI allow hippocampal signals intended for consolidation in neocortical networks to be transmitted to LVI neurons. Interestingly, LVI neurons project to anterior thalamic nuclei (Ben-Simon et al., 2022) which have recently come to prominence as an alternative pathway for the transfer of hippocampal representations to neocortical circuits (Aggleton and O'Mara, 2022). Anterior thalamic nuclei might operate partially independently of the canonical LVa pathway but the two output streams have been suggested to converge in some cortical areas, promoting memory

consolidation in these interaction zones (Aggleton and O'Mara, 2022). Hippocampal signals likely reach anterior thalamic nuclei via the dorsal Sub which projects to the anterior thalamus both directly as well as indirectly through mammillary bodies (Fanselow and Dong, 2010). Importantly, our present data open up the possibility that mnemonic activity patterns could also reach the anterior thalamus through LVI neurons, possibly following integration of the hippocampal output signals with inputs from further brain areas.

4.8 Limitations of the study and future directions

While the connectivity patterns revealed by the present study set important constraints on signal flow in the MEC deep layer network, certain limitations have to be considered when interpreting the results from our experiments. Furthermore, our findings raise several important questions that will have to be addressed by future studies.

Possible indirect propagation of hippocampal signals to MEC deep layer neurons

In the present study we focused on direct hippocampal projections to MEC deep layers and did not investigate possible indirect pathways through which hippocampal output signals might propagate to MEC deep layer neurons. Most prominently, both the dorsal and ventral HF send direct projections to the deep layers of LEC (Cenquizca and Swanson, 2007; Naber et al., 2001; van Strien et al., 2009), from where hippocampal output signals could be transmitted to MEC deep layer neurons either indirectly through superficial entorhinal layers (Vandrey et al., 2022) or possibly through direct deep layer projections to MEC LVI (Köhler, 1988).

Connectivity of the lateral entorhinal cortex

Although we did not characterize hippocampal output projections to LEC in the present study, we have analyzed both dorsal and ventral hippocampal projections to LEC LV in Ohara et al., 2023. Our anatomical tracing experiments revealed that hippocampal projections to LEC exhibit a classical parallel topography where dorsal hippocampal projections target the dorsal and ventral hippocampal projections ventral LEC. Furthermore, the innervation of dorsal LEC LVa by dorsal hippocampal projections appears to be robust and both dorsal and ventral hippocampal projections to LEC appear to target both layers Va and Vb with comparable strength (Ohara et al., 2023). This circuit architecture indicates that

dorsal hippocampal output signals propagating to LEC are efficiently conveyed to LEC LVa neurons and can thus reliably reach the neocortex.

Additionally, it has been shown that connectivity from LVb to LVa principal neurons in LEC is considerably stronger than in MEC (Ohara et al., 2021) and that projections from LEC LVa to LVI principal neurons are relatively common (Ben-Simon et al., 2022). Signals processed by individual LEC deep layers thus appear to be at least partially transmitted to other deep layers, indicating that signal processing in the LEC deep layer network differs from the ubiquitous parallel processing seen for MEC deep layers. Currently, the functional relevance of these fundamental differences in connectivity between the LEC and MEC deep layer networks remains unknown. Future studies employing functional circuit mapping will have to determine the exact patterns of connectivity between LEC deep layers, which will form the basis for further investigations into differences in signal processing in the MEC and LEC deep layer networks.

Convergence of dorsal and ventral hippocampal output signals in dorsal MEC LVa

One of the most compelling findings of the present study is the potential convergence of dorsal and ventral hippocampal output signals in dorsal MEC LVa neurons. Based on the fraction of dorsal LVa neurons that received either dorsal or ventral hippocampal input in my recordings, it is highly likely that many LVa neurons integrate dorsal and ventral hippocampal output signals. Nevertheless, in the present study we did not demonstrate this directly. Furthermore, it remains unclear whether cells that receive convergent hippocampal input have distinct projection targets from cells that are only innervated by a single hippocampal pole. Importantly, the functional relevance of this potential convergent pathway will have to be confirmed in vivo using experiments where the ventral hippocampal output pathway is manipulated during a memory task. Our findings predict that increased ventral hippocampal activation during tasks that normally heavily rely on the dorsal HF would result in improved systems consolidation.

Integration of LVI neurons into the MEC circuit

In the present study we focused on the integration of LVI neurons into the MEC deep layer network. In view of the larger MEC circuitry, however, it remains unclear how LVI neurons interact with cells in superficial MEC layers. While the axons of LVI principal cells in our recordings typically travelled towards Sub, in line with hippocampal projection targets (Ben-

Simon et al., 2022), we regularly observed axonal bifurcations where one branch of the axon travelled through LVa into LIII. It is therefore possible that LVI neurons target cells in superficial MEC layers. Conversely, LVI principal neurons might be weakly innervated by LII stellate cells (Sürmeli et al., 2015), raising the possibility that information processed by superficial MEC neurons might reach LVI.

Integration of hippocampal output signals with input from other neuronal populations

In addition to hippocampal output signals, principal neurons in all MEC deep layers receive input from a variety of neuronal populations in different brain areas. LVa neurons were recently shown to receive direct input from the visual cortex (Shao et al., 2024), LVb neurons are innervated by both LII stellate (Sürmeli et al., 2015) and LIII pyramidal neurons (Beed et al., 2020) and LVI neurons receive input from anterior thalamic nuclei and the claustrum (Ben-Simon et al., 2022). Future studies will have to determine how MEC deep layer neurons integrate inputs from these different neuronal populations with hippocampal output signals, which will be essential for understanding information processing in the MEC deep layer network.

CONCLUSION

Recent structural and functional insights have fundamentally changed our understanding of the MEC deep layer network. We now know that MEC deep layers do not simply mediate the transfer of hippocampal representations to neocortical areas but feature a complex functional organization where principal cells in individual layers originate projections to different downstream brain regions. This architecture likely allows hippocampal output signals to conditionally activate distinct neuronal circuits, enabling specific processing based on the current cognitive task or behavioral state of the animal. The routing of hippocampal outputs to these divergent pathways has previously remained obscure due to incomplete knowledge of hippocampal innervation of individual deep layers and crosstalk between layers V and VI. To address these gaps in our understanding, in the present study we systematically characterized the functional organization of the hippocampal output pathway to MEC deep layers and the integration of LVI neurons into the MEC deep layer circuitry.

First, using a combination of anatomical and optogenetic circuit mapping, we found that LVA neurons are strongly targeted by ventral hippocampal outputs along the entire dorsoventral MEC axis. We thus identified a major source of hippocampal output signals to dorsal LVA neurons which, based on previous and our current findings, are weakly innervated by the dorsal HF. Ventral hippocampal signals thus appear to dominate the hippocampal-neocortical dialogue. At the same time, the convergence of dorsal and ventral hippocampal signals in dorsal LVA may represent a conditional gating mechanism by which information from the dorsal HF can reach the neocortex for consolidation. We additionally demonstrated comparatively weaker hippocampal innervation of neurons in LVI, indicating that LVI cells likely integrate hippocampal output signals with input from further neuronal populations.

Second, using paired patch clamp recordings we found minimal interlaminar connectivity between principal cells in LVI and both LV sublayers. These data complement previous results that have demonstrated sparse connectivity between principal cells in sublayers Va and Vb and together suggest that signals within individual deep layer subnetworks are processed largely independently in parallel streams of activity. In summary, the present study identified key principles of connectivity that govern signal flow in the hippocampal-medial entorhinal output pathway and between MEC deep layers. These findings set the groundwork for future functional studies on the segregated deep layer pathways which will be key for understanding information processing in the hippocampal-medial entorhinal system.

ACKNOWLEDGEMENTS

I would like to sincerely thank my supervisors Dr. Alexei Egorov and Prof. Andreas Draguhn for their kind support and assistance throughout my doctoral studies. Their expert knowledge and constructive input were invaluable for the success of this thesis project and allowed me to grow both scientifically and personally.

I would also like to thank our scientific collaborators, Prof. Menno Witter and Dr. Shinya Ohara, who contributed to our fruitful common work with high quality experiments and general scientific expertise. Our collaboration has been a pleasure!

I am additionally deeply grateful to all members of the Draguhn lab for their help and assistance at various stages of this project and for creating a supportive and friendly working atmosphere.

Finally, I would like to thank my family, friends and my loving girlfriend Larissa for your continued support and for giving me the regular opportunity to disengage from scientific work. Without these much needed intermissions I would not have been able to consistently invest most of my time and effort into this project.

Thank you!

REFERENCES

- Aggleton, J.P., and O'Mara, S.M. (2022). The anterior thalamic nuclei: core components of a tripartite episodic memory system. *Nat Rev Neurosci* 23, 505–516. <https://doi.org/10.1038/s41583-022-00591-8>.
- Annese, J., Schenker-Ahmed, N.M., Bartsch, H., Maechler, P., Sheh, C., Thomas, N., Kayano, J., Ghatan, A., Bresler, N., Frosch, M.P., et al. (2014). Postmortem examination of patient H.M.'s brain based on histological sectioning and digital 3D reconstruction. *Nat Commun* 5, 3122. <https://doi.org/10.1038/ncomms4122>.
- Barnes, C.A., McNaughton, B.L., Mizumori, S.J., Leonard, B.W., and Lin, L.H. (1990). Comparison of spatial and temporal characteristics of neuronal activity in sequential stages of hippocampal processing. *Prog Brain Res* 83, 287–300. [https://doi.org/10.1016/s0079-6123\(08\)61257-1](https://doi.org/10.1016/s0079-6123(08)61257-1).
- Barrientos, S.A., and Tiznado, V. (2016). Hippocampal CA1 Subregion as a Context Decoder. *J. Neurosci.* 36, 6602–6604. <https://doi.org/10.1523/JNEUROSCI.1107-16.2016>.
- Beed, P., de Filippo, R., Holman, C., Johenning, F.W., Leibold, C., Caputi, A., Monyer, H., and Schmitz, D. (2020). Layer 3 Pyramidal Cells in the Medial Entorhinal Cortex Orchestrate Up-Down States and Entrain the Deep Layers Differentially. *Cell Rep* 33, 108470. <https://doi.org/10.1016/j.celrep.2020.108470>.
- Benarroch, E.E. (2021). What is the Role of the Claustrum in Cortical Function and Neurologic Disease? *Neurology* 96, 110–113. [10.1212/WNL.00000000000011280](https://doi.org/10.1212/WNL.00000000000011280).
- Ben-Simon, Y., Kaefer, K., Velicky, P., Csicsvari, J., Danzl, J.G., and Jonas, P. (2022). A direct excitatory projection from entorhinal layer 6b neurons to the hippocampus contributes to spatial coding and memory. *Nat Commun* 13, 4826. <https://doi.org/10.1038/s41467-022-32559-8>.
- Benson, D.L., Isackson, P.J., Gall, C.M., and Jones, E.G. (1992). Contrasting patterns in the localization of glutamic acid decarboxylase and Ca²⁺/calmodulin protein kinase gene expression in the rat central nervous system. *Neuroscience* 46, 825–849. [https://doi.org/10.1016/0306-4522\(92\)90188-8](https://doi.org/10.1016/0306-4522(92)90188-8).
- Boccaro, C.N., Kjonigsen, L.J., Hammer, I.M., Bjaalie, J.G., Leergaard, T.B., and Witter, M.P. (2015). A three-plane architectonic atlas of the rat hippocampal region. *Hippocampus* 25, 838–857. <https://doi.org/10.1002/hipo.22407>.
- Buzsáki, G. (2015). Hippocampal sharp wave-ripple: A cognitive biomarker for episodic memory and planning. *Hippocampus* 25, 1073–1188. <https://doi.org/10.1002/hipo.22488>.

Buzsáki, G., and Moser, E.I. (2013). Memory, navigation and theta rhythm in the hippocampal-entorhinal system. *Nat Neurosci* 16, 130–138. 10.1038/nn.3304.

Cajal, S.R. (1911). *Histologie du Système Nerveux de l'Homme et des Vertébrés*. A. Maloine (Paris 1909-1911).

Canto, C.B., and Witter, M.P. (2012). Cellular properties of principal neurons in the rat entorhinal cortex. II. The medial entorhinal cortex. *Hippocampus* 22, 1277–1299. <https://doi.org/10.1002/hipo.20993>.

Cappaert, N.L.M., Van Strien, N.M., and Witter, M.P. (2015). Chapter 20 - Hippocampal Formation. In *The Rat Nervous System (Fourth Edition)*, G. Paxinos, ed. (Academic Press), pp. 511–573. <https://doi.org/10.1016/B978-0-12-374245-2.00020-6>.

Cembrowski, M.S., Wang, L., Lemire, A.L., Copeland, M., DiLisio, S.F., Clements, J., and Spruston, N. (2018). The subiculum is a patchwork of discrete subregions. *Elife* 7, e37701. <https://doi.org/10.7554/eLife.37701>.

Cenquizca, L.A., and Swanson, L.W. (2007). Spatial organization of direct hippocampal field CA1 axonal projections to the rest of the cerebral cortex. *Brain Res Rev* 56, 1–26. <https://doi.org/10.1016/j.brainresrev.2007.05.002>.

Chrobak, J.J., and Buzsáki, G. (1996). High-Frequency Oscillations in the Output Networks of the Hippocampal–Entorhinal Axis of the Freely Behaving Rat. *The Journal of Neuroscience* 16, 3056. <https://doi.org/10.1523/JNEUROSCI.16-09-03056.1996>.

Curtis, C.E., and D'Esposito, M. (2004). The effects of prefrontal lesions on working memory performance and theory. *Cogn Affect Behav Neurosci* 4, 528–539. <https://doi.org/10.3758/cabn.4.4.528>.

Daume, J., Kamiński, J., Schjetnan, A.G.P., Salimpour, Y., Khan, U., Kyzar, M., Reed, C.M., Anderson, W.S., Valiante, T.A., Mamelak, A.N., et al. (2024). Control of working memory by phase-amplitude coupling of human hippocampal neurons. *Nature* 629, 393–401. <https://doi.org/10.1038/s41586-024-07309-z>.

Diamantaki, M., Frey, M., Berens, P., Preston-Ferrer, P., and Burgalossi, A. (2016). Sparse activity of identified dentate granule cells during spatial exploration. *Elife* 5, e20252. <https://doi.org/10.7554/eLife.20252>.

Dickerson, B.C., and Eichenbaum, H. (2010). The episodic memory system: neurocircuitry and disorders. *Neuropsychopharmacology* 35, 86–104. 10.1038/npp.2009.126.

- Diehl, G.W., Hon, O.J., Leutgeb, S., and Leutgeb, J.K. (2017). Grid and Nongrid Cells in Medial Entorhinal Cortex Represent Spatial Location and Environmental Features with Complementary Coding Schemes. *Neuron* 94, 83–92.e6. [10.1016/j.neuron.2017.03.004](https://doi.org/10.1016/j.neuron.2017.03.004).
- Dolorfo, C.L., and Amaral, D.G. (1998). Entorhinal cortex of the rat: topographic organization of the cells of origin of the perforant path projection to the dentate gyrus. *J Comp Neurol* 398, 25–48. [https://doi.org/10.1002/\(SICI\)1096-9861\(19980817\)398:1<25::AID-CNE3>3.0.CO;2-B](https://doi.org/10.1002/(SICI)1096-9861(19980817)398:1<25::AID-CNE3>3.0.CO;2-B)
- Dudek, S.M., Alexander, G.M., and Farris, S. (2016). Rediscovering area CA2: unique properties and functions. *Nature reviews. Neuroscience* 17, 89. [10.1038/nrn.2015.22](https://doi.org/10.1038/nrn.2015.22).
- Ekstrom, A.D., and Hill, P.F. (2023). Spatial navigation and memory: A review of the similarities and differences relevant to brain models and age. *Neuron* 111, 1037–1049. <https://doi.org/10.1016/j.neuron.2023.03.001>.
- Eriksson, J., Vogel, E.K., Lansner, A., Bergström, F., and Nyberg, L. (2015). Neurocognitive Architecture of Working Memory. *Neuron* 88, 33–46. [10.1016/j.neuron.2015.09.020](https://doi.org/10.1016/j.neuron.2015.09.020).
- Fanselow, M.S., and Dong, H.-W. (2010). Are the dorsal and ventral hippocampus functionally distinct structures? *Neuron* 65, 7–19. [10.1016/j.neuron.2009.11.031](https://doi.org/10.1016/j.neuron.2009.11.031).
- Feldmeyer, D. (2023). Structure and function of neocortical layer 6b. *Front Cell Neurosci* 17, 1257803. <https://doi.org/10.3389/fncel.2023.1257803>.
- Foster, N.N., Barry, J., Korobkova, L., Garcia, L., Gao, L., Becerra, M., Sherfat, Y., Peng, B., Li, X., Choi, J.-H., et al. (2021). The mouse cortico–basal ganglia–thalamic network. *Nature* 598, 188–194. <https://doi.org/10.1038/s41586-021-03993-3>.
- Fujimaru, Y., and Kosaka, T. (1996). The distribution of two calcium binding proteins, calbindin D-28K and parvalbumin, in the entorhinal cortex of the adult mouse. *Neurosci Res* 24, 329–343. [https://doi.org/10.1016/0168-0102\(95\)01008-4](https://doi.org/10.1016/0168-0102(95)01008-4).
- Fyhn, M., Molden, S., Witter, M.P., Moser, E.I., and Moser, M.-B. (2004). Spatial representation in the entorhinal cortex. *Science* 305, 1258–1264. [10.1126/science.1099901](https://doi.org/10.1126/science.1099901).
- Gerlei, K., Passlack, J., Hawes, I., Vandrey, B., Stevens, H., Papastathopoulos, I., and Nolan, M.F. (2020). Grid cells are modulated by local head direction. *Nat Commun* 11, 4228. <https://doi.org/10.1038/s41467-020-17500-1>.
- Gerlei, K.Z., Brown, C.M., Sürmeli, G., and Nolan, M.F. (2021). Deep entorhinal cortex: from circuit organization to spatial cognition and memory. *Trends Neurosci* 44, 876–887. <https://doi.org/10.1016/j.tins.2021.08.003>.

Germroth, P., Schwerdtfeger, W.K., and Buhl, E.H. (1989). Morphology of identified entorhinal neurons projecting to the hippocampus. A light microscopical study combining retrograde tracing and intracellular injection. *Neuroscience* 30, 683–691. [https://doi.org/10.1016/0306-4522\(89\)90161-9](https://doi.org/10.1016/0306-4522(89)90161-9).

Gloveli, T., Schmitz, D., Empson, R.M., Dugladze, T., and Heinemann, U. (1997). Morphological and electrophysiological characterization of layer III cells of the medial entorhinal cortex of the rat. *Neuroscience* 77, 629–648. [https://doi.org/10.1016/s0306-4522\(96\)00494-0](https://doi.org/10.1016/s0306-4522(96)00494-0).

GoodSmith, D., Chen, X., Wang, C., Kim, S.H., Song, H., Burgalossi, A., Christian, K.M., and Knierim, J.J. (2017). Spatial Representations of Granule Cells and Mossy Cells of the Dentate Gyrus. *Neuron* 93, 677-690.e5. <https://doi.org/10.1016/j.neuron.2016.12.026>.

Hafting, T., Fyhn, M., Molden, S., Moser, M.-B., and Moser, E.I. (2005). Microstructure of a spatial map in the entorhinal cortex. *Nature* 436, 801–806. [10.1038/nature03721](https://doi.org/10.1038/nature03721).

Hamam, B.N., Amaral, D.G., and Alonso, A.A. (2002). Morphological and electrophysiological characteristics of layer V neurons of the rat lateral entorhinal cortex. *J Comp Neurol* 451, 45–61. <https://doi.org/10.1002/cne.10335>.

Hannula, D.E., and Ranganath, C. (2008). Medial Temporal Lobe Activity Predicts Successful Relational Memory Binding. *J Neurosci* 28, 116–124. <https://doi.org/10.1523/JNEUROSCI.3086-07.2008>.

Hartley, T., Bird, C.M., Chan, D., Cipolotti, L., Husain, M., Vargha-Khadem, F., and Burgess, N. (2007). The hippocampus is required for short-term topographical memory in humans. *Hippocampus* 17, 34–48. <https://doi.org/10.1002/hipo.20240>.

Henke, P.G. (1990). Hippocampal pathway to the amygdala and stress ulcer development. *Brain Res Bull* 25, 691–695. [https://doi.org/10.1016/0361-9230\(90\)90044-z](https://doi.org/10.1016/0361-9230(90)90044-z).

Insausti, R., Muñoz-López, M., Insausti, A.M., and Artacho-Pérula, E. (2017). The Human Periallocortex: Layer Pattern in Presubiculum, Parasubiculum and Entorhinal Cortex. A Review. *Front Neuroanat* 11, 84. <https://doi.org/10.3389/fnana.2017.00084>.

Jay, T.M., and Witter, M.P. (1991). Distribution of hippocampal CA1 and subicular efferents in the prefrontal cortex of the rat studied by means of anterograde transport of Phaseolus vulgaris-leucoagglutinin. *J Comp Neurol* 313, 574–586. [10.1002/cne.903130404](https://doi.org/10.1002/cne.903130404).

Jiang, X., Shen, S., Cadwell, C.R., Berens, P., Sinz, F., Ecker, A.S., Patel, S., and Tolias, A.S. (2015). Principles of connectivity among morphologically defined cell types in adult neocortex. *Science* 350, aac9462. <https://doi.org/10.1126/science.aac9462>.

- Johnston, D., and Amaral, D.G. (2004). Hippocampus. In *The synaptic organization of the brain*, 5th ed (Oxford University Press), pp. 455–498.
<https://doi.org/10.1093/acprof:oso/9780195159561.003.0011>.
- Jonides, J., Lewis, R.L., Nee, D.E., Lustig, C.A., Berman, M.G., and Moore, K.S. (2008). The Mind and Brain of Short-Term Memory. *Annu Rev Psychol* 59, 193–224.
<https://doi.org/10.1146/annurev.psych.59.103006.093615>.
- Josselyn, S.A., and Tonegawa, S. (2020). Memory engrams: Recalling the past and imagining the future. *Science* 367, eaaw4325. <https://doi.org/10.1126/science.aaw4325>.
- Jung, M.W., Wiener, S.I., and McNaughton, B.L. (1994). Comparison of spatial firing characteristics of units in dorsal and ventral hippocampus of the rat. *J Neurosci* 14, 7347–7356. <https://doi.org/10.1523/JNEUROSCI.14-12-07347.1994>.
- Justus, D., Dalügge, D., Bothe, S., Fuhrmann, F., Hannes, C., Kaneko, H., Friedrichs, D., Sosulina, L., Schwarz, I., Elliott, D.A., et al. (2017). Glutamatergic synaptic integration of locomotion speed via septoentorhinal projections. *Nat Neurosci* 20, 16–19. 10.1038/nn.4447.
- Kerr, K.M., Agster, K.L., Furtak, S.C., and Burwell, R.D. (2007). Functional neuroanatomy of the parahippocampal region: the lateral and medial entorhinal areas. *Hippocampus* 17, 697–708. <https://doi.org/10.1002/hipo.20315>.
- Kitamura, T., Ogawa, S.K., Roy, D.S., Okuyama, T., Morrissey, M.D., Smith, L.M., Redondo, R.L., and Tonegawa, S. (2017). Engrams and circuits crucial for systems consolidation of a memory. *Science* 356, 73–78. <https://doi.org/10.1126/science.aam6808>.
- Kitamura, T., Pignatelli, M., Suh, J., Kohara, K., Yoshiki, A., Abe, K., and Tonegawa, S. (2014). Island cells control temporal association memory. *Science* 343, 896–901. <https://doi.org/10.1126/science.1244634>.
- Kjonigsen, L.J., Lillehaug, S., Bjaalie, J.G., Witter, M.P., and Leergaard, T.B. (2015). Waxholm Space atlas of the rat brain hippocampal region: three-dimensional delineations based on magnetic resonance and diffusion tensor imaging. *Neuroimage* 108, 441–449. <https://doi.org/10.1016/j.neuroimage.2014.12.080>.
- Klausberger, T., and Somogyi, P. (2008). Neuronal diversity and temporal dynamics: the unity of hippocampal circuit operations. *Science* 321, 53–57. 10.1126/science.1149381.
- Klink, R., and Alonso, A. (1997). Morphological characteristics of layer II projection neurons in the rat medial entorhinal cortex. *Hippocampus* 7, 571–583. [https://doi.org/10.1002/\(SICI\)1098-1063\(1997\)7:5<571::AID-HIPO12>3.0.CO;2-Y](https://doi.org/10.1002/(SICI)1098-1063(1997)7:5<571::AID-HIPO12>3.0.CO;2-Y).

Kloosterman, F., Van Haeften, T., Witter, M.P., and Lopes Da Silva, F.H. (2003a). Electrophysiological characterization of interlaminar entorhinal connections: an essential link for re-entrance in the hippocampal-entorhinal system. *Eur J Neurosci* 18, 3037–3052. <https://doi.org/10.1111/j.1460-9568.2003.03046.x>.

Kloosterman, F., Witter, M.P., and Van Haeften, T. (2003b). Topographical and laminar organization of subicular projections to the parahippocampal region of the rat. *J Comp Neurol* 455, 156–171. <https://doi.org/10.1002/cne.10472>.

Köhler, C. (1988). Intrinsic connections of the retrohippocampal region in the rat brain: III. The lateral entorhinal area. *J Comp Neurol* 271, 208–228. [10.1002/cne.902710204](https://doi.org/10.1002/cne.902710204).

Lubenov, E.V., and Siapas, A.G. (2009). Hippocampal theta oscillations are travelling waves. *Nature* 459, 534–539. <https://doi.org/10.1038/nature08010>.

Marozzi, E., Jeffery, K.J., 2012. Place, space and memory cells. *Curr Biol* 22, R939-942. <https://doi.org/10.1016/j.cub.2012.10.022>

Maurer, A.P., and Nadel, L. (2021). The Continuity of Context: A Role for the Hippocampus. *Trends Cogn Sci* 25, 187–199. <https://doi.org/10.1016/j.tics.2020.12.007>.

Miettinen, M., Pitkänen, A., and Miettinen, R. (1997). Distribution of calretinin-immunoreactivity in the rat entorhinal cortex: coexistence with GABA. *J Comp Neurol* 378, 363–378. [10.1002/\(sici\)1096-9861\(19970217\)378:3<363::aid-cne5>3.0.co;2-1](https://doi.org/10.1002/(sici)1096-9861(19970217)378:3<363::aid-cne5>3.0.co;2-1)

Mitchell, A.S., Czajkowski, R., Zhang, N., Jeffery, K., and Nelson, A.J.D. (2018). Retrosplenial cortex and its role in spatial cognition. *Brain Neurosci Adv* 2, 2398212818757098. <https://doi.org/10.1177/2398212818757098>.

Moser, E., Moser, M.B., and Andersen, P. (1993). Spatial learning impairment parallels the magnitude of dorsal hippocampal lesions, but is hardly present following ventral lesions. *J Neurosci* 13, 3916–3925. <https://doi.org/10.1523/JNEUROSCI.13-09-03916.1993>.

Moser, M.-B., Rowland, D.C., and Moser, E.I. (2015). Place cells, grid cells, and memory. *Cold Spring Harb Perspect Biol* 7, a021808. <https://doi.org/10.1101/cshperspect.a021808>.

Naber, P.A., Lopes da Silva, F.H., and Witter, M.P. (2001). Reciprocal connections between the entorhinal cortex and hippocampal fields CA1 and the subiculum are in register with the projections from CA1 to the subiculum. *Hippocampus* 11, 99–104. [10.1002/hipo.1028](https://doi.org/10.1002/hipo.1028).

Neher, E., and Sakmann, B. (1976). Single-channel currents recorded from membrane of denervated frog muscle fibres. *Nature* 260, 799–802. <https://doi.org/10.1038/260799a0>.

Nilssen, E.S., Doan, T.P., Nigro, M.J., Ohara, S., and Witter, M.P. (2019). Neurons and networks in the entorhinal cortex: A reappraisal of the lateral and medial entorhinal

subdivisions mediating parallel cortical pathways. *Hippocampus* 29, 1238–1254. <https://doi.org/10.1002/hipo.23145>.

Nuñez, A., and Buño, W. (2021). The Theta Rhythm of the Hippocampus: From Neuronal and Circuit Mechanisms to Behavior. *Front. Cell. Neurosci.* 15. 10.3389/fncel.2021.649262.

Ohara, S., Blankvoort, S., Nair, R.R., Nigro, M.J., Nilssen, E.S., Kentros, C., and Witter, M.P. (2021). Local projections of layer Vb-to-Va are more prominent in lateral than in medial entorhinal cortex. *Elife* 10, e67262. <https://doi.org/10.7554/eLife.67262>.

Ohara, S., Gianatti, M., Itou, K., Berndtsson, C.H., Doan, T.P., Kitanishi, T., Mizuseki, K., Iijima, T., Tsutsui, K.-I., and Witter, M.P. (2019). Entorhinal Layer II Calbindin-Expressing Neurons Originate Widespread Telencephalic and Intrinsic Projections. *Front Syst Neurosci* 13, 54. <https://doi.org/10.3389/fnsys.2019.00054>.

Ohara, S., Onodera, M., Simonsen, Ø.W., Yoshino, R., Hioki, H., Iijima, T., Tsutsui, K.-I., and Witter, M.P. (2018). Intrinsic Projections of Layer Vb Neurons to Layers Va, III, and II in the Lateral and Medial Entorhinal Cortex of the Rat. *Cell Rep* 24, 107–116. <https://doi.org/10.1016/j.celrep.2018.06.014>.

Ohara, S., Rannap, M., Tsutsui, K.-I., Draguhn, A., Egorov, A.V., and Witter, M.P. (2023). Hippocampal-medial entorhinal circuit is differently organized along the dorsoventral axis in rodents. *Cell Reports* 42. <https://doi.org/10.1016/j.celrep.2023.112001>.

O'Keefe, J. (1976). Place units in the hippocampus of the freely moving rat. *Exp Neurol* 51, 78–109. [https://doi.org/10.1016/0014-4886\(76\)90055-8](https://doi.org/10.1016/0014-4886(76)90055-8).

O'Keefe, J., and Dostrovsky, J. (1971). The hippocampus as a spatial map. Preliminary evidence from unit activity in the freely-moving rat. *Brain Res* 34, 171–175. [https://doi.org/10.1016/0006-8993\(71\)90358-1](https://doi.org/10.1016/0006-8993(71)90358-1).

O'Reilly, K.C., Gulden Dahl, A., Ulsaker Kruge, I., and Witter, M.P. (2013). Subicular-parahippocampal projections revisited: development of a complex topography in the rat. *J Comp Neurol* 521, 4284–4299. <https://doi.org/10.1002/cne.23417>.

Papp, E.A., Leergaard, T.B., Calabrese, E., Johnson, G.A., and Bjaalie, J.G. (2014). Waxholm Space atlas of the Sprague Dawley rat brain. *Neuroimage* 97, 374–386. <https://doi.org/10.1016/j.neuroimage.2014.04.001>.

Patel, J., Schomburg, E.W., Berényi, A., Fujisawa, S., and Buzsáki, G. (2013). Local generation and propagation of ripples along the septotemporal axis of the hippocampus. *J Neurosci* 33, 17029–17041. <https://doi.org/10.1523/JNEUROSCI.2036-13.2013>.

Pesold, C., Impagnatiello, F., Pisu, M.G., Uzunov, D.P., Costa, E., Guidotti, A., and Caruncho, H.J. (1998). Reelin is preferentially expressed in neurons synthesizing gamma-aminobutyric acid in cortex and hippocampus of adult rats. *Proc Natl Acad Sci U S A* 95, 3221–3226. <https://doi.org/10.1073/pnas.95.6.3221>.

Ramsden, H.L., Sürmeli, G., McDonagh, S.G., and Nolan, M.F. (2015). Laminar and dorsoventral molecular organization of the medial entorhinal cortex revealed by large-scale anatomical analysis of gene expression. *PLoS Comput Biol* 11, e1004032. <https://doi.org/10.1371/journal.pcbi.1004032>.

Rannap, M., Ohara, S., Winterstein, J., Roth, F.C., Draguhn, A., and Egorov, A.V. (2024). Functional and structural organization of medial entorhinal cortex layer VI. [Manuscript in revision]

Rebola, N., Carta, M., and Mulle, C. (2017). Operation and plasticity of hippocampal CA3 circuits: implications for memory encoding. *Nat Rev Neurosci* 18, 208–220. <https://doi.org/10.1038/nrn.2017.10>.

Roediger, H.L., Zaromb, F.M., and Goode, M.K. (2008). 1.02 - A Typology of Memory Terms. In *Learning and Memory: A Comprehensive Reference*, J. H. Byrne, ed. (Academic Press), pp. 11–24. <https://doi.org/10.1016/B978-012370509-9.00047-4>.

Rolls, E.T. (2013). The mechanisms for pattern completion and pattern separation in the hippocampus. *Front Syst Neurosci* 7, 74. <https://doi.org/10.3389/fnsys.2013.00074>.

Roth, F.C., Beyer, K.M., Both, M., Draguhn, A., and Egorov, A.V. (2016). Downstream effects of hippocampal sharp wave ripple oscillations on medial entorhinal cortex layer V neurons in vitro. *Hippocampus* 26, 1493–1508. <https://doi.org/10.1002/hipo.22623>.

Roy, D.S., Kitamura, T., Okuyama, T., Ogawa, S.K., Sun, C., Obata, Y., Yoshiki, A., and Tonegawa, S. (2017). Distinct Neural Circuits for the Formation and Retrieval of Episodic Memories. *Cell* 170, 1000-1012.e19. <https://doi.org/10.1016/j.cell.2017.07.013>.

Rozov, A., Rannap, M., Lorenz, F., Nasretdinov, A., Draguhn, A., and Egorov, A.V. (2020). Processing of Hippocampal Network Activity in the Receiver Network of the Medial Entorhinal Cortex Layer V. *J. Neurosci.* 40, 8413–8425. [10.1523/JNEUROSCI.0586-20.2020](https://doi.org/10.1523/JNEUROSCI.0586-20.2020).

Saleeba, C., Dempsey, B., Le, S., Goodchild, A., and McMullan, S. (2019). A Student's Guide to Neural Circuit Tracing. *Front Neurosci* 13, 897. [10.3389/fnins.2019.00897](https://doi.org/10.3389/fnins.2019.00897).

Sargolini, F., Fyhn, M., Hafting, T., McNaughton, B.L., Witter, M.P., Moser, M.-B., and Moser, E.I. (2006). Conjunctive representation of position, direction, and velocity in entorhinal cortex. *Science* 312, 758–762. <https://doi.org/10.1126/science.1125572>.

Scoville, W.B., and Milner, B. (1957). Loss of recent memory after bilateral hippocampal lesions. *J Neurol Neurosurg Psychiatry* 20, 11–21. <https://doi.org/10.1136/jnnp.20.1.11>.

Shao, Q., Chen, L., Li, X., Li, M., Cui, H., Li, X., Zhao, X., Shi, Y., Sun, Q., Yan, K., et al. (2024). A non-canonical visual cortical-entorhinal pathway contributes to spatial navigation. *Nat Commun* 15, 4122. <https://doi.org/10.1038/s41467-024-48483-y>.

Shi, Y., Cui, H., Li, X., Chen, L., Zhang, C., Zhao, X., Li, X., Shao, Q., Sun, Q., Yan, K., et al. (2023). Laminar and dorsoventral organization of layer 1 interneuronal microcircuitry in superficial layers of the medial entorhinal cortex. *Cell Rep* 42, 112782. <https://doi.org/10.1016/j.celrep.2023.112782>.

Solstad, T., Boccara, C.N., Kropff, E., Moser, M.-B., and Moser, E.I. (2008). Representation of geometric borders in the entorhinal cortex. *Science* 322, 1865–1868. <https://doi.org/10.1126/science.1166466>.

Squire, L.R., and Zola-Morgan, M. (1991). 3.04 - Declarative Memory System: Amnesia. In *Learning and Memory: A Comprehensive Reference*, J. H. Byrne, ed. (Academic Press), pp. 67–78. <https://doi.org/10.1016/B978-012370509-9.00118-2>.

Steward, O., and Scoville, S.A. (1976). Cells of origin of entorhinal cortical afferents to the hippocampus and fascia dentata of the rat. *J Comp Neurol* 169, 347–370. <https://doi.org/10.1002/cne.901690306>.

Strange, B.A., Witter, M.P., Lein, E.S., and Moser, E.I. (2014). Functional organization of the hippocampal longitudinal axis. *Nat Rev Neurosci* 15, 655–669. [10.1038/nrn3785](https://doi.org/10.1038/nrn3785).

Sürmeli, G., Marcu, D.C., McClure, C., Garden, D.L.F., Pastoll, H., and Nolan, M.F. (2015). Molecularly Defined Circuitry Reveals Input-Output Segregation in Deep Layers of the Medial Entorhinal Cortex. *Neuron* 88, 1040–1053. [10.1016/j.neuron.2015.10.041](https://doi.org/10.1016/j.neuron.2015.10.041).

Swanson, L.W., and Cowan, W.M. (1977). An autoradiographic study of the organization of the efferent connections of the hippocampal formation in the rat. *J Comp Neurol* 172, 49–84. <https://doi.org/10.1002/cne.901720104>.

Tamamaki, N., and Nojyo, Y. (1993). Projection of the entorhinal layer II neurons in the rat as revealed by intracellular pressure-injection of neurobiotin. *Hippocampus* 3, 471–480. <https://doi.org/10.1002/hipo.450030408>.

Tang, Q., Burgalossi, A., Ebbesen, C.L., Ray, S., Naumann, R., Schmidt, H., Spicher, D., and Brecht, M. (2014). Pyramidal and stellate cell specificity of grid and border representations in layer 2 of medial entorhinal cortex. *Neuron* 84, 1191–1197. <https://doi.org/10.1016/j.neuron.2014.11.009>.

- Tang, Q., Ebbesen, C.L., Sanguinetti-Scheck, J.I., Preston-Ferrer, P., Gundlfinger, A., Winterer, J., Beed, P., Ray, S., Naumann, R., Schmitz, D., et al. (2015). Anatomical Organization and Spatiotemporal Firing Patterns of Layer 3 Neurons in the Rat Medial Entorhinal Cortex. *J Neurosci* 35, 12346–12354. [10.1523/JNEUROSCI.0696-15.2015](https://doi.org/10.1523/JNEUROSCI.0696-15.2015).
- Taube, J.S. (2007). The head direction signal: origins and sensory-motor integration. *Annu Rev Neurosci* 30, 181–207. <https://doi.org/10.1146/annurev.neuro.29.051605.112854>.
- Tocker, G., Barak, O., and Derdikman, D. (2015). Grid cells correlation structure suggests organized feedforward projections into superficial layers of the medial entorhinal cortex. *Hippocampus* 25, 1599–1613. <https://doi.org/10.1002/hipo.22481>.
- Treves, A., and Rolls, E.T. (1994). Computational analysis of the role of the hippocampus in memory. *Hippocampus* 4, 374–391. <https://doi.org/10.1002/hipo.450040319>.
- Tsoi, S.Y., Öncül, M., Svahn, E., Robertson, M., Bogdanowicz, Z., McClure, C., and Sürmeli, G. (2022). Telencephalic outputs from the medial entorhinal cortex are copied directly to the hippocampus. *eLife* 11, e73162. <https://doi.org/10.7554/eLife.73162>.
- Tu, B., Gu, Z., Shen, J., Lamb, P.W., and Yakel, J.L. (2009). Characterization of a Nicotine-Sensitive Neuronal Population in Rat Entorhinal Cortex. *J Neurosci* 29, 10436–10448. <https://doi.org/10.1523/JNEUROSCI.2580-09.2009>.
- Tukker, J.J., Beed, P., Brecht, M., Kempter, R., Moser, E.I., and Schmitz, D. (2022). Microcircuits for spatial coding in the medial entorhinal cortex. *Physiol Rev* 102, 653–688. <https://doi.org/10.1152/physrev.00042.2020>.
- van Groen, T. (2001). Entorhinal cortex of the mouse: cytoarchitectonical organization. *Hippocampus* 11, 397–407. <https://doi.org/10.1002/hipo.1054>.
- van Groen, T., Miettinen, P., and Kadish, I. (2003). The entorhinal cortex of the mouse: organization of the projection to the hippocampal formation. *Hippocampus* 13, 133–149. <https://doi.org/10.1002/hipo.10037>.
- van Strien, N.M., Cappaert, N.L.M., and Witter, M.P. (2009). The anatomy of memory: an interactive overview of the parahippocampal-hippocampal network. *Nat Rev Neurosci* 10, 272–282. <https://doi.org/10.1038/nrn2614>.
- Vandrey, B., Armstrong, J., Brown, C.M., Garden, D.L.F., and Nolan, M.F. (2022). Fan cells in lateral entorhinal cortex directly influence medial entorhinal cortex through synaptic connections in layer 1. *Elife* 11, e83008. <https://doi.org/10.7554/eLife.83008>.
- Varga, C., Lee, S.Y., and Soltesz, I. (2010). Target-selective GABAergic control of entorhinal cortex output. *Nature neuroscience* 13, 822. <https://doi.org/10.1038/nn.2570>.

- Winocur, G., Moscovitch, M., and Bontempi, B. (2010). Memory formation and long-term retention in humans and animals: convergence towards a transformation account of hippocampal-neocortical interactions. *Neuropsychologia* 48, 2339–2356. <https://doi.org/10.1016/j.neuropsychologia.2010.04.016>.
- Winterer, J., Maier, N., Wozny, C., Beed, P., Breustedt, J., Evangelista, R., Peng, Y., D'Albis, T., Kempter, R., and Schmitz, D. (2017). Excitatory Microcircuits within Superficial Layers of the Medial Entorhinal Cortex. *Cell Rep* 19, 1110–1116. [10.1016/j.celrep.2017.04.041](https://doi.org/10.1016/j.celrep.2017.04.041).
- Witter, M.P., Doan, T.P., Jacobsen, B., Nilssen, E.S., and Ohara, S. (2017). Architecture of the Entorhinal Cortex A Review of Entorhinal Anatomy in Rodents with Some Comparative Notes. *Front Syst Neurosci* 11, 46. <https://doi.org/10.3389/fnsys.2017.00046>.
- Witter, M.P., Wouterlood, F.G., Naber, P.A., and Van Haeften, T. (2000). Anatomical organization of the parahippocampal-hippocampal network. *Ann N Y Acad Sci* 911, 1–24. <https://doi.org/10.1111/j.1749-6632.2000.tb06716.x>.
- Wouterlood, F.G., and Pothuizen, H. (2000). Sparse colocalization of somatostatin- and GABA-immunoreactivity in the entorhinal cortex of the rat. *Hippocampus* 10, 77–86. [https://doi.org/10.1002/\(SICI\)1098-1063\(2000\)10:1<77::AID-HIPO8>3.0.CO;2-P](https://doi.org/10.1002/(SICI)1098-1063(2000)10:1<77::AID-HIPO8>3.0.CO;2-P).
- Wozny, C., Beed, P., Nitzan, N., Pössnecker, Y., Rost, B.R., and Schmitz, D. (2018). VGLUT2 Functions as a Differential Marker for Hippocampal Output Neurons. *Front Cell Neurosci* 12, 337. <https://doi.org/10.3389/fncel.2018.00337>.
- Yamamoto, N., Yokose, J., Ramesh, K., Kitamura, T., and Ogawa, S.K. (2024). Outer layer of Vb neurons in medial entorhinal cortex project to hippocampal dentate gyrus in mice. *Mol Brain* 17, 5. <https://doi.org/10.1186/s13041-024-01079-5>.
- Yang, S., Yang, S., Moreira, T., Hoffman, G., Carlson, G.C., Bender, K.J., Alger, B.E., and Tang, C.-M. (2014). Interlamellar CA1 network in the hippocampus. *Proc Natl Acad Sci U S A* 111, 12919–12924. <https://doi.org/10.1073/pnas.1405468111>.
- Zhang, S.-J., Ye, J., Miao, C., Tsao, A., Cerniauskas, I., Ledergerber, D., Moser, M.-B., and Moser, E.I. (2013). Optogenetic dissection of entorhinal-hippocampal functional connectivity. *Science* 340, 1232627. <https://doi.org/10.1126/science.1232627>.

APPENDIX A

Supplementary figures

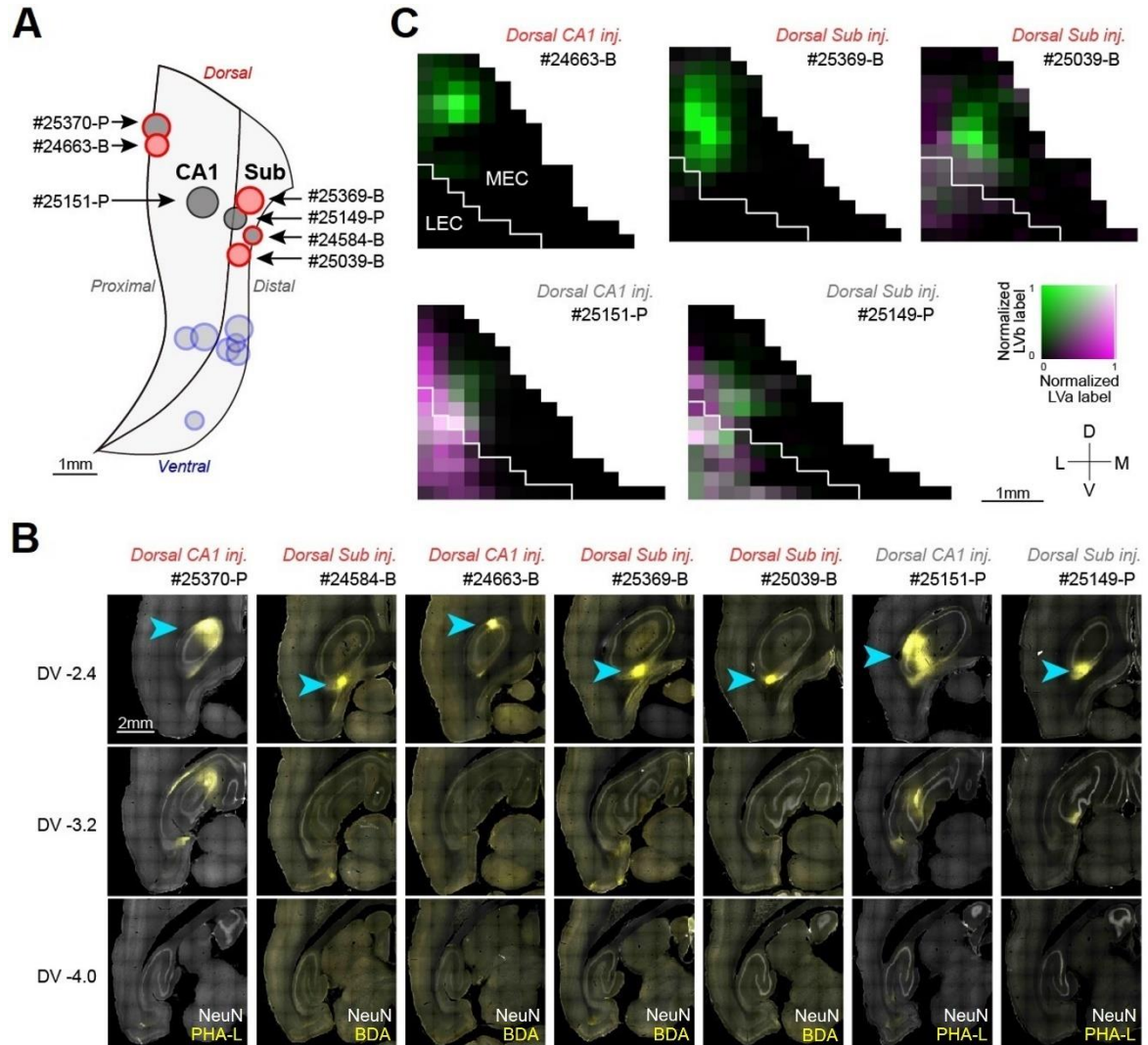


Figure A1. Hippocampal-MEC projections originating from the dorsal HF in the rat horizontal plane. (A) Two-dimensional unfolded map of CA1 and Sub showing the positions of anterograde tracer (PHA-L or BDA) injection sites for rat samples in the horizontal plane. Injection sites in the dorsal HF are shown in red. (B) Low magnification confocal images of injection sites taken at different dorsoventral levels. (C) Representative two-dimensional density maps showing the patterns of anterogradely labeled axons in MEC following anterograde tracer injections into dorsal CA1 or Sub. Two samples, one injected in dorsal distal CA1 (#25151-P) and the other in dorsal proximal subiculum (#25149-P), showed massive labeling of axons in LEC. Due to this labeling pattern, these samples were excluded from the analyses in Figures 8D and 8E which focus on labeling patterns in MEC. Experiments performed by Dr. Shinya Ohara; the figure was modified from Ohara et al., 2023.

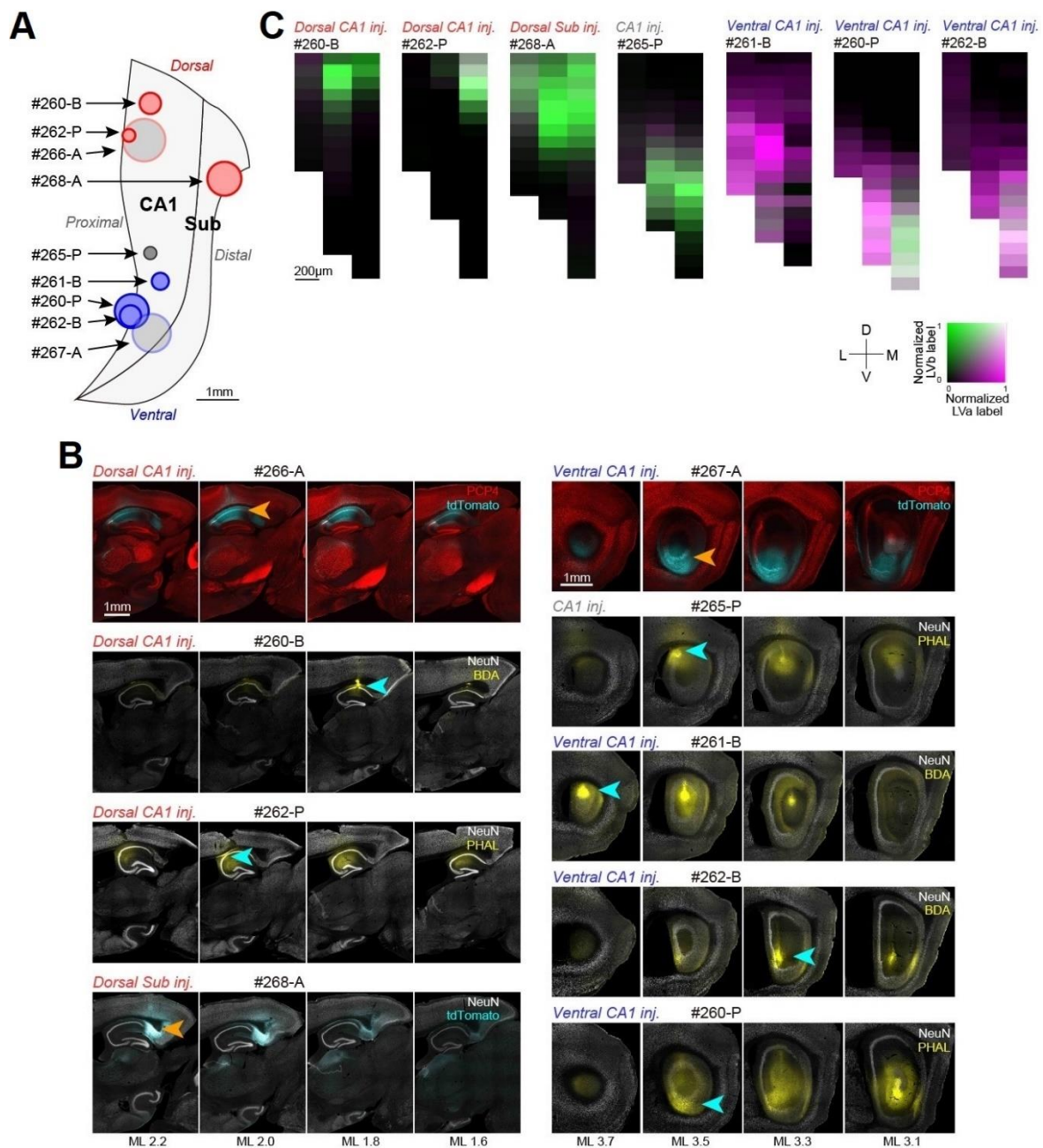


Figure A2. Hippocampal-MEC projections in the mouse sagittal plane. (A) Two-dimensional unfolded map of CA1 and Sub showing the positions of anterograde tracer (PHA-L, BDA or AAV1-Syn1(S)-FLEX-tdTomato-T2A-SypGFP) injection sites for mouse samples in the sagittal plane. (B) Low magnification confocal images of injection sites taken at different mediolateral levels. (C) Two-dimensional density maps showing the patterns of anterogradely labeled axons in MEC following anterograde tracer injections into dorsal or ventral CA1 or Sub. Case #265-P which was located in the intermediate HF was excluded from the analyses in Figures 9D, 9E, 15D and 15E. Experiments performed by Dr. Shinya Ohara; the figure was modified from Ohara et al., 2023.

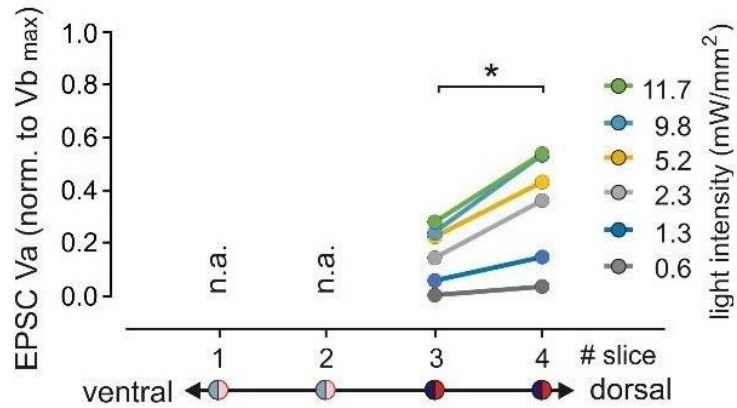


Figure A3. Normalized LVA principal neuron responses measured along the dorsoventral MEC axis for AAV-CaMKIIa-hChR2-EYFP injections into the dorsal HF. Quantification of responses recorded from LVA neurons normalized to the highest LVb EPSC amplitude at maximum light intensity (11.7 mW/mm²) in each slice (level 3: 5 cells from 3 mice; level 4: 7 cells from 5 mice; 11.7 mW/mm², $p = 0.034$, Mann-Whitney U test). Data are analyzed at the two dorsal section levels along the dorsoventral MEC axis for light pulses with increasing intensities; n.a.: not available (none of the neurons in ventral slices responded). The data are presented as median. Mann-Whitney U test for response values at maximum light intensity: * $p < 0.05$. Modified from Ohara et al., 2023.

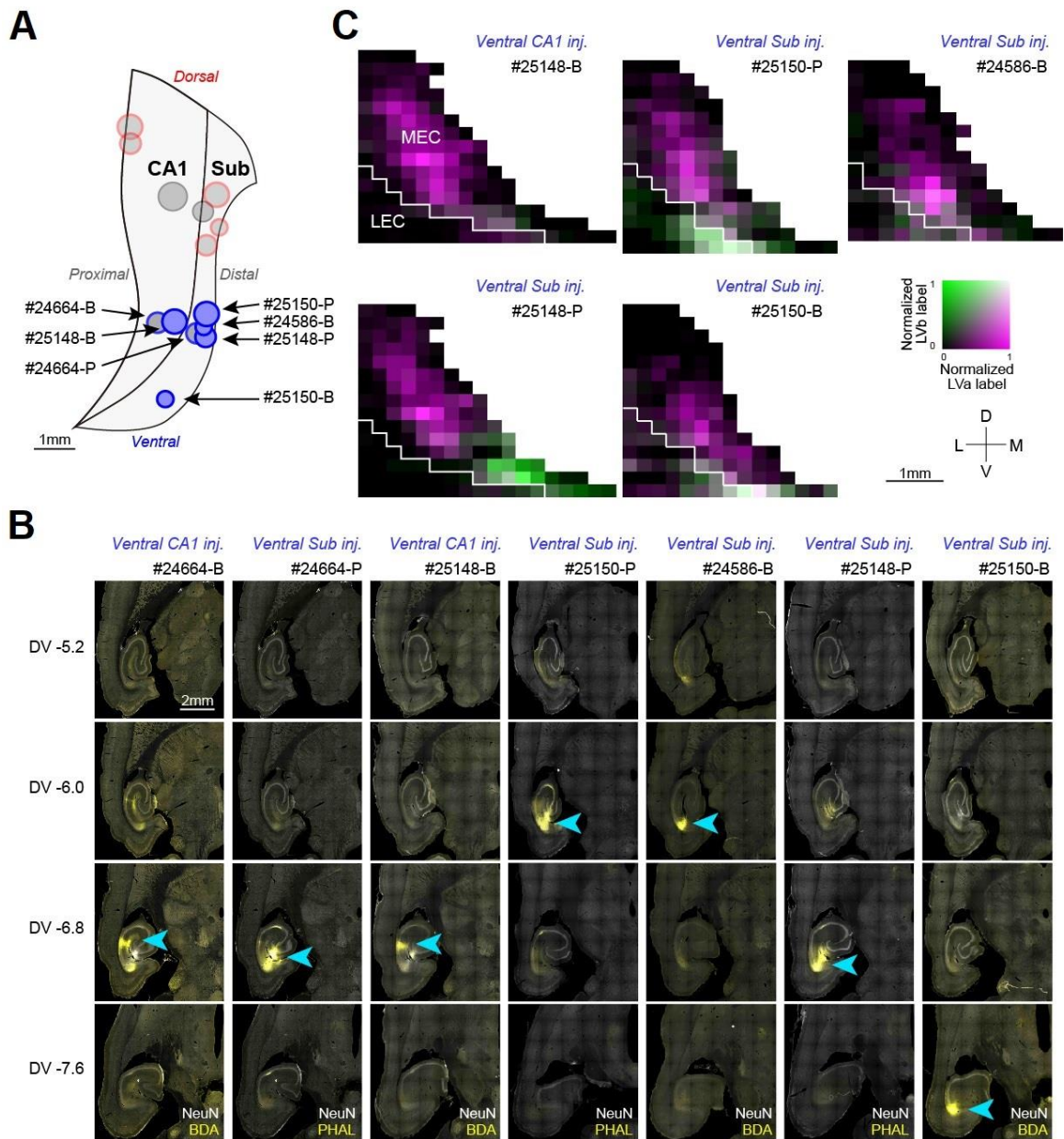


Figure A4. Hippocampal-MEC projections originating from the ventral HF in the rat horizontal plane. (A) Two-dimensional unfolded map of CA1 and Sub showing the positions of anterograde tracer (PHA-L or BDA) injection sites for rat samples in the horizontal plane. Injection sites in the ventral HF are shown in blue. (B) Low magnification confocal images of injection sites taken at different dorsoventral levels. (C) Representative two-dimensional density maps showing the patterns of anterogradely labeled axons in MEC following anterograde tracer injections into ventral CA1 or Sub. Experiments performed by Dr. Shinya Ohara; the figure was modified from Ohara et al., 2023.

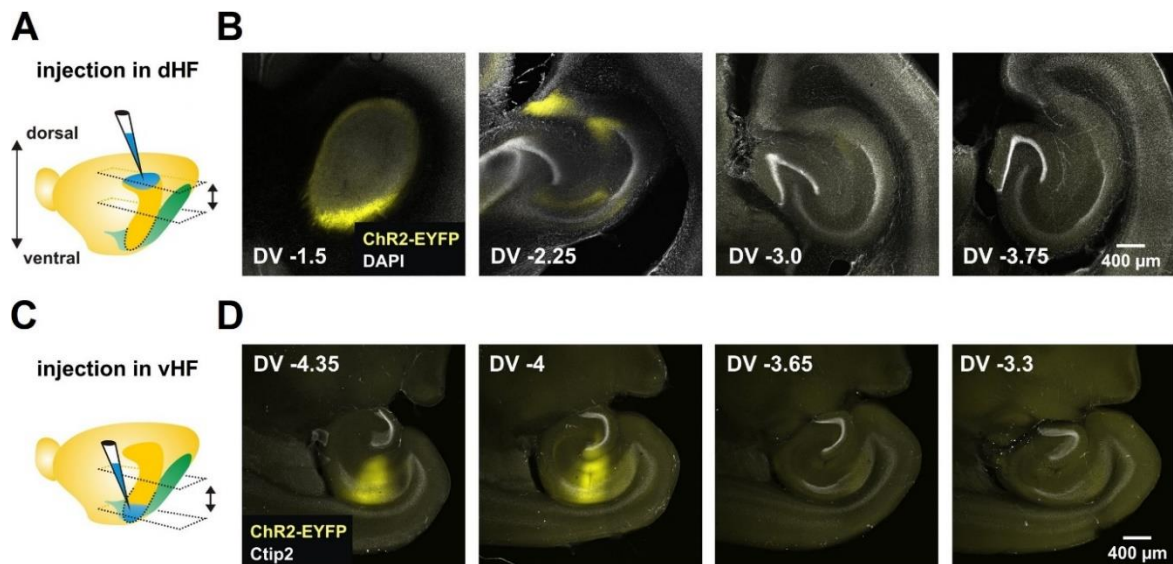


Figure A5. Representative AAV-CaMKIIa-hChR2-EYFP injection sites in the dorsal and ventral HF, related to experiments investigating functional connectivity between the HF and MEC layer VI. (A) Illustration of the injection site (blue) in the dorsal HF (dHF). The approximate range of horizontal sections shown in B are indicated by arrows. (B) Low magnification confocal images of horizontal sections taken at different dorsoventral levels showing the injection site in dorsal CA1. (C) Illustration of the injection site (blue) in the ventral HF (vHF). The approximate range of horizontal sections shown in B are indicated by arrows. (B) Low magnification confocal images of horizontal sections taken at different dorsoventral levels showing the injection site in ventral CA1. Modified from Rannap et al. (in revision).

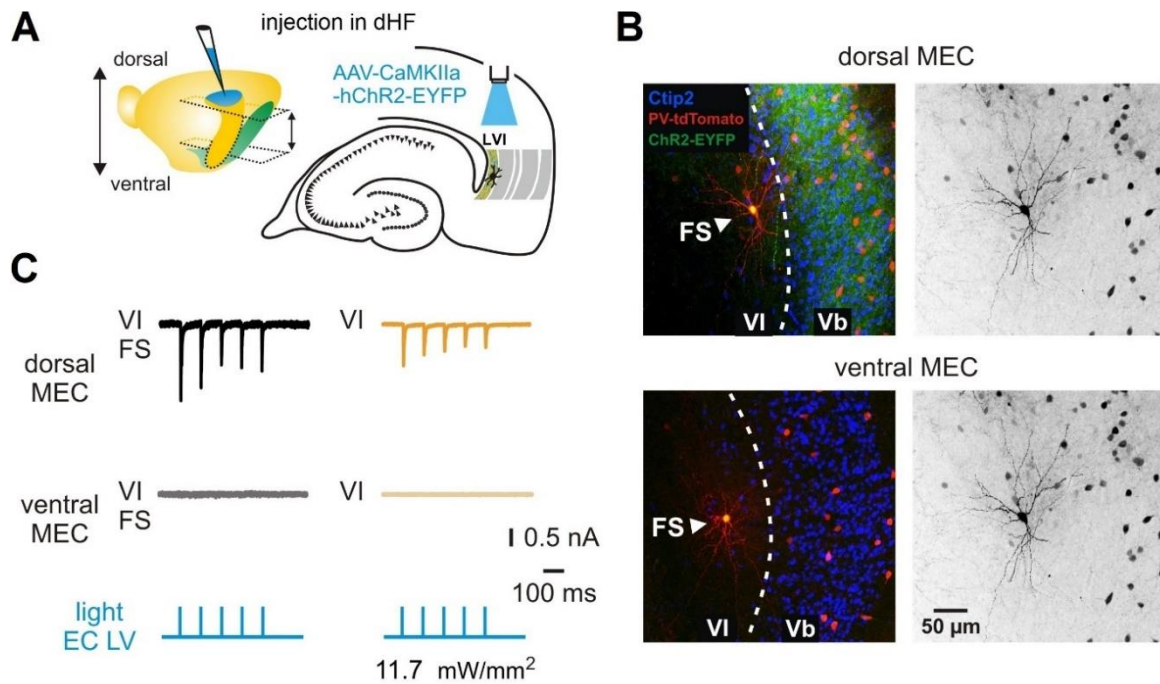


Figure A6. Functional connectivity between the dorsal HF and MEC layer VI FS interneurons. (A) Left: illustration of the injection site (blue) in the dorsal hippocampus of PV-Cre.tdTomato mice with the approximate range of horizontal sections used in experiments indicated by arrows. Right: schematic drawing of a horizontal hippocampal-MEC slice showing the position of light stimulation used to activate the axons of dorsal hippocampal neurons infected with AAV-CaMKIIa-hChR2-EYFP. (B) Maximum intensity projection confocal images of representative horizontal slices from virus-injected PV-Cre.tdTomato mice (PV cells in red). The images show recorded LVI FS interneurons from the dorsal (top) and ventral MEC (bottom) labeled with biocytin (red), overlaid with Ctip2 labeling and fluorescent staining of hippocampal axons expressing hChR2-EYFP. Right images show the same neurons in black and white contrast. (C) Example EPSC traces recorded from LVI FS interneurons in the dorsal (top) and ventral (middle) MEC in response to 1 ms blue light pulses (bottom). Traces from LVI FS cells are compared with respective traces from LVI excitatory neurons from Figure 21C. Modified from Rannap et al. (in revision).

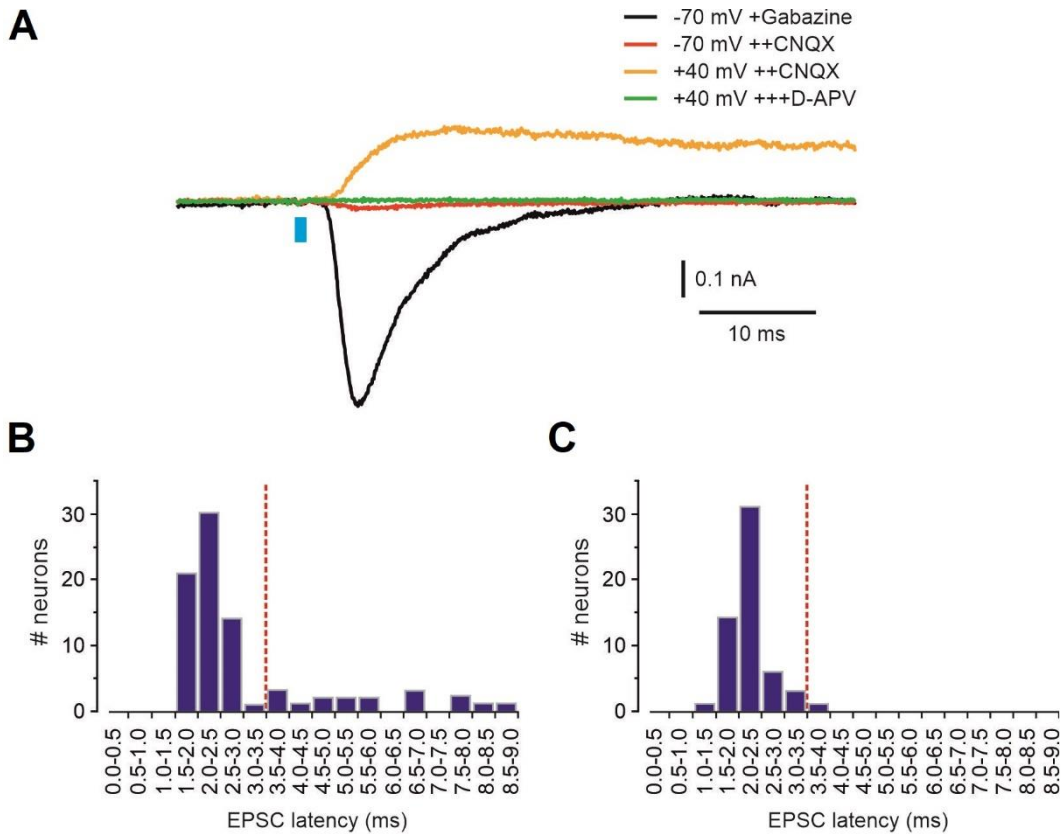


Figure A7. NMDA receptor currents recorded in the presence of CNQX and gabazine and latency distributions for light-evoked EPSCs across different optogenetic experiments. (A) Representative EPSC traces recorded from an excitatory LVI neuron in response to 1 ms light pulses (vertical blue line). Shown is a baseline EPSC recorded at -70 mV in the presence of 100 μ M gabazine (black trace), which was almost entirely blocked by the perfusion of 10 μ M CNQX (red trace). With gabazine and CNQX still in the bath, currents could be reliably recorded at +40 mV (yellow trace), which were subsequently blocked by the perfusion of 30 μ M D-APV (green trace). (B) Histogram showing the combined distribution of light-evoked EPSC latencies for all recorded LVI, LVa and LVb principal neurons from Figures 22 and 25 and LVI FS interneurons from Figures 23 and 26. EPSCs in these experiments were induced by the activation of dorsal or ventral hippocampal axons expressing hChR2-EYFP. The red dashed line indicates the border between putative mono- and polysynaptic responses. (C) Histogram showing the combined distribution of light-evoked EPSC latencies for all recorded LVI and LVb principal neurons from Figure 32. EPSCs in these experiments were induced by the activation of LVa principal cell axons expressing hChR2-EYFP. Modified from Rannap et al. (in revision).

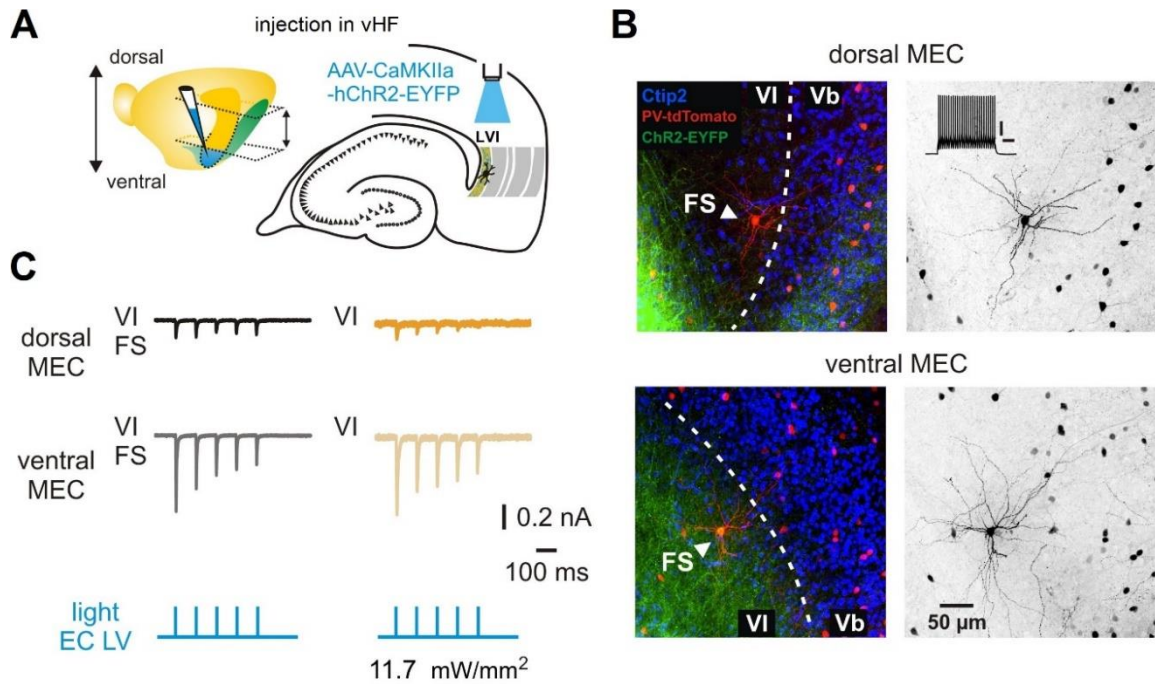


Figure A8. Functional connectivity between the ventral HF and MEC layer VI FS interneurons. (A) Left: illustration of the injection site (blue) in the ventral hippocampus of PV-Cre.tdTomato mice with the approximate range of horizontal sections used in experiments indicated by arrows. Right: schematic drawing of a horizontal hippocampal-MEC slice showing the position of light stimulation used to activate the axons of ventral hippocampal neurons infected with AAV-CaMKIIa-hChR2-EYFP. (B) Maximum intensity projection confocal images of representative horizontal slices from virus-injected PV-Cre.tdTomato mice (PV cells in red). The images show recorded LVI FS interneurons from the dorsal (top) and ventral MEC (bottom) labeled with biocytin (red), overlaid with Ctip2 labeling and fluorescent staining of hippocampal axons expressing hChR2-EYFP. Right images show the same neurons in black and white contrast; inset shows typical FS cell firing behavior in response to a 0.3 nA current injection, scale bars correspond to 20 mV and 100 ms. (C) Example EPSC traces recorded from LVI FS interneurons in the dorsal (top) and ventral (middle) MEC in response to 1 ms blue light pulses (bottom). Traces from LVI FS cells are compared with respective traces from LVI excitatory neurons from Figure 24C. Modified from Rannap et al. (in revision).

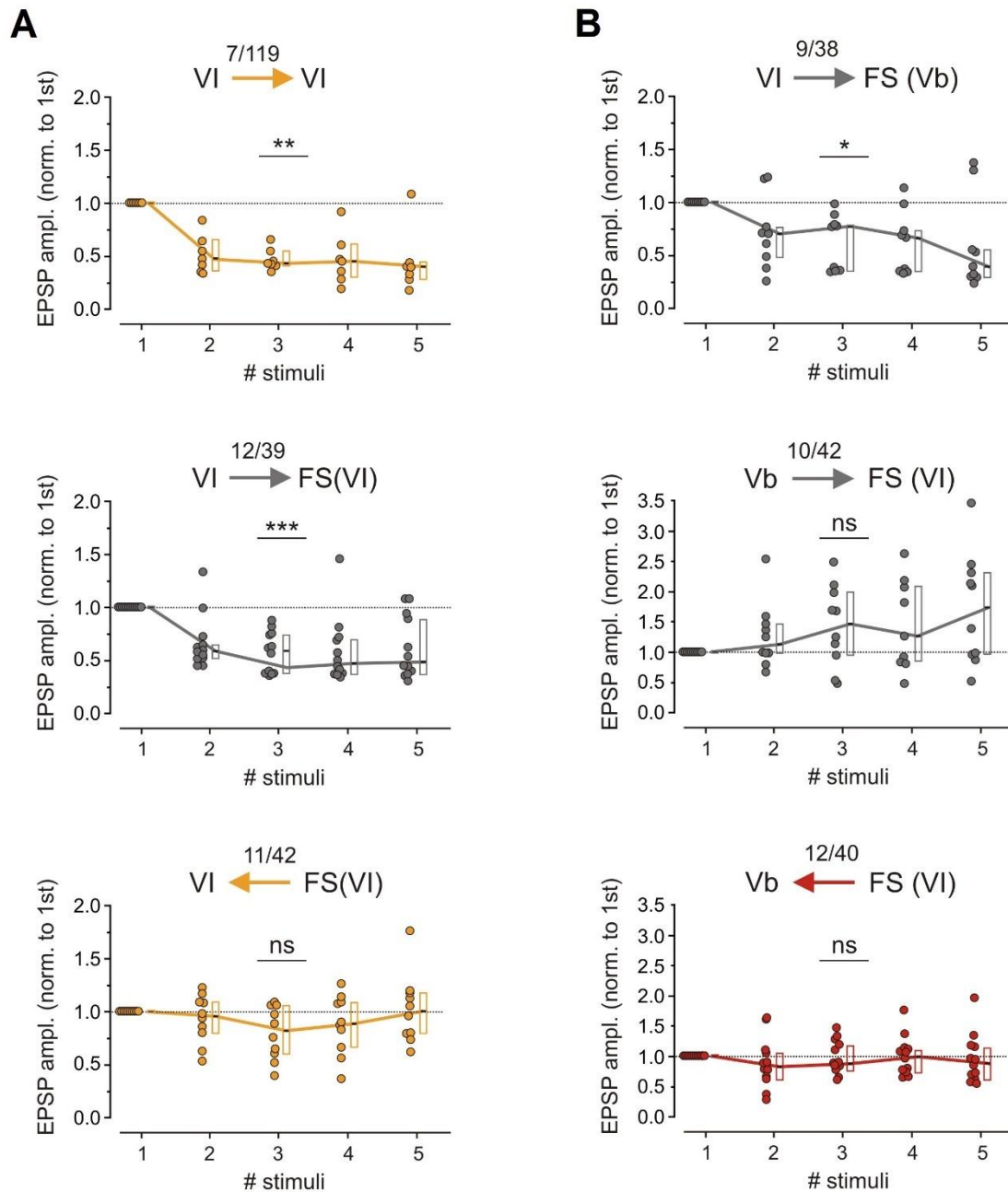


Figure A9. Short-term plasticity of synaptic connections between LVI and LVb excitatory and FS interneurons. (A) Short-term plasticity of synaptic connections between LVI excitatory neurons (top), from LVI excitatory to LVI FS interneurons (middle) and from LVI FS to LVI excitatory cells (bottom). For all connections, PSP amplitudes in response to five consecutive presynaptic action potentials were normalized to the first PSP amplitude. (B) Same analysis as in A for connections from LVI excitatory to LVb FS cells (top), from LVb excitatory to LVI FS cells (middle) and from LVI FS to LVb excitatory cells (bottom). All data are presented as median (black line), 25th and 75th percentiles (box). Circles represent individual values. Friedman repeated measures ANOVA on ranks: *** $p < 0.001$; ** $p < 0.01$; * $p < 0.05$; ns, not significant. Modified from Rannap et al. (in revision).

APPENDIX B

Supplementary tables

Table B1. Intrinsic electrophysiological properties of MEC LVI principal neurons

	Mean \pm SEM (n = 34)
Resting membrane potential (mV)	-72.19 \pm 0.84
Input resistance (M Ω) ¹	179.73 \pm 11.02
Sag ratio ²	1.01 \pm 0.001
AP threshold (mV) ³	-38.00 \pm 0.75
AP peak (mV) ⁴	71.73 \pm 0.97
AP half-width (ms) ⁵	1.53 \pm 0.03
AP 20%-80% rise time (ms)	0.26 \pm 0.01
Max rise slope (mV/ms) ⁶	175.81 \pm 5.44
Max decay slope (mV/ms) ⁷	-40.64 \pm 1.18
AHP amplitude (mV) ⁸	-11.55 \pm 0.37
Rheobase current (pA)	116.91 \pm 6.31
Latency to 1st AP (ms) ⁹	320.34 \pm 13.13
Adaptation ¹⁰	0.77 \pm 0.03

All AP properties were measured from the first AP at rheobase current. AP, action potential; AHP, afterhyperpolarization.

1. Measured from peak voltage deflection in response to a -25 pA current injection according to Ohm's law
2. Ratio between peak voltage deflection and steady-state voltage following a -200 pA current injection
3. Membrane potential at the point where AP rate of rise reached 20 mV/ms
4. Voltage difference between AP threshold and peak
5. Full width at half maximum
6. Maximum rate of rise during the AP rising phase
7. Maximum rate of decay during the AP decaying phase
8. Peak negative voltage deflection after the AP relative to the threshold
9. Measured from the onset of the current injection to the threshold
10. Time interval between the first two APs divided by the interval between the last two APs measured from traces with 8 ± 1 total APs

Adapted from Rannap et al. (in revision).

Table B2. Differences in local LVI connectivity between the dorsal and ventral MEC

		Connectivity	Amplitude (nA)	Latency (ms)	STP (5th/1st)
VI ↔ VI	dMEC	3 of 55 (5.5%)	0.32 [0.16; 1.13]	2.30 [0.59; 4.46]	0.34 [0.19; 0.44]
		p > 0.999	p = 0.114	p = 0.629	p = 0.629
	vMEC	4 of 64 (6.3%)	0.10 [0.08; 0.17]	1.74 [1.50; 1.85]	0.41 [0.31; 0.91]
VI → FS (VI)	dMEC	7 of 21 (33.3%)	0.18 [0.10; 4.18]	0.55 [0.42; 1.13]	0.89 [0.45; 1.08]
		p = 0.742	p = 0.530	p = 0.530	p = 0.020*
	vMEC	5 of 18 (27.8%)	0.95 [0.25; 2.44]	0.81 [0.59; 1.43]	0.37 [0.33; 0.50]
FS (VI) → VI	dMEC	7 of 24 (29.2%)	0.34 [0.15; 0.48]	0.56 [0.26; 0.64]	1.06 [0.80; 1.18]
		p = 0.731	p = 0.833	p = 0.050	p = 0.667
	vMEC	4 of 18 (22.2%)	0.21 [0.13; 1.04]	0.78 [0.66; 2.43]	0.80 [0.62; 1.76]

Values are presented as median, 25th and 75th percentile [P25; P75]. Amplitude and latency values correspond to the first PSP induced by the presynaptic train of five action potentials. Short-term plasticity values represent the amplitude of the last PSP normalized to the first. dMEC, dorsal MEC; vMEC, ventral MEC; STP, short-term plasticity. Mann-Whitney U or Fisher's exact test: *p < 0.05. Adapted from Rannap et al. (in revision).

Table B3. Differences in LVI-LVb connectivity between the dorsal and ventral MEC

		Connectivity	Amplitude (nA)	Latency (ms)	STP (5th/1st)
VI → Vb	dMEC	1 of 59 (1.7%)	0.04	1.66	0.60
	vMEC	0 of 61			
Vb → VI	dMEC	0 of 58			
	vMEC	0 of 64			
VI → FS (Vb)	dMEC	5 of 19 (26.3%) p > 0.999	0.33 [0.10; 0.36] p = 0.905	0.66 [0.56; 0.94] p = 0.064	0.39 [0.28; 0.93] p > 0.999
	vMEC	4 of 19 (21.1%)	0.19 [0.16; 0.45]	1.04 [0.75; 2.23]	0.41 [0.29; 1.16]
FS (Vb) → VI	dMEC	0 of 21			
	vMEC	1 of 20 (5.0%)	0.13	1.61	0.74
Vb → FS (VI)	dMEC	5 of 22 (22.7%) p > 0.999	0.22 [0.12; 0.48] p = 0.691	0.46 [0.42; 0.67] p = 0.548	1.39 [0.92; 2.84] p = 0.841
	vMEC	5 of 20 (25.0%)	0.35 [0.12; 0.61]	0.43 [0.18; 1.59]	2.09 [0.76; 2.23]
FS (VI) → Vb	dMEC	5 of 20 (25.0%) p = 0.731	0.22 [0.05; 0.48] p = 0.639	0.54 [0.48; 0.94] p = 0.048*	1.17 [0.93; 1.65] p = 0.018*
	vMEC	7 of 20 (35.0%)	0.23 [0.11; 0.40]	1.02 [0.77; 1.47]	0.70 [0.56; 0.94]

Values are presented as median, 25th and 75th percentile [P25; P75]. Amplitude and latency values correspond to the first PSP induced by the presynaptic train of five action potentials. Short-term plasticity values represent the amplitude of the last PSP normalized to the first. dMEC, dorsal MEC; vMEC, ventral MEC; STP, short-term plasticity. Mann-Whitney U or Fisher's exact test: *p < 0.05. Adapted from Rannap et al. (in revision).